CHARACTERIZATION AND COOLING CAPACITY ENHANCEMENT OF A POROUS CERAMIC WICK BASED COLDPLATE

by

MAURICIO ADRIÁN SALINAS

Presented to the Faculty of the Graduate School of

The University of Texas at Arlington in Partial Fulfillment

of the Requirements

for the Degree of

DOCTOR OF PHILOSOPHY

THE UNIVERSITY OF TEXAS AT ARLINGTON

December 2008

ACKNOWLEDGEMENTS

First, I dedicate this document to my late mother M. Imelda Guerra de Salinas. She inculcated in me the virtue of education and always believed in me, even when I doubted myself. Next, I would like to express my appreciation and gratitude to my father, Antonio Salinas Tejada, for showing me, by example, the merits of honesty and hard work. He toiled day in and day out for the sole purpose of giving his children a better life. I'd also like to thank my siblings: Marco Antonio, Mario Alberto, Emilia, and Manuel Alfonso, for shaping me into the person I am today.

There were several educators who had a lasting impact in my life. First, was my high school chemistry teacher, Mr. Fernandez, who's enthusiastic teaching style initiated my interest in science. Next, were two undergraduate professors Dr. Hashim S. Mahdi and Dr. Edwin W. LeMaster. Dr. Mahdi taught most of the thermal science courses and was the first to peak my interest in heat transfer. Dr. LeMaster was an unofficial mentor and his words gave me the confidence to go to graduate school.

Next, I would like to thank my employer, Raytheon Company, for financially supporting my doctoral studies. Moreover, my Raytheon advisor, Dr. Donald C. Price, was instrumental in getting this sustenance and he was always available for advice and support. Furthermore, I'd like to thank my current Raytheon advisor, Dr. B. Elliott Short Jr., for stepping in once Dr. Price retired. Finally, I'd like to thank my dissertation advisor, Dr. Seung Mun You, for his guidance and support.

Last but certainly not least, I'd like to thank my wife, Marisa B. Salinas for her unwavering support, always reviewing my work, and giving me a handsome son, Manolo Andrés.

November 14, 2008

ABSTRACT

CHARACTERIZATION AND COOLING CAPACITY
ENHANCEMENT OF A POROUS CERAMIC
WICK BASED COLDPLATE

Mauricio Adrián Salinas, PhD.

The University of Texas at Arlington, 2008

Supervising Professor: Seung Mun You

Current passive cooling methods of aerospace and military, high heat-flux electronics include the use of thermal planes made of exotic metal alloys, which have been designed, at a great expense, to have high thermal conductivity and low density (i.e. light weight). Also, phase change modules composed of a metal matrix saturated with a solid phase change material are being employed for systems requiring a transient cooling scheme such as expendable weapons. This method requires the heat to be transferred from the source location, through the metal matrix (typically a porous aluminum foam), to the available phase change material. Preliminary empirical evaluations performed at Raytheon's Space and Airborne Systems indicate that wick-based coldplates including a non-metallic porous medium, saturated with fluid may be much more effective. This wick-based method allows the capillary action of the wick to passively transport liquid from liquid-rich areas to the point of need, a much more efficient process.

The objective of this research was to characterize the mass and heat transport of this proposed non-metallic, wick-based coldplate. Mass transport was characterized by measuring the wickability (liquid penetration into porous media) between the proposed working fluids and porous medium. This was accomplished by employing the two most common techniques, the height and weight approaches. The height approach requires the measurement of distance penetrated by the liquid into the porous medium, while the weight approach tracks the mass gained by the pores due to imbibition. Experimental data was analyzed through Washburn's Theory. Heat transport was characterized by measuring the transient cooling capacity and the steady state thermal resistance of the proposed wick-based coldplate. For these evaluations, an aluminum oxide based ceramic served as the porous medium with the following working fluids: water, methanol, ethanol, methanol-water mixtures, ethanol-water mixtures, and a fluorinert liquid FC-72.

TABLE OF CONTENTS

ACKNOWLEDGEMENTS…… iii

ABSTRACT…… iv

LIST OF ILLUSTRATIONS…….. ix

LIST OF TABLES…….. xiv

NOMENCLATURE…… xv

Chapter Page

1. INTRODUCTION…… 1

2. MASS TRANSPORT WITHIN PORUS MEDIUM …… 4

2.1 Height Approach…….. 4

2.1.1 Uncertainty Analysis of Height Approach.....…… 5

2.1.2 Effect of Ceramic Wick Thickness on Wickability …… 7

2.1.3 Effect of Fluid on Wickability……..…… 8

2.2 Weight Approach…….. 11

2.2.1 Surface Tension Measurements…….....…… 12

2.2.2 Density Measurements…….....…… 15

2.2.3 Viscosity Measurements…….....…… 17

2.2.4 Contact Angle Measurement Using the Washburn Method ……..…… 21

2.3 Mass Transport Summary…….. 29

3. SURFACE ENERGY ANALYSIS…….. 30

3.1 Zisman Theory……..…….. 30

3.2 Owens-Wendt Theory.....…... 32

3.2.1 Uncertainty Analysis of Goniometer…….. 33
3.2.2 Optically Measured Contact Angle Results……. 36
3.2.3 Owens-Wendt Plot and Results…… 39
3.3 Surface Energy Summary…… 42
4. TRANSIENT COOLING CAPACITY…… 43
4.1 Transient Test Setup…… 46
4.1.1 Transient Test Procedure…….…….. 48
4.2 Transient Test Results for Cotton Wick……..…… 49
4.3 Transient Test Results for Ceramic Wick……..…… 52
4.4 Transient Cooling Capacity Summary..... 56
5. STEADY STATE TEST SETUP……..…… 57
5.1 Coldplate Sealing……..…… 59
5.1.1 O-ring Seal.....…….. 59
5.1.2 Fitting Seal.....…….. 63
5.1.2.1 Sealant Compatibility Test……. 64
5.1.2.2 Thermocouple Seal…….. 68
5.2 Degassing System……..…… 68
5.2.1 Single Fluid Degassing System.....…….. 68
5.2.2 Binary Mixture Degassing System.....…….. 71
5.3 Test Setup and Procedure……..… 73
5.3.1 Uncertainty Analysis of Steady State Test…… 75
5.3.2 Seal Verification.....……..... 76
5.3.3 External Thermocouple Placement…… 79
5.3.4 Steady State Test Procedure…..... 83
6. STEADY STATE THERMAL RESISTANCE…….. 87
6.1 Baseline Thermal Resistances……..…… 87

6.2 Horizontal Test Results…… 88

6.2.1 Thermal Performance with No Wick…….. 88

6.2.2 Thermal Performance of Various Wick Configurations…….. 92

6.2.3 Thermal Performance of Binary Mixtures…… 98

6.3 Vertical Test Results…… 101

6.4 Phase Change Mechanism…… 103

6.5 Steady State Summary…… 105

7. CONCLUSION..... 107

7.1 Summary of Accomplishments and Results…….. 107

7.2 Future Research…… 108

APPENDIX

A. STUDENT-T DISTRIBUTION TABLE..…….. 109

B. TRANSIENT TEMPERATURE PROFILES …… 111

REFERENCES…… 113

BIOGRAPHICAL INFORMATION…… 116

LIST OF ILLUSTRATIONS

Figure		Page
1.1	Surface Tension of Ethanol-Water Mixtures [3]…….....	3
2.1	Longitudinal Wicking “Strip” Test (Height Approach)……..……..	5
2.2	Methanol Height of Rise in Ceramic Wick……..	7
2.3	Rise in Height as a Function of Wick Thickness ……..……..……	8
2.4	Rise in Height for Various Fluids……...	9
2.5	Wickability of Ethanol-Water Mixtures (Height Approach)…….	10
2.6	Wickability of Alcohol-Water Mixtures (Height Approach)…….	11
2.7	Illustration of the Wilhelmy Plate Method…….	12
2.8	Kruss K100 Tensiometer……...	13
2.9	Measured Surface Tensions of Alcohol-Water Mixtures……..	15
2.10	Anton Paar DMA 38 Density Meter……..	16
2.11	Measured Densities of Alcohol-Water Mixtures…….	17
2.12	Gilmont 100 Falling Fall Viscometer…….	18
2.13	Measured Viscosities of Alcohol-Water Mixtures……	20
2.14	Figure 2.14 Property Comparison of Alcohol-Water Mixtures……..	21
2.15	Optical Contact Angle Measurement Technique……	22
2.16	Washburn Method for Calculating Contact Angle……..	23
2.17	Typical Mass Absorbed vs. Time Plot (Hexane)..……..	23
2.18	Contact Angles of Alcohol-Water Mixtures and FC-72 on Ceramic Wick……..	26
2.19	Predicted Volume Absorbed (Weight Approach)…….	27
2.20	Wickability Approach Comparison (Ethanol)……	28

2.21 Wickability Approach Comparison (Methanol)…… 29

3.1 Zisman Plot of Ceramic Wick…….. 31

3.2 FTA 1000 Goniometer…….. 34

3.3 Mathematical Representation of Droplet…….. 34

3.4 Droplet Images of Water on PTFE…… 35

3.5 Measured Contact Angles between Liquids and PTFE……. 36

3.6 Measured Contact Angles between Ethanol-Water Mixtures and PTFE…….. 37

3.7 Measured Contact Angles between Methanol-Water Mixtures and PTFE…….. 38

3.8 Owens-Wendt Plot of Ceramic Wick……. 39

3.9 Fluid Height of Rise in Ceramic Wick…… 41

4.1 Example of an Expendable Weapon System…….. 43

4.2 Example of CCA Cooled by a PCM Coldplate……. 44

4.3 (a) PCM Coldplate (b) Wick-based Coldplate…….. 44

4.4 Baseplate Temperature Profile of (a) PCM Coldplate and (b) Wick-based Coldplate……. 45

4.5 Side View of Transient Cooling Capacity Test (Open System)…….. 47

4.6 Isometric View of Transient Cooling Capacity Test (Open System)…….. 47

4.7 Back View of Transient Cooling Capacity Test (Open System)…….. 48

4.8 Transient Temperature Profile of Cotton Wick with Methanol (Horizontal Position)…… 49

4.9 Transient Temperature Profile – Methanol vs. Ethanol…….. 50

4.10 Transient Temperature Profile – Cotton, Methanol, Vertical……. 51

4.11 Transient Temperature Profile – Cotton, Methanol-Water (40-60), Vertical……. 52

4.12 Transient Temperature Profile – Ceramic, Methanol vs. Ethanol, Vertical..... 53

4.13 Cooling Capacity Comparison between Cotton and Ceramic Wicks..... 54

4.14 Transient Temperature Profile – Ceramic, Methanol-Water Mixtures..... 55

4.15 Transient Cooling Capacity Comparisons for Alcohol-Water Mixtures..... 56

5.1 Typical Military Electronics Box..... 58

5.2 Exploded View of Military Electronics Box..... 58

5.3 Side View of Sealed Wick-based Coldplate Design..... 60

5.4 Isometric View of Top Cover..... 60

5.5 Isometric View of Baseplate..... 61

5.6 Flat Undercut Screw..... 61

5.7 Groove Radii (a) Inconsistent and (b) Consistent Width..... 62

5.8 Access Holes on Top Cover..... 63

5.9 Valve and Pressure Transducer Fittings..... 64

5.10 Compatibility Test Setup..... 65

5.11 (a) Before and (b) After Images of Seal-All (Not to Scale)..... 67

5.12 (a) Before and (b) After Images of 3M Epoxy (Not to Scale)..... 67

5.13 (a) Before and (b) After Images of RTV Silicon (Not to Scale)..... 67

5.14 Single Fluid Degassing System..... 69

5.15 Saturation Curves for Water and Methanol..... 70

5.16 Binary Mixture Degassing System..... 72

5.17 Vapor Pressures of Water-Methanol Mixtures at 50°C..... 73

5.18 Top View of Steady State Test Setup..... 74

5.19 Side View of Steady State Test Setup..... 75

5.20 Example of a Poorly Sealed Coldplate (Water)..... 77

5.21 Example of a Well Sealed Coldplate (Water)…….. 78

5.22 Example of a Well Sealed Coldplate (Methanol)……..…….. 79

5.23 Top View of Numerical Model…… 80

5.24 Isometric View of Inner Side of Coldplate Cover…… 80

5.25 Finite Element Grid of Heater Area (a) Temperature Profile of Cover with Empty Cavity (b)…….. 81

5.26 Modified Numerical Model…….. 82

5.27 Cover Temperature Profiles for Cavity Heat Transfer Coefficients of (a) 100 (b) 1,000 and (c) 10,000 W/m^2K…… 83

5.28 Wick-based Coldplate in Vertical Position…… 85

5.29 Wick-based Coldplate Covered with Insulation…… 85

5.30 Typical Temperature Profile of Steady State Test…….. 86

6.1 Baseline Thermal Resistances…….. 88

6.2 Thermal Performance of a Sealed vs. Leaky Coldplate……. 89

6.3 Thermal Performance as a Function of Fill Ratio (Methanol)…… 90

6.4 Thermal Performance as a Function of Fill Ratio (Water)…… 91

6.5 Thermal Performance Water vs. Methanol vs. 50/50 Mixture…….. 92

6.6 Full Wick Configuration…… 93

6.7 Wick Configuration having Two Gaps…… 93

6.8 Wick Configuration having 1/2 Inch Strips (5 each)……... 94

6.9 Wick Configuration having 1/2 Inch Strips (8 each)…… 94

6.10 Thermal Performance of Various Wick Configurations…… 95

6.11 Wick Configuration having 1/4 Inch Strips (15 each)…….. 96

6.12 Strip Position Shift due to Vacuum Process……. 96

6.13 Thermal Performance of Best Wick Configuration as a Function of Fill Ratio…… 97

6.14 Thermal Performance with Mixture of 30% Methanol and 70% Water…….. 98

6.15 Thermal Performance of Methanol-Water Mixtures (Horizontal)…….…… 99

6.16 Thermal Performance of Wick vs. No Wick (Horizontal)..…… 100

6.17 Thermal Performance of Vertical vs. Horizontal (No Wick)……. 101

6.18 Thermal Performance of Vertical vs. Horizontal (Wick)…….. 102

6.19 Thermal Performance of Methanol-Water Mixtures (Vertical)…….. 103

6.20 Coldplate with Transparent Baseplate……. 104

6.21 Observed Boiling Regions (No Wick)……..……. 104

6.22 Observed Boiling Regions (Wick)…….. 105

LIST OF TABLES

Table		Page
1.1	Thermophysical Properties of Working Fluids ……..…	2
2.1	Surface Tension Measurements of Methanol and Ethanol ……	14
2.2	Density Measurements of Methanol and Ethanol…….	16
2.3	Viscosity Range for Various Ball Materials……	18
2.4	Viscosity Measurements of Methanol and Ethanol……..	19
2.5	Material Constant for Ceramic Wick……	25
3.1	Surface Energy Values for Ceramic Solid and Liquids……	40
3.2	Properties of Working Fluids……	41
5.1	Before and After Weights of Thread Sealants……..	66
5.2	Predicted Temperatures for Modified Numerical Model……..	83

NOMENCLATURE

Abbreviations

CCA	Circuit Card Assembly
CST	Critical Surface Tension (Surface Energy of a Solid)
EPDM	Ethylene Propylene Diene Rubber
FC-72	3M Flourinert Electronic Liquid
FEA	Finite Element Analysis
FSO	Full-Scale Output
FTA	First Ten Angstroms
PCM	Phase Change Material
PT	Pressure Transducer
PTFE	Polytetrafluoroethylene
RSS	Root Sum Square
RTV	Room Temperature Vulcanizer
TC	Thermocouple
TIG	Tungsten Inert Gas

Variables

C	material constant characteristic of porous solid [cm^5]
F	force [mN]
h	rise in fluid height [cm]

$\bar{h}$	average rise in fluid height [cm]
h'	estimated true rise in fluid height [cm]
L	wetted length [m]
m	mass of fluid absorbed by porous solid [g]
N	sample size
S_x	standard deviation
$S_{\bar{x}}$	standard deviation of the means
t	time [sec]
$t_{v,P}$	t estimator (weighting function for finite data sets)
u_c	instrument uncertainty
u_d	design stage uncertainty
u_o	zero order uncertainty (due to instrument's resolution)
V	volume of fluid absorbed by porous solid [cm^3]

Greek Symbols

η	fluid viscosity [cP]
θ	contact angle [deg]
θ_W	contact angle calculated via the Washburn Method [deg]
θ_{PTFE}	contact angle between liquid and reference solid PTFE [deg]
ρ	fluid density [g/cm^3]
σ_L	liquid surface tension [mN/m]
σ_S	solid surface energy (CST) [mN/m]

σ_{SL}	interfacial surface tension between solid and liquid phases [mN/m]
σ_L^D	dispersive component of liquid surface tension [mN/m]
σ_L^P	polar component of liquid surface tension [mN/m]
σ_S^D	dispersive component of solid CST [mN/m]
σ_S^P	polar component of solid CST [mN/m]

Subscripts

c	instrument
d	design stage
L	liquid
o	zero order
P	probability
$PTFE$	Polytetrafluoroethylene
S	solid
SL	solid to liquid
v	degrees of freedom in a data set ($N-1$)
W	Washburn
x	sample
$\bar{x}$	means

Superscripts

D	dispersive
P	polar

CHAPTER 1

INTRODUCTION

Previous research by Weber, et al. [1] demonstrated that non-metallic wick-based coldplates saturated with a liquid are superior to that of metal-matrix coldplates saturated with a solid phase change material. In this study, the metallic-matrix coldplate utilized only 30 percent of the capacity of the phase-change-material (paraffin wax), while the wick-based coldplate consumed over 85 percent of the available working fluid. Additional advantages of non-metallic, wick-based coldplates include: the ability to maintain various electrical components with varying heat dissipations at a uniform temperature (an important feature for phased array radar systems), ideal for time and spatially variant heat loads, inexpensive, commercially off-the-shelf materials may be used, and light weight. Weber's study used cotton as the wick material and methanol as the working fluid. Goals for current research were to optimize the wick-based coldplate design by selecting a more robust wick material with improved surface energy and using binary liquid mixtures to enhance the wickability and thermal performance of the working fluid.

In order to maximize wicking, an ideal working fluid would have low viscosity, high surface tension and low contact angle. However, fluids with high surface tensions typically tend to produce high contact angles, conversely fluids with lower surface tension tend to generate low contact angles. Next, it would have a high heat of vaporization for maximum heat transfer. Finally, it would have freezing and boiling points that were acceptable for a wide range of applications. Table 1.1 lists the properties of the four liquids of interest; all values were taken at standard temperature and pressure [2]. Water has the highest heat of vaporization, but its surface tension is so high that it will not wick onto the ceramic porous medium of interest.

Furthermore, its freezing/boiling points would be unacceptable for most electronic cooling applications. Both methanol and ethanol have much lower surface tensions than water, which should produce favorable contact angles, plus their freezing/boiling points are much more suitable. The down side with these alcohols was that their heat of vaporization was less than half of water. FC-72 had the lowest surface tension having the potential to generate the lowest contact angle. The hope was that its superior wickability would overcome its anemic heat of vaporization.

Table 1.1 Thermophysical Properties of Working Fluids

Fluid	Surface Tension (mN/m)	Density (kg/m^3)	Viscosity (cP)	Heat of Vaporization (J/g)	Freezing Temp. (°C)	Boiling Temp. (°C)
Water	72.8	998	0.890	2260	0	100
Methanol	22.3	787	0.549	1099	-97	64.7
Ethanol	22.2	785	1.074	855	-114	78.4
FC-72	12.0	1680	0.640	88	-90	56

Data found in literature, see Figure 1.1, demonstrates the reduction in surface tension in ethanol-water mixtures with an increasing concentration of ethanol [3]. At a mass fraction of 50% the surface tension of the mixture was approaching that of pure ethanol. This impressive reduction in surface tension (and presumably contact angle) gives much promise to the use of alcohol-water mixtures. The alcohol content may be varied to achieve the desired wickability, cooling capacity and saturation temperature. These quantities were empirically determined for both ethanol-water and methanol-water mixtures.

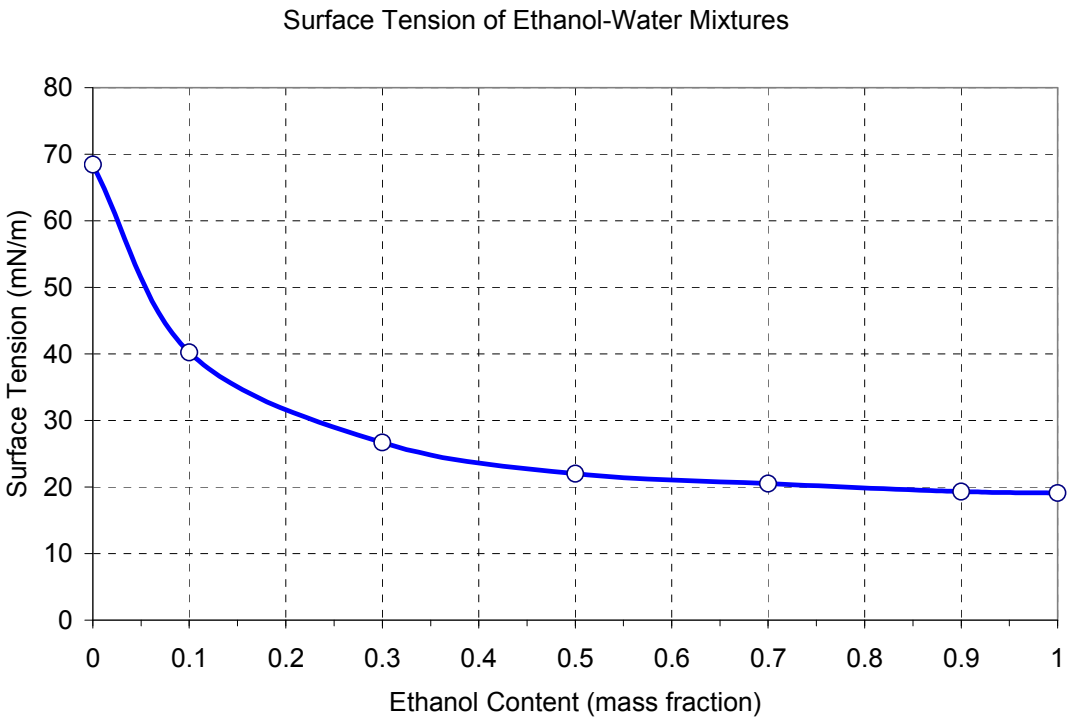

Figure 1.1 Surface Tension of Ethanol-Water Mixtures [3]

CHAPTER 2

MASS TRANSPORT WITHIN PORUS MEDIUM

Mass transport was quantified via wickability, which is the ability of a fabric or porous medium to absorb and disperse liquid. The two most commonly used empirical methods are the height [4] and weight [5] approaches. The Height approach requires measurements of the distance penetrated by a liquid into the porous medium. The weight approach requires the measurement of the increase in weight (vs. time) of the porous solid due to imbibition.

2.1 Height Approach

The height approach was by far the simpler of the two methods, thus it was implemented first. The Longitudinal Wicking “Strip” Test, illustrated in Figure 2.1, was deemed most applicable for wick-based coldplates. Standard test method DIN53924, known as the short interval test, was applied [6]. This test calls for a strip of the porous medium to be immersed into the fluid having a known initial fluid height. Once the strip of material is immersed, capillary pumping will absorb liquid into the porous medium causing the liquid to rise along the strip. Rise in fluid height was measured after duration of thirty seconds. Pure ethanol, methanol, and FC-72 were tested first, and then water was added to the alcohols in increments of 10% concentration by mass. Ceramic fiber strips, Cotronics 390 Paper, were used for these trials.

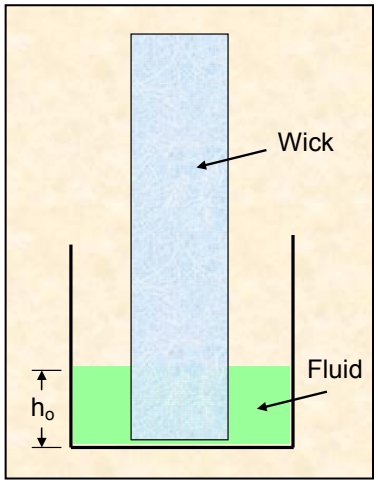

Figure 2.1 Longitudinal Wicking "Strip" Test (Height Approach)

2.1.1 Uncertainty Analysis of Height Approach

The root-sum-squares (RSS) method [7] was used to determine design stage uncertainty (u_d) of the height approach. This uncertainty includes the uncertainty inherent to the instrument (u_c) and the uncertainty due to the instrument's resolution (u_o), see Equation 2.1. According to the reference, the uncertainty due to the instrument's resolution, or the zero order uncertainty, is equal to one-half of the instrument resolution for a 95% probability. A simple scale was the only instrument required for this set of evaluations. The resolution of the scale was a tenth of a centimeter, thus the zero order uncertainty was ±0.05 cm. No other uncertainties exists for such a simple instrument, consequently the design stage uncertainty was equal to the zero order uncertainty.

$$u_d = \sqrt{u_o^2 + u_c^2} \tag{2.1}$$

$$u_o = \pm \tfrac{1}{2}\, resolution \quad (95\%) \tag{2.2}$$

$$h' = \bar{h} \pm t_{v,P} S_{\bar{x}} \tag{2.3}$$

$$S_{\bar{x}} = \frac{S_x}{\sqrt{N}} \tag{2.4}$$

$$S_x = \left(\frac{1}{N-1} \sum_{i=1}^{N} \left(h_i - \bar{h} \right)^2 \right)^{1/2} \tag{2.5}$$

$$v = N - 1 \tag{2.6}$$

Initially, a set of five tests were performed with methanol onto a 1/16 inch thick ceramic strip, see Figure 2.2. The sample average rise in height ($\bar{h}$) was 4.51 ± 0.06 cm. Data range was only slightly greater than the design stage uncertainty of ±0.05 cm, indicating that data-acquisition errors were minimal. Potential sources of data-acquisition error include: curvature of ceramic strip, non-uniform rise in fluid, and repeatability of trial duration. Using the Student-t Distribution [7], Equation 2.3, the range of the true rise in height (h') was determined to be 4.51 ± 0.043 cm for a probability of 99%. A Student-t Distribution table was listed in Appendix A.

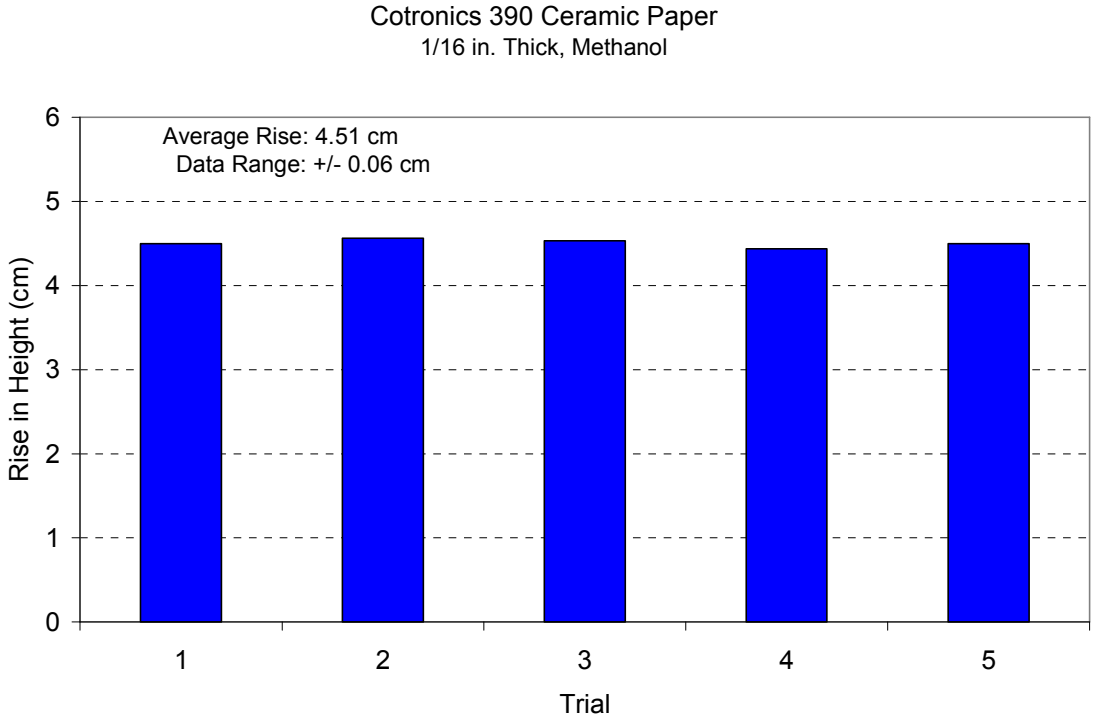

Figure 2.2 Methanol Height of Rise in Ceramic Wick

2.1.2 Effect of Ceramic Wick Thickness on Wickability

Ultimately, the goal was to have the ability to develop wick-based coldplates of various thermal capacities and thicknesses. Flexibility with the coldplate thickness is essential for integrating into various hardware platforms. In light, it was critical to understand the effect of varying the wick thickness on wickability. Two additional wick thicknesses were evaluated (five trials each) and results were compared as shown in Figure 2.3. Average rise in height for the 1/32 and 1/8 inch thick ceramic strips were 4.47 and 4.48 inches, respectively. These values fall within the range of the true rise in height of the 1/16 inch thick wick. Therefore, statistically speaking, there was no positive or adverse effect on wickability based on wick thickness for thicknesses ranging between 1/32 and 1/8 inch.

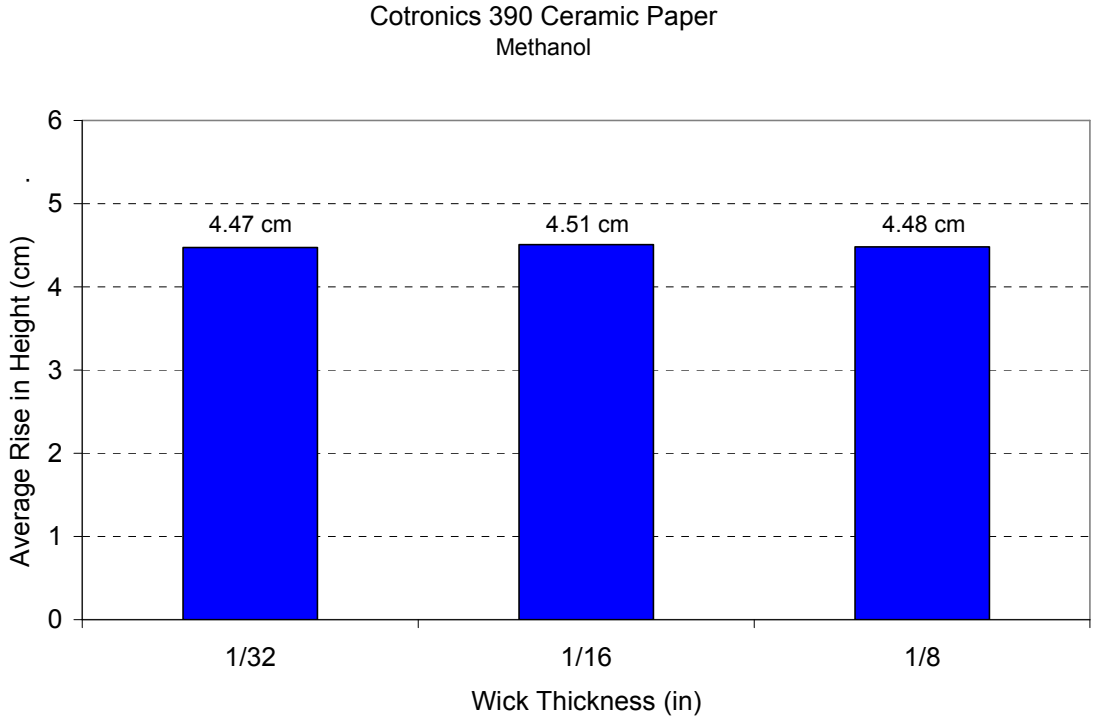

Figure 2.3 Rise in Height as a Function of Wick Thickness

2.1.3 Effect of Fluid on Wickability

Figure 2.4 displays the average rise in height (five trials each) of the three fluids in question (pure water does not wick into this ceramic due to its high surface tension). Methanol outperformed ethanol and FC-72 by 22 and 220%, respectively. Observing the Washburn Equation (2.7), which relates the predicted volume of fluid absorbed to the time in which the porous medium is in contact with the fluid [8], may explain these results.

$$V^2 = \frac{tC\sigma_L \cos\theta_W}{\eta} \qquad (2.7)$$

Methanol and ethanol have similar surface tensions, but the viscosity of methanol is roughly half of that of ethanol. This explains methanol's superior performance over ethanol, but why did the

FC-72 perform so poorly? FC-72 has a viscosity similar to that of methanol and its low surface tension should have produced a low contact angle (i.e. good wickability). The contact angle between FC-72 and the ceramic wick must be determined in order to further investigate its meager performance. This will be discussed in section 2.2.4.

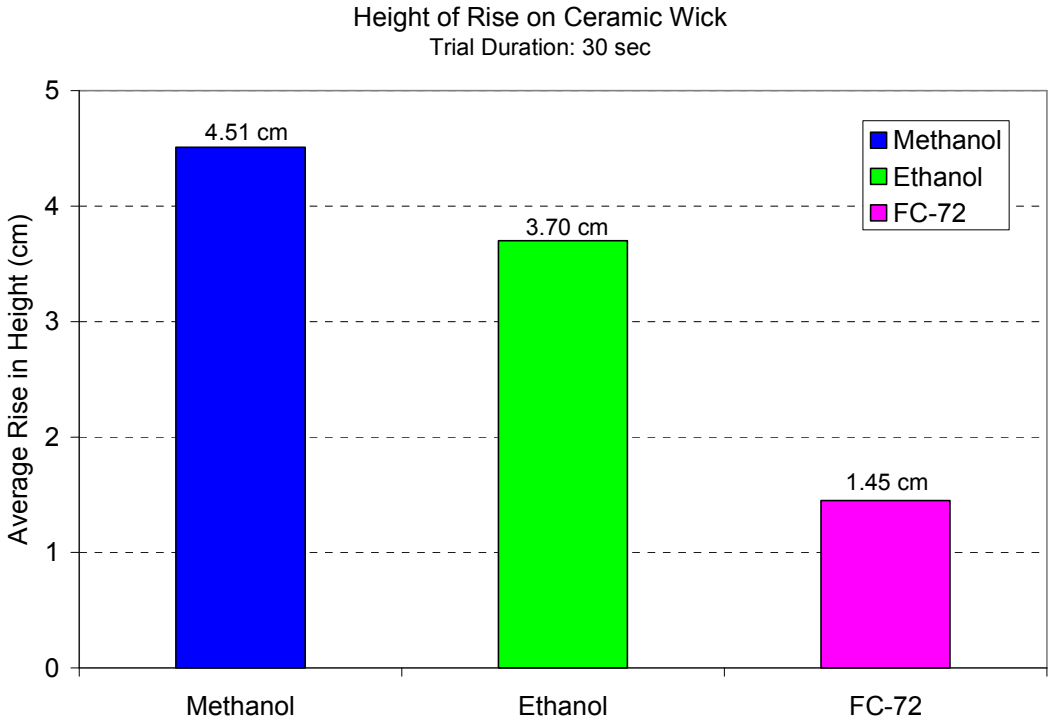

Figure 2.4 Rise in Height for Various Fluids

Figure 2.5 displays the rise in height of ethanol-water mixtures within a ceramic fiber medium. At a mass fraction of zero the liquid was pure water, which did not wick at all onto the ceramic fibers. This was likely due to water's high surface tension, which was presumably higher than the critical surface energy of the ceramic wick. Ethanol was added to the solution until wicking was observed, which occurred approximately at an ethanol concentration of 15%

by mass. As the concentration of ethanol was increased the wickability increased sharply until reaching a mass fraction of 40%. Interestingly enough the rise in height was relatively constant between 40 and 80% concentration. The slight decrease is surface tension within this region does not explain this behavior. Something must be occurring with the contact angle and/or viscosity in order to explain this flat region. Beyond an 80% concentration the rise in height resumed increasing.

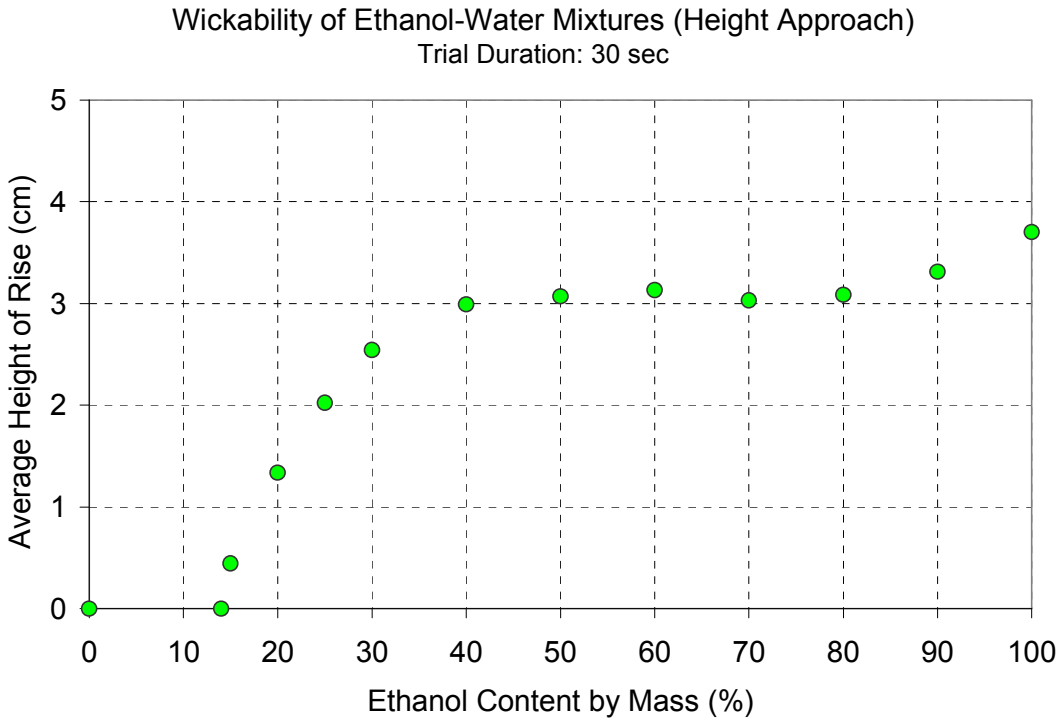

Figure 2.5 Wickability of Ethanol-Water Mixtures (Height Approach)

Figure 2.6 includes the wickability of methanol-water mixtures, whose behavior was significantly different from that of ethanol-water. First, discernable wicking does not occur until a methanol concentration of 30%; double that of ethanol-water. For methanol the sharp increase in wickability was shifted to the right by 20% concentration. Next, the methanol-water

curve was much more linear, suggesting wickability always increases with decreasing surface tension and contact angle. This allows the wickability of methanol-water to surpass that of ethanol water beyond concentrations of 60%. Finally, maximum wickability was obtained with pure methanol, 22% greater than that of pure ethanol.

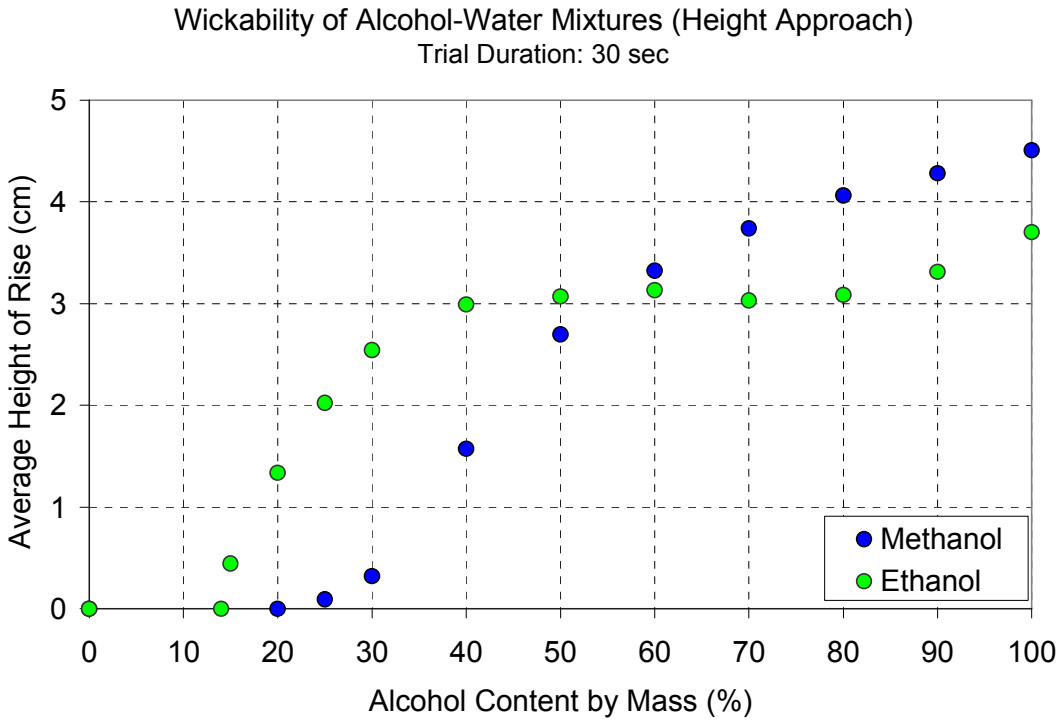

Figure 2.6 Wickability of Alcohol-Water Mixtures (Height Approach)

2.2 Weight Approach

The weight approach [5] was much more involved and required the use of a highly sensitive tensiometer to measure the mass absorbed into the porous medium over time. Furthermore, the following fluid properties had to be measured: surface tension, density, and viscosity. Once the fluid properties were quantified, the Washburn Method [8] was employed to determine the contact angle. Normally, contact angles are measured optically by placing a drop

of the liquid onto the solid. However, since the solid in this case was porous, the optical or geometric technique was not possible. Hence, the use of the Washburn Method, which is specific for determining contact angles between a liquid and a porous medium. Contact angles measured using the Washburn and optical techniques should agree within the expected empirical uncertainty. Finally, in order to make comparisons to the height approach, the predicted volume of fluid absorbed for a fixed duration was computed.

2.2.1 Surface Tension Measurements

Surface tension measurements were made via the Wilhelmy Plate Method [15], which is illustrated in Figure 2.7. Mathematically, this method is characterized by Equation 2.8, which relates the surface tension to the force generated by the contact between a thin plate and the test fluid. Roughened platinum is typically used because its high surface energy produces a zero degree contact angle with most fluids. Once the contact angle term is eliminated the surface tension is simply the ratio between the force and wetted length. This wetted length is solely based on the geometry of the thin plate.

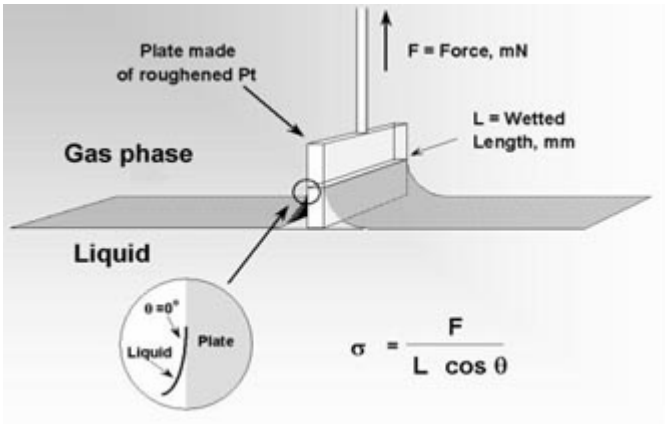

Figure 2.7 Illustration of the Wilhelmy Plate Method

$$\sigma = \frac{F}{L\cos\theta} \tag{2.8}$$

A Kruss K100 Tensiometer, illustrated in Figure 2.8, was used for these measurements. It has a reported surface tension range of 1-1000 mN/m with a resolution of 0.01 mN/m. In order to gain confidence in making these measurements, initial tests were performed on methanol and ethanol, which have well established reference values. Five trials of each fluid were performed and resulting values are listed in Table 2.1. The average measured values were within one percent of the reference values. Furthermore, for a probability of 99% the true mean was 22.44 ± 0.017 and 22.31 ± 0.014 mN/m for methanol and ethanol, respectively.

Figure 2.8 Kruss K100 Tensiometer

Table 2.1 Surface Tension Measurements of Methanol and Ethanol

	Surface Tension (mN/m)	
	Methanol	**Ethanol**
Trial 1	22.46	22.30
Trial 2	22.42	22.32
Trial 3	22.45	22.29
Trial 4	22.42	22.33
Trial 5	22.46	22.32
Measured Average	22.44	22.31
Published Value [2]	22.29	22.22
% Difference	0.7%	0.4%

Once confidence was established in performing surface tension measurements, the surface tension of methanol-water and ethanol-water mixtures was measured for the full concentration range. Average surface tension measurements are displayed in Figure 2.9. As anticipated the surface tension of the mixtures decreased with increasing alcohol concentration. Ethanol-water mixtures produced slightly lower surface tensions than methanol-water mixtures, however the difference was minimal. This data certainly does not explain the strange wickability behavior of the ethanol-waters mixtures discussed in the previous chapter.

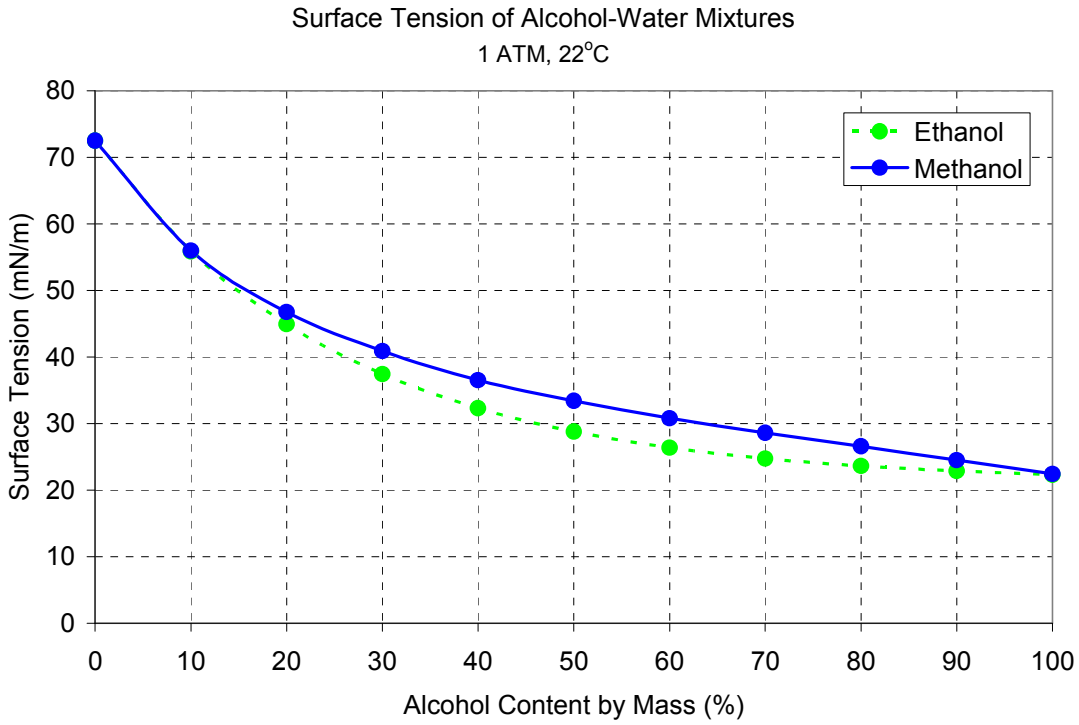

Figure 2.9 Measured Surface Tensions of Alcohol-Water Mixtures

2.2.2 Density Measurements

An Anton Paar DMA 38 Meter, illustrated in Figure 2.10, was used to measure the densities of the liquids. It has a reported range of 0 to 3000 kg/m^3, accuracy of ±1 kg/m^3, and repeatability of ±0.2 kg/m^3. This instrument operates on the Oscillating U-tube Principle [16], which states that the resonant frequency of an oscillating tube is inversely proportional to the square root of its mass, see Equation 2.9. The oscillating u-tube acts as a mass-spring system with the arms of the tube acting as springs.

$$f = \frac{1}{\sqrt{m}} \tag{2.9}$$

The hollow u-tube has a known volume, which was filled with the test liquids. The fluid mass is calculated, within the circuitry of the device, using the measured resonant frequency. Next, using the known volume, the density is computed. Again, to gain practice with this instrument, pure methanol and ethanol were tested first. Five trials of each liquid were performed and the resulting densities are listed in Table 2.2. For methanol the measured average density was 791.2 ± 1.1 kg/m^3, not quite the repeatability reported by the vendor. Assuming a probability of 99%, the true mean was 791.2 ± 0.8 kg/m^3. Measured and true mean densities for ethanol were 788.7 ± 0.6 kg/m^3 and 788.7± 0.4 kg/m^3, respectively. Mean density values for both liquids were well within one percent of the published values.

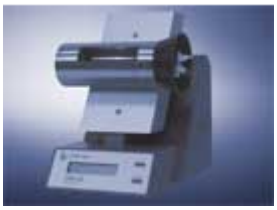

Figure 2.10 Anton Paar DMA 38 Density Meter

Table 2.2 Density Measurements of Methanol and Ethanol

	Density (kg/m^3)	
	Methanol	**Ethanol**
Trial 1	790.1	788.9
Trial 2	791.9	788.1
Trial 3	792.1	789.2
Trial 4	791.6	789.0
Trial 5	790.2	788.5
Measured Average	791.2	788.7
Published Value [2]	787	785
% Difference	0.6%	0.5%

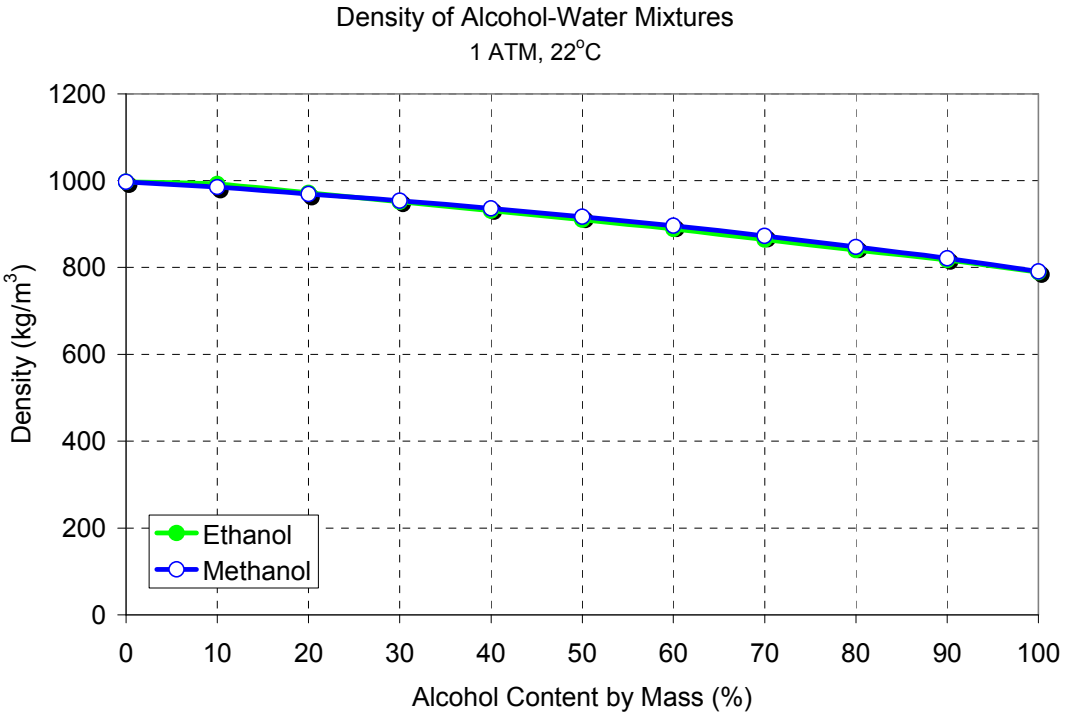

Figure 2.11 Measured Densities of Alcohol-Water Mixtures

Next, the densities of methanol-water and ethanol-water mixtures were measured; results are displayed in Figure 2.11. Interestingly enough, the densities of these mixtures were for all intents and purposes identical for the full alcohol concentration range. Again, this data provides no insight into the non-linear wickability behavior of the ethanol-water mixtures.

2.2.3 Viscosity Measurements

A Gilmont 100, a low shear falling ball viscometer, was employed to perform the viscosity measurements, see Figure 2.12. Test procedures were straightforward. The glass tubing was filled with the test liquid, and then the tube was inverted to allow the ball to enter a Teflon screw, which served as the release mechanism. This ball-release device was originally sealed with a Viton® O-ring, however Viton® tends to react with methanol; thus, it was replaced with an ethylene-propylene-diene rubber (EPDM) O-ring, which is chemically resistant

to solvents including alcohols. Next, the tube was restored to the normal position and a knob was turned to release ball. Table 2.3 lists the various available ball materials and their corresponding viscosity range. Since the reported viscosity of methanol and ethanol was 0.549 and 1.074 cP, respectively, the glass ball was used for all evaluations. Next, the time of descent was measured for the ball falling between the two reference marks. Each ball comes with its own calibration curve, which relates time of descent to viscosity. The reported maximum repeatability of this device was ±1.0%.

Figure 2.12 Gilmont 100 Falling Fall Viscometer

Table 2.3 Viscosity Range for Various Ball Materials

Ball Material	Calibrated Test Range (cP)
Glass	0.2 to 3.0
Stainless Steal	1.0 to 10.0
Tantalum	2.0 to 20.0

Once again, both methanol and ethanol were evaluated first in order to gain experience using this apparatus. Five trials of each liquid were performed and resulting viscosities are listed in Table 2.4. For methanol the sample average viscosity was 0.557 ± 0.002 cP (± 0.4%), which was well within the reported repeatability of this viscometer. For an assigned probability of 99%, the true mean value was 0.557 ± 0.0011 cP. Comparing the measured mean to the published value reveals a difference within two percent, which was quite acceptable. For ethanol the sample and true mean values were 1.071 ± 0.002 (± 0.2%) and 1.071 ± 0.0012 cP, respectively. Ethanol's measured viscosity was well within one percent of the reference value.

Table 2.4 Viscosity Measurements of Methanol and Ethanol

	Viscosity (cP)	
	Methanol	**Ethanol**
Trial 1	0.558	1.072
Trial 2	0.555	1.070
Trial 3	0.556	1.070
Trial 4	0.556	1.073
Trial 5	0.558	1.070
Measured Average	0.557	1.071
Published Value [2]	0.549	1.074
% Difference	1.5%	0.3%

Once proficiency was established in performing viscosity measurements, the viscosity of both methanol-water and ethanol-water mixtures were obtained, and resulting average values were plotted as shown in Figure 2.13. Interestingly enough, the viscosity goes through a maximum at the mid-range of alcohol concentration. For the ethanol-water mixtures the maximum viscosity was 140% greater than that of water. Since the viscosity of pure methanol was roughly half of that of water, the maximum viscosity generated by the methanol-water mixtures was not as dramatic, measuring 70% greater than that of water.

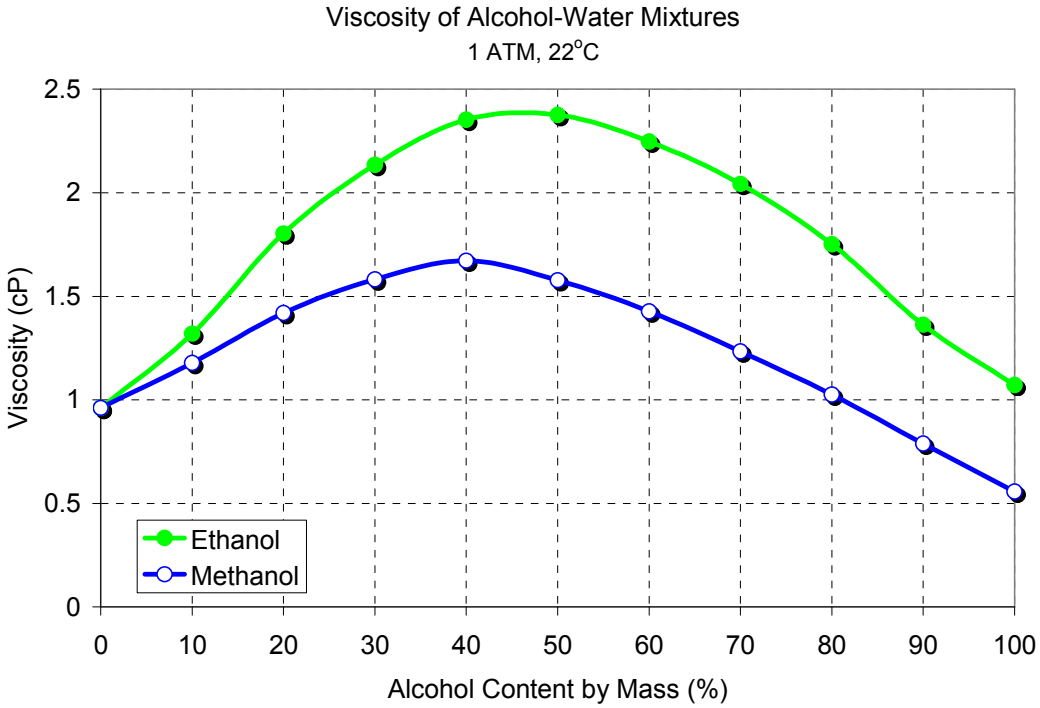

Figure 2.13 Measured Viscosities of Alcohol-Water Mixtures

According to the Washburn Theory, see Equation 2.7, the volume of fluid absorbed into a porous medium is inversely proportional to the fluid's viscosity. Therefore, these viscosity maxima adversely affect the wickability of the alcohol-water mixtures. This effect was much more pronounced for the ethanol-water mixtures and explains the flat region in wickability between 40 and 80% ethanol concentration (see Figure 2.6). As the ethanol concentration increased, the surface tension decreased, but the viscosity increased; thus, the effect of each parameter opposed each other resulting in constant wickability. For methanol, the viscosity maximum was not as pronounced; allowing the wickability to increase fairly linearly with increasing methanol concentration, see Figure 2.14.

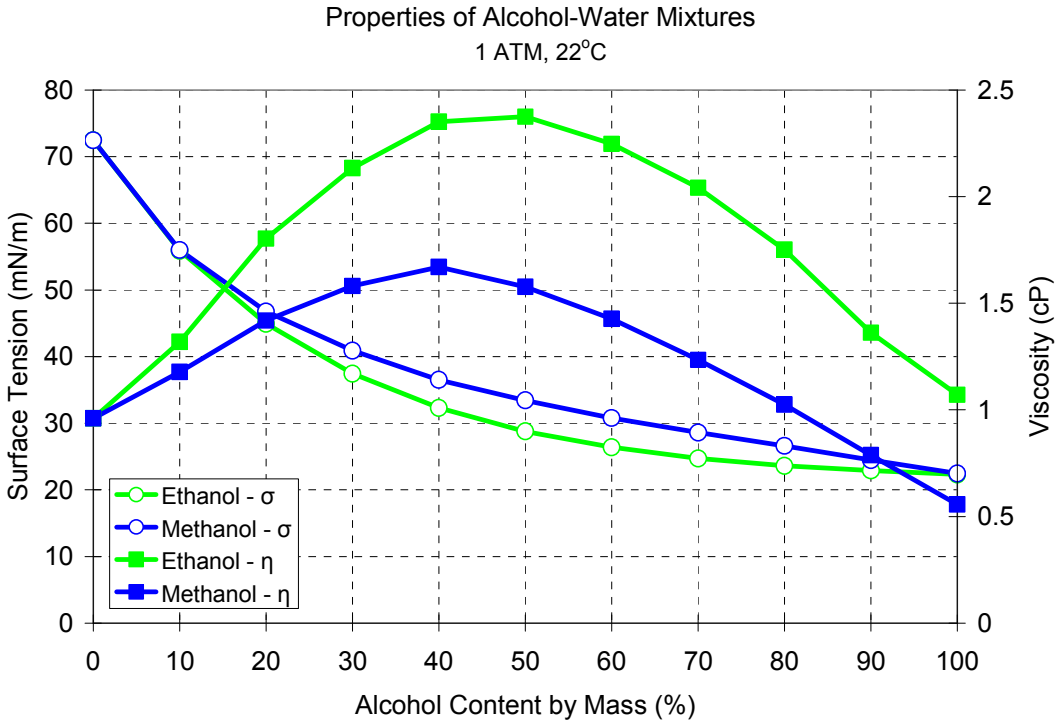

Figure 2.14 Property Comparison of Alcohol-Water Mixtures

2.2.4 Contact Angle Measurement Using the Washburn Method

Traditionally, the contact angle formed between a liquid and solid is measured optically by placing a drop of the sample liquid onto the solid and measuring the angle formed between the horizontal and the tangent of the bubble starting at the interface of the three phases, see Figure 2.15. However, if the solid in question happens to be a porous solid, then this approach will not work since the drop of liquid will be absorbed. In order to calculate a contact angle (θ_W) between a liquid and a porous solid, the Washburn Method [8] must be employed.

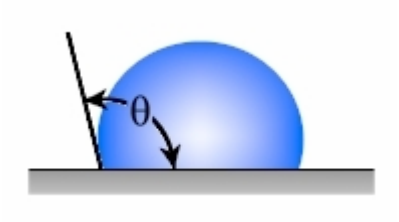

Figure 2.15 Optical Contact Angle Measurement Technique

The Washburn Method states that once a porous solid is brought into contact with a liquid, the rise of the liquid in the pores of the solid will obey Equation 2.10, which has been rearranged to solve for the contact angle.

$$\cos\theta_W = \frac{m^2}{t}\frac{\eta}{C\rho^2\sigma} \tag{2.10}$$

Thus, the contact angle is a function of the density, viscosity, and surface tension of the liquid plus a material constant (C), which characterizes the solid (i.e. porosity, surface energy, pore structure, etc.). Once the material properties have been determined, the porous solid is placed in contact with the test liquid and the mass absorbed is recorded over time, see Figure 2.16. The Kruss K100 Tensiometer, illustrated in Figure 2.8, was used to track the mass absorbed by the ceramic wick over time. Typically, the mass squared is plotted vs. time so that the resulting slope of the curve (m^2/t) will provide the term lacking in the Washburn Equation. Figure 2.17 illustrates a typical mass squared vs. time plot. Initially, while the liquid is being absorbed the curve is linear, however once the sample strip begins to saturate the slope of the curve begins to level off and asymptotically approaches zero. Consequently, only the initial and linear portion of the curve was considered, and the resulting slope was used to calculate the contact angle.

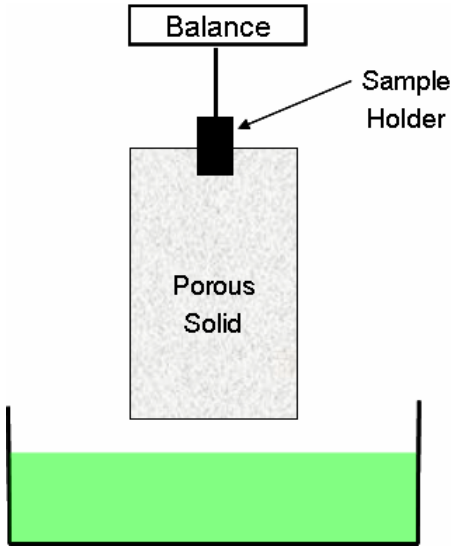

Figure 2.16 Washburn Method for Calculating Contact Angle

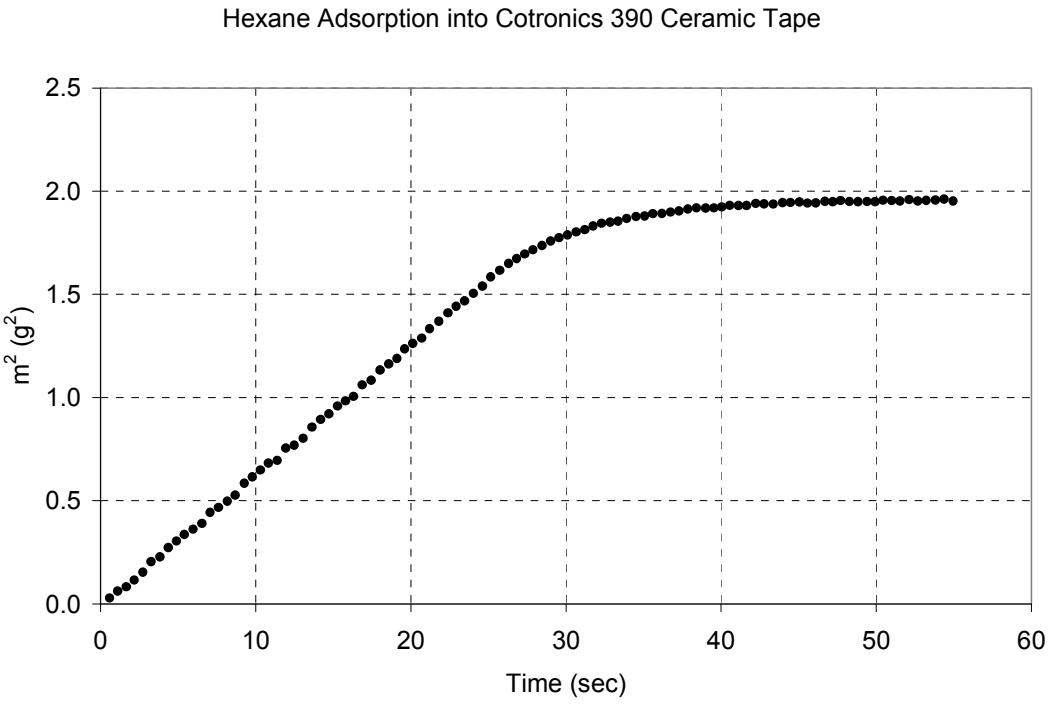

Figure 2.17 Typical Mass Absorbed vs. Time Plot (Hexane)

Properties of the liquids were reported in previous sections, however the material constant (C) for the ceramic wick has yet to be determined. The approach for determining the material constant was as follows. Low surface tension liquids known to form a zero degree contact angle with many solids were selected and tested with the ceramic wick. Liquids hexane (σ = 18.40 mN/m) and pentane (σ = 15.49 mN/m) were selected to determine the material constant. First, hexane was placed in contact with the ceramic wick, and the plot in Figure 2.17 was generated. Assuming a contact angle of zero, the Washburn Equation reduces to:

$$C = \frac{m^2}{t}\frac{\eta}{\rho^2\sigma} \qquad (2.11)$$

This test was repeated and the resulting material constants are listed in Table 2.5. Both material constants for Hexane were in good agreement; the scatter was less than 0.1%. How can one be assured that the zero degree contact angle assumption was valid? The Washburn Method suggests evaluating the material with another liquid with a lower surface tension, and if the resulting value is the same as the first, then one can safely assume that the contact angle was zero degrees in both cases. Pentane was then used to determine the material constant, and the resulting values are also listed in Table 2.5. Material constants generated by Pentane were in good agreement with each other and with those generated by the Hexane. Had this not been the case, a third or fourth probe liquid (with even lower surface tension) would have been introduced until values for the material constant ceased to vary. Since the resulting values were in good agreement, an average value was computed and used for the remainder of the Washburn calculations.

Table 2.5 Material Constant for Ceramic Wick

Probe Liquid	Material Constant (cm^5)
Hexane (Trial 1)	2.6267×10^{-5}
Hexane (Trial 2)	2.6284×10^{-5}
Pentane (Trial 1)	2.6297×10^{-5}
Pentane (Trial 2)	2.6271×10^{-5}
Average	2.6280×10^{-5}

Now that the properties of the liquids and the material constant of the porous solid have been determined, the binary mixtures of methanol-water and ethanol-water were evaluated in duplicate, and the resulting average contact angles were plotted in Figure 2.18. Contact angles for the alcohol-water mixtures followed the general tendency of lower surface tension liquids producing lower contact angles. Next, FC-72 was tested, and the resulting contact angle was 66.6 degrees, which goes completely against the previous trend. This high contact angle for FC-72 at least quantifies its poor wickability, but why is it so? Having such a low surface tension, why does FC-72 generate such a high contact angle with the ceramic wick? In order to investigate this further, a detailed surface energy analysis was performed; the results are discussed in the next chapter.

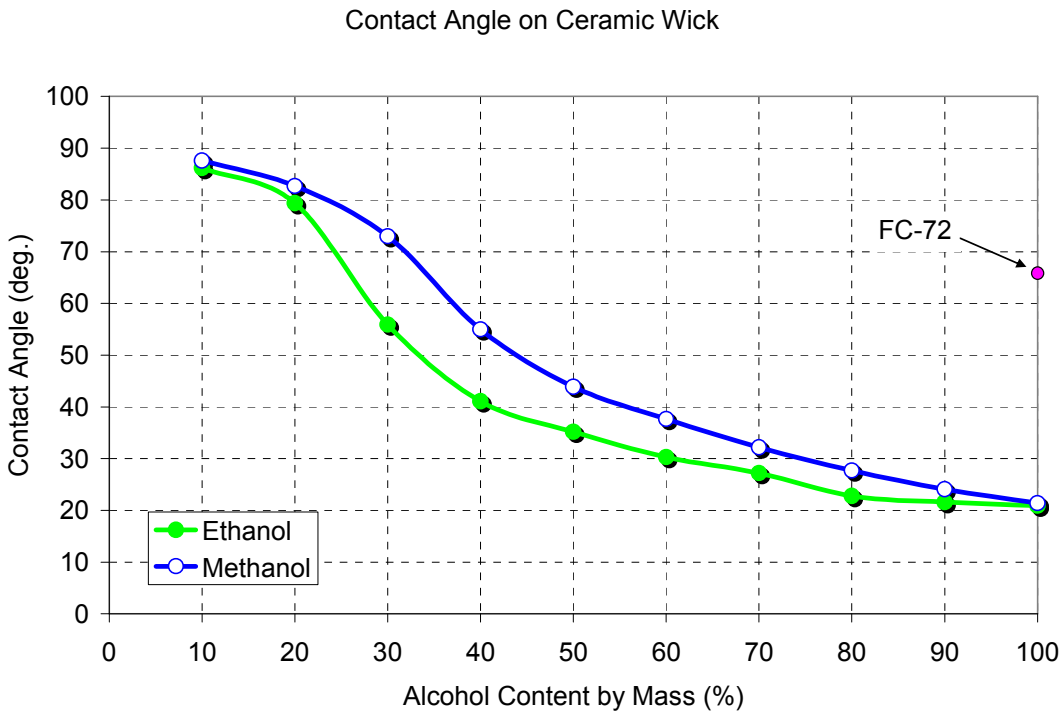

Figure 2.18 Contact Angles of Alcohol-Water Mixtures and FC-72 on Ceramic Wick

Now that the contact angles have been determined, the predicted volume of liquid absorbed for a fixed duration may be computed via the Washburn Equation 2.7. Trial duration of 30 seconds was selected in order to make comparisons with the height approach. Figure 2.19 displays the predicted volume of liquid absorbed for the alcohol-water binary mixtures. Next, the predicted volume absorbed was converted to height of rise in order to directly compare with the height approach and comparisons are illustrated in Figures 2.20-21. Note that some liquid absorption was predicted at alcohol concentration levels as low as 10%. This differs form the results obtained in the height approach where imbibition did not occur until 15 and 30% concentration for ethanol and methanol, respectively. This and other differences between the two approaches have been well documented [17, 18]. With the height approach, only the amount of liquid observed rising into the wick was accounted for; therefore only the

amount of liquid imbibition was measured. However, with the weight approach the force that was being recorded by the tensiometer was the superposition of the imbibition and the force that appears once contact between solid and liquid was established. For example, pure water did not wick at all into the ceramic, yet its high surface tension would have tugged on the wick, enough to falsely register a weight absorbed using the tensiometer.

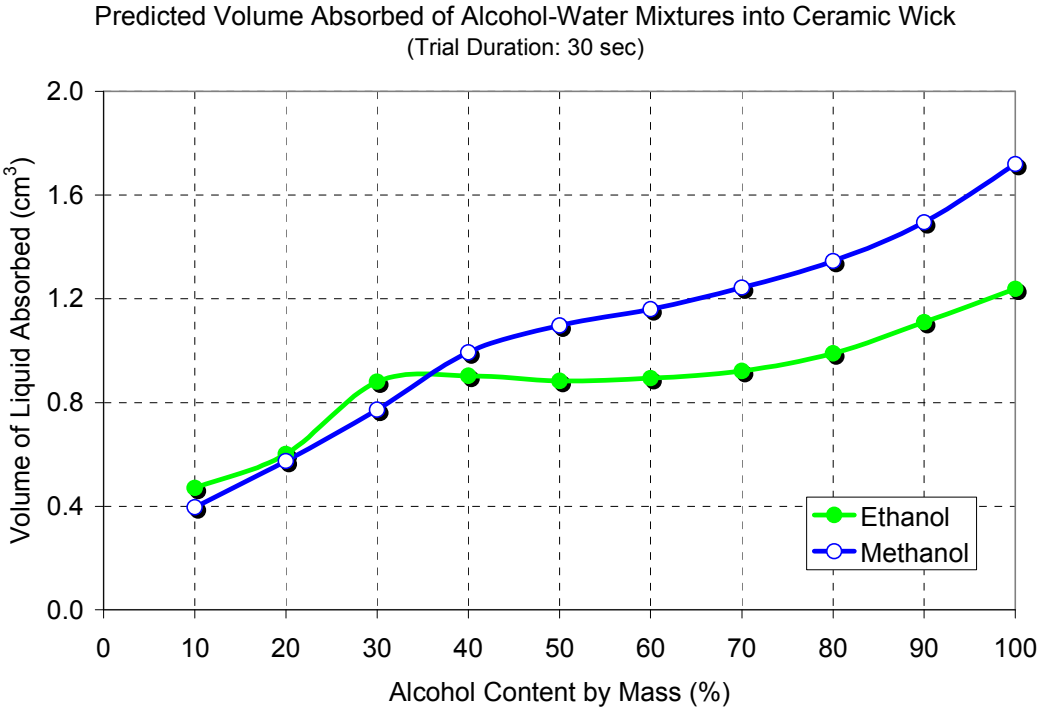

Figure 2.19 Predicted Volume Absorbed (Weight Approach)

For the methanol-water mixtures the weight approach also produced a fairly linear increase in wickability, as a function of methanol concentration. Furthermore, for the ethanol-water mixtures, the weight approach confirmed the flat region in the wickability curve, except that it was shifted to the left by 10% concentration. This contact angle data and predicted

volume absorbed only confirms that the flat region was due to the viscosity maximum generated by the ethanol-water mixtures.

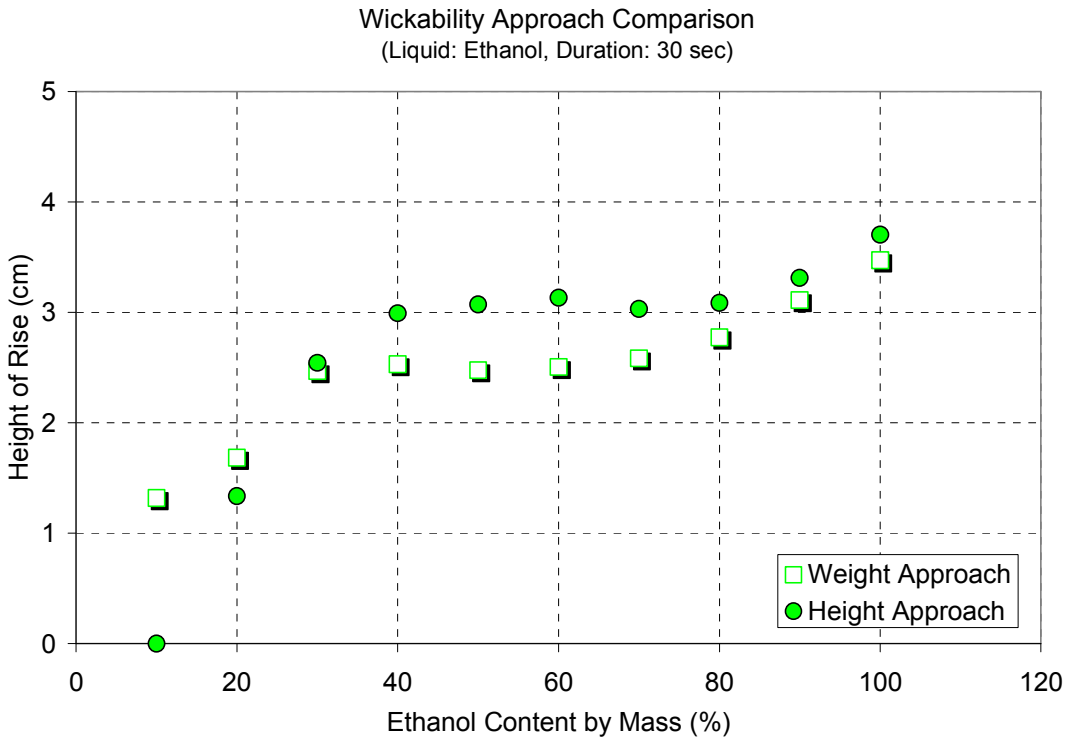

Figure 2.20 Wickability Approach Comparison (Ethanol)

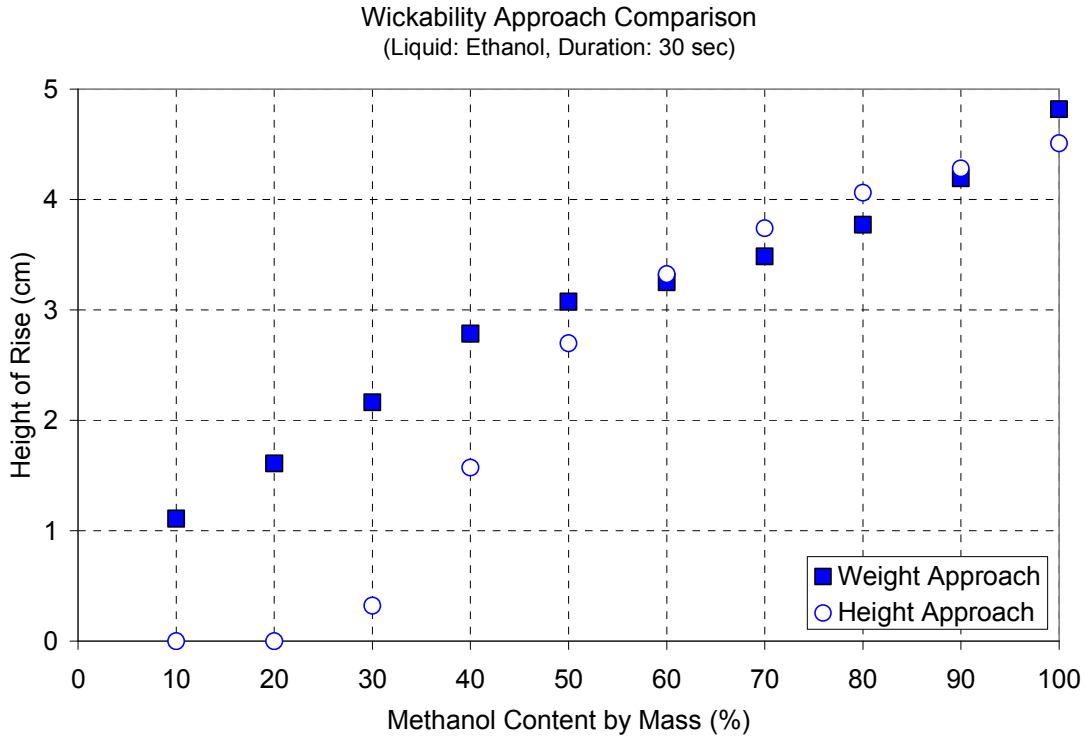

Figure 2.21 Wickability Approach Comparison (Methanol)

2.3 Mass Transport Summary

Mass transport within the porous medium was evaluated using both the height and weight approaches. Moreover, material properties of the test liquids were measured. Finally, the contact angle between the test liquids and the proposed ceramic wick was determined. This parameter is often used to describe the wickability of a liquid onto a porous solid. Methanol's superior wickability over ethanol was due to its lower viscosity. FC-72 had poor wickability and formed a large contact angle with the ceramic wick in spite of its attractive surface tension. The wickability of ethanol-water mixtures increased non-linearly with increasing concentrations of ethanol. In fact, wickability was relatively constant through the midrange in alcohol concentration. This phenomenon was confirmed by both test methods and was likely due to the generated viscosity maximum.

CHAPTER 3

SURFACE ENERGY ANALYSIS

In order to further investigate the large contact angle calculated between FC-72 and the ceramic wick (i.e. poor wickability) a surface energy analysis was performed. Wickability is dominated by the interfacial interactions between the liquid and porous solid. This process involves intermolecular interactions, which may be modeled by a number of surface energy theories such as Zisman [9], Owens-Wendt [10], Fowkes [11], van Oss [12], etc. A number of surface energy theories exist because none is universal. Generally, the surface energy of a liquid is characterized by its surface tension, which quantifies the amount of energy (Joules) required to stretch the liquid per unit area (meter^2). Surface energy of a solid, also known as the critical surface tension (CST), is a measure of how much energy is available at the surface of the solid to pull the liquid. The CST may not be directly measured; its value is derived from a series of liquid-solid contact angles. Both the Zisman and Owens-Wendt Theories were used to investigate the surface energy of the ceramic wick and working fluids.

3.1 Zisman Theory

The Zisman Theory is the most commonly used definition of surface energy. Zisman states that the surface energy of a solid is equal to the surface tension of the highest surface tension liquid that will completely wet the solid (i.e. form a zero degree contact angle). This is based on the assumption that contact angle decreases as the surface tension of the liquid decreases. In order to determine the CST of the ceramic wick, a Zisman Plot was generated, see Figure 3.1. The cosine of the contact angles ($\cos\theta_W$, listed in the previous chapter) was plotted versus the surface tensions of the corresponding liquids. A linear curve fit was drawn to

represent the bulk of the data. Only the two points representing pentane and n-hexane, which produced contact angles of zero, were not included in the curve fit.

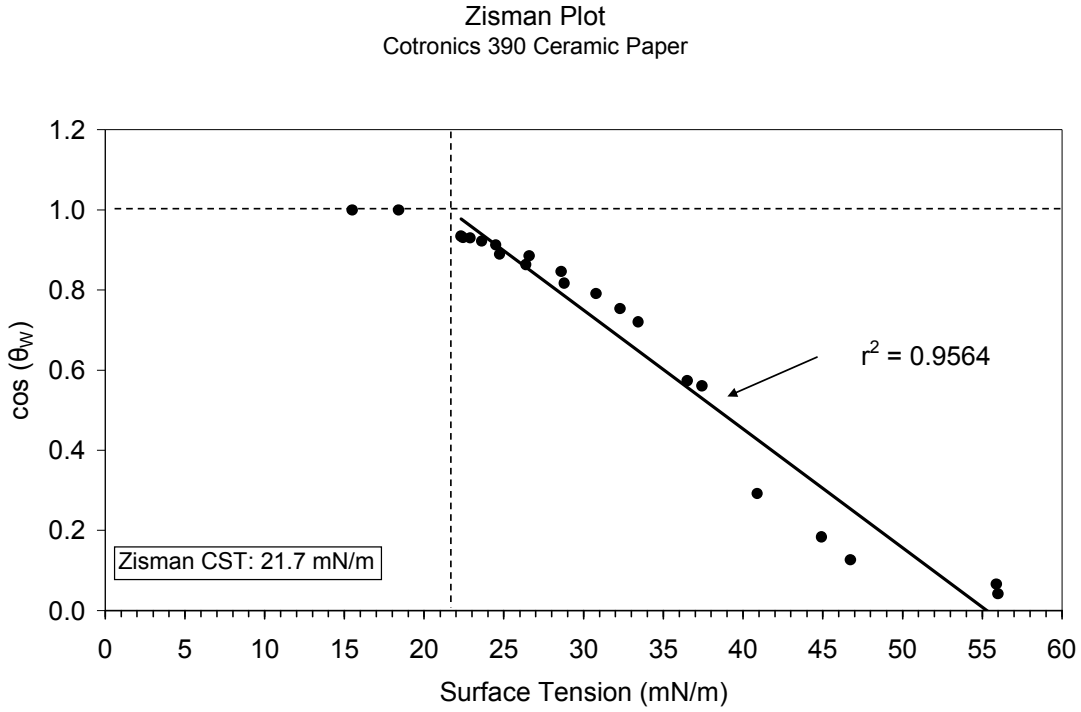

Figure 3.1 Zisman Plot of Ceramic Wick

The resulting linear coefficient (r^2 = 0.9564) does not lend itself to much confidence that the data fits well with this theory. CTS is indicated by the point at which the fitted line intersects a value of one for cos θ_W. The resulting CST for the ceramic wick was 21.7 mN/m. So, according to the Zisman Theory, any liquid with a surface tension less than 21.7 mN/m should produce a zero degree contact angle with this ceramic wick. In the previous chapter we found that FC-72, having a surface tension of 12 mN/m, generated a contact angle of 66.6° with this wick material. Consequently, this particular theory was not appropriate for the ceramic wicking material.

3.2 Owens-Wendt Theory

For moderately polar solids such as ceramics, the Owens-Wendt Theory [10] was the most appropriate. This theory requires the surface energy to be divided into two components, one part dispersive (σ^D) and one part polar (σ^P). Overall surface energy is simply the sum of the two components (Equations 3.1 and 3.2). The dispersive component accounts for non-polar van der Waals type molecular interactions, while the polar component accounts for all polar interactions, including dipole-dipole, dipole-induced dipole, and hydrogen bonding interactions. Since polar bonds are stronger than non-polar van der Waals forces, the polar component has a greater influence on the overall performance. Mathematically, this theory is based on the Good (3.3) [11] and Young (3.4) equations, which are combined and rearranged to form the Owens-Wendt equation (3.5). This equation is in linear form with the x-term being only a function of the liquid surface tensions. The y-term is a function of the liquid surface tensions and the contact angle between the liquid and the solid. If the overall surface tension and its two components are known for a series of liquids, they may be graphed to produce an Owens-Wendt Plot. Theoretically, a straight line would be generated, with the slope producing the polar component of the solid surface energy and the y-intercept yielding the dispersive component.

$$\sigma_S = \sigma_S^D + \sigma_S^P \tag{3.1}$$

$$\sigma_L = \sigma_L^D + \sigma_L^P \tag{3.2}$$

$$\sigma_{SL} = \sigma_S + \sigma_L - 2\left(\sigma_L^D \sigma_S^D\right)^{1/2} - 2\left(\sigma_L^P \sigma_S^P\right)^{1/2} \tag{3.3}$$

$$\sigma_S = \sigma_{SL} + \sigma_L \cos\theta \tag{3.4}$$

$$\frac{\sigma_L\left(\cos\theta_W + 1\right)}{2\left(\sigma_L^D\right)^{1/2}} = \left(\sigma_S^P\right)^{1/2} \frac{\left(\sigma_L^P\right)^{1/2}}{\left(\sigma_L^D\right)^{1/2}} + \left(\sigma_S^D\right)^{1/2} \tag{3.5}$$

y = m x + b

Components of the liquid surface tension were measured with the use of a reference solid, PTFE, which is known to have no polar interactions. Its overall surface energy is 18.0 mN/m (i.e. σ_S = 18.0 mN/m, σ_S^P = 0 mN/m, and σ_S^D = 18.0 mN/m). Inserting these values into Equation (3.5) yields:

$$\sigma_L^D = \frac{(\sigma_L)^2(\cos\theta_{PTFE}+1)^2}{72} \tag{3.6}$$

With the overall surface tension, σ_L, already measured for various alcohol-water mixtures (Figure 1.1), the only unknown in Equation (3.6) was the contact angle between these mixtures and the reference solid, θ_{PTFE}. These contact angles were measured optically using a goniometer and were used to calculate the surface tension components of the working fluids.

3.2.1 Uncertainty Analysis of Goniometer

A First Ten Angstroms (FTA) 1000 Goniometer, see Figure 3.2, was used to optically measure the contact angle between the test liquids and PTFE. The manufacturer reports an instrument resolution of 0.01 degrees and an error of ±2.5%. The contact angle would have to be less than 5 degrees in order for the error due to the resolution to become significant. Consequently, the design stage error of this instrument was assumed to be ±2.5%.

A liquid dropper was used to place a drop of liquid onto the target solid. Next, the lens of the goniometer was adjusted until the droplet was in focus. Next, an image of the droplet was captured an imported into the goniometer's proprietary software. This software automatically generated a mathematical representation of the droplet shape. This curve fit is displayed in Figure 3.3; it is the yellow trace along the curvature of the droplet. Furthermore, the base dimension of the droplet is represented by the cyan line. The code allows for various mathematical models, which may be used to represent the droplet's geometry. Selection of an inappropriate mathematical formula may results in significant error. The two geometry settings used for this study were the spherical drop geometry and the Lapace-Young Equation. After

some trial and error it was noted that for contact angles near 90 degrees, the spherical equation was most accurate and for $100° \leq \theta \leq 80°$ the Lapace-Young Equation was best.

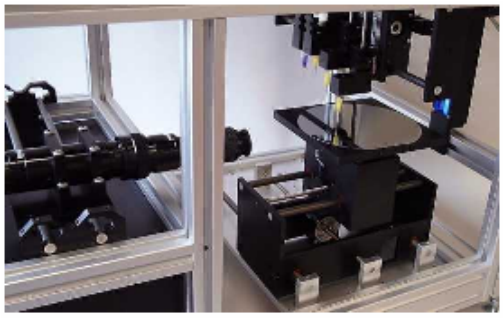

Figure 3.2 FTA 1000 Goniometer

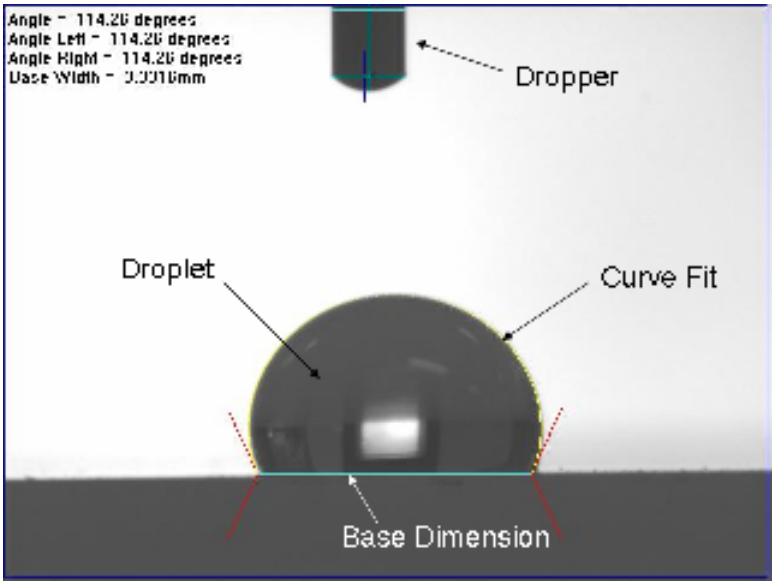

Figure 3.3 Mathematical Representation of Droplet

Next, the contact angle of pure distilled water on pure PTFE was measured five times and the resulting images and contact angles are displayed in Figure 3.4. Sample contact angle average was 113.1° ± 1.6° (or ± 1.4%), which was well within the reported error of ±2.5%. For a 99% confidence, the true mean was calculated to be 113.1° ± 1.0°. This was in very good agreement with the published value [19] of 113.7°.

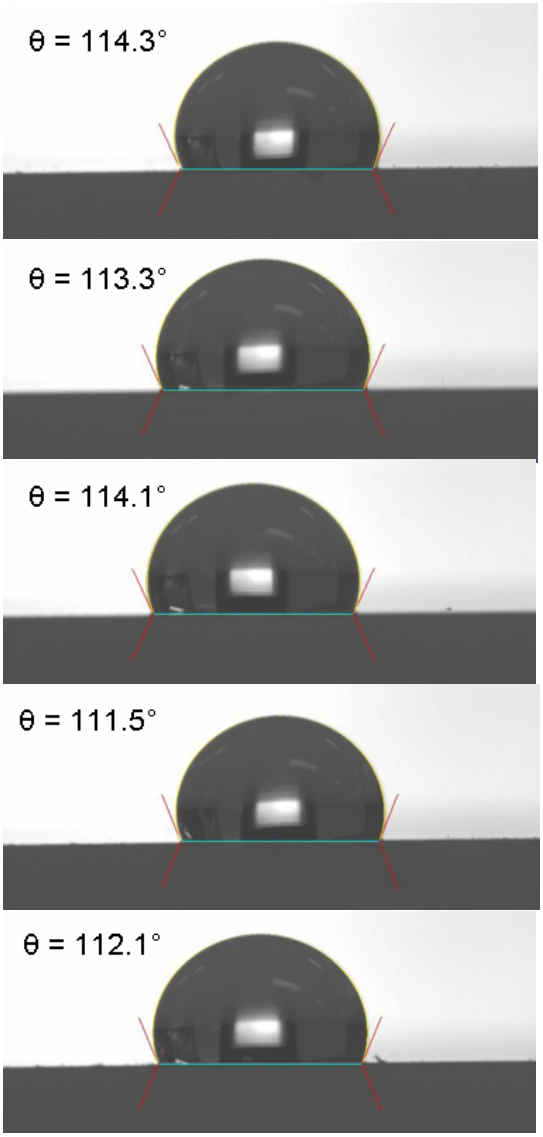

Figure 3.4 Droplet Images of Water on PTFE

3.2.2 Optically Measured Contact Angle Results

Once confidence was established in using the goniometer, contact angles were measured for the various working fluids on pure PTFE and the results are displayed in Figures 3.5-3.7. Figure 3.5 compares the resulting contact angles for water, methanol, ethanol, and FC-72 on pure PTFE. As expected, water generated the largest contact angle, while the alcohols produced greatly reduced angles, and FC-72 developed a very small angle. Figure 3.6 illustrates the contact angles formed by ethanol-water mixtures. As the ethanol concentration increased the contact angle decreased. Similarly, Figure 3.7 shows the same trend for the methanol-water mixtures.

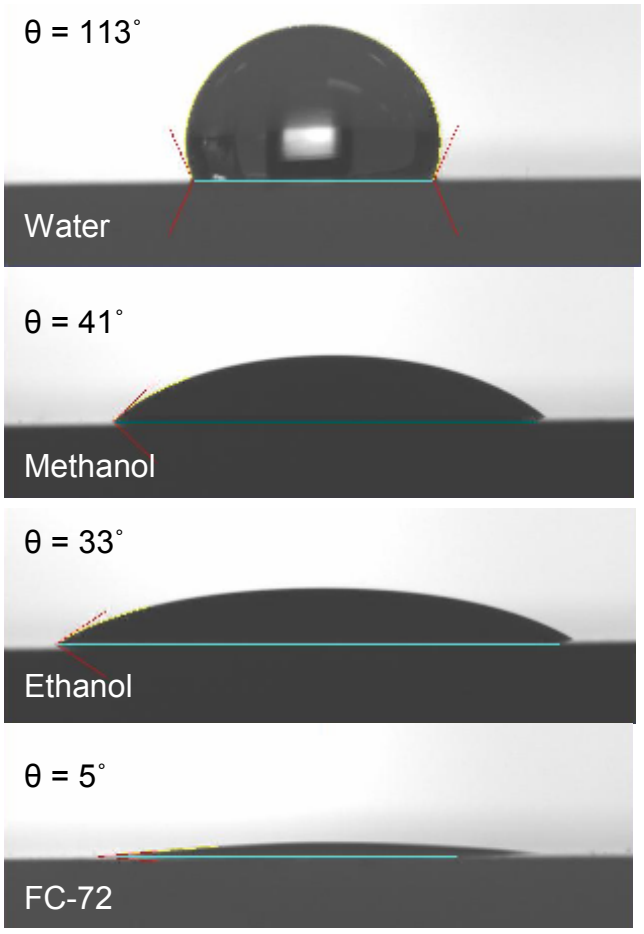

Figure 3.5 Measured Contact Angles between Liquids and PTFE

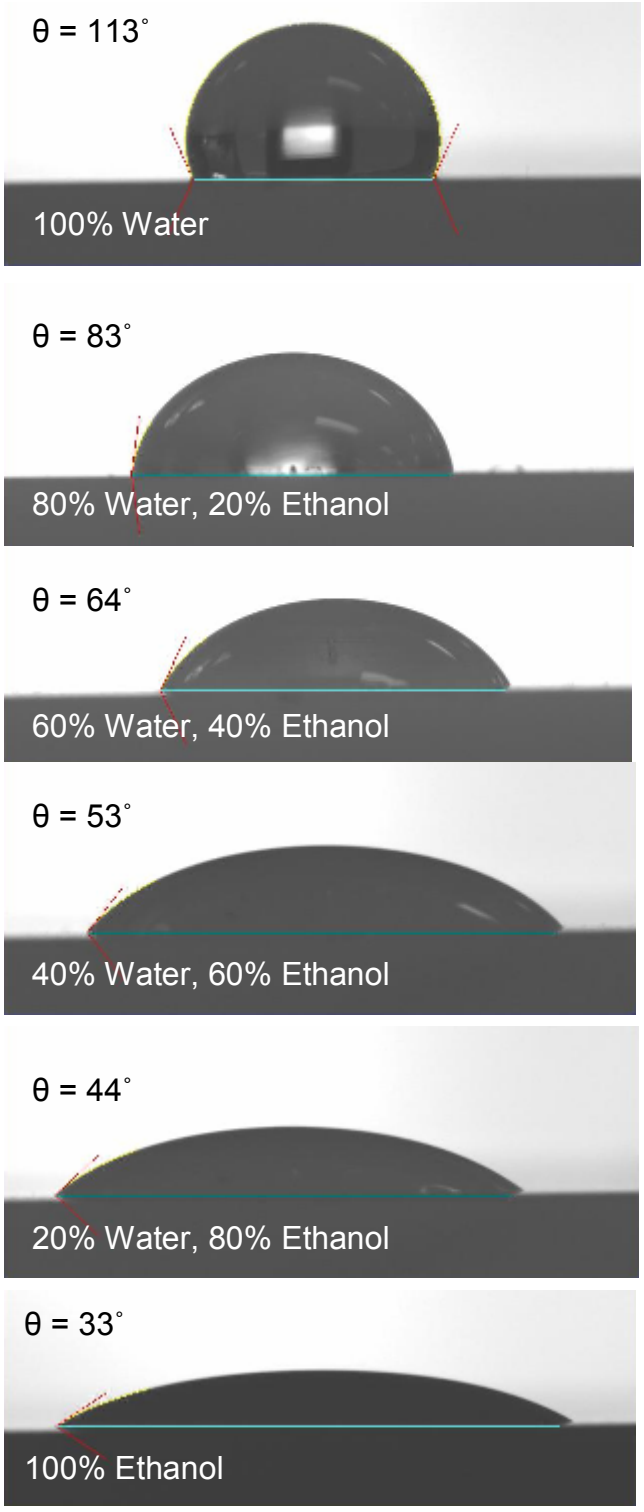

Figure 3.6 Measured Contact Angles between Ethanol-Water Mixtures and PTFE

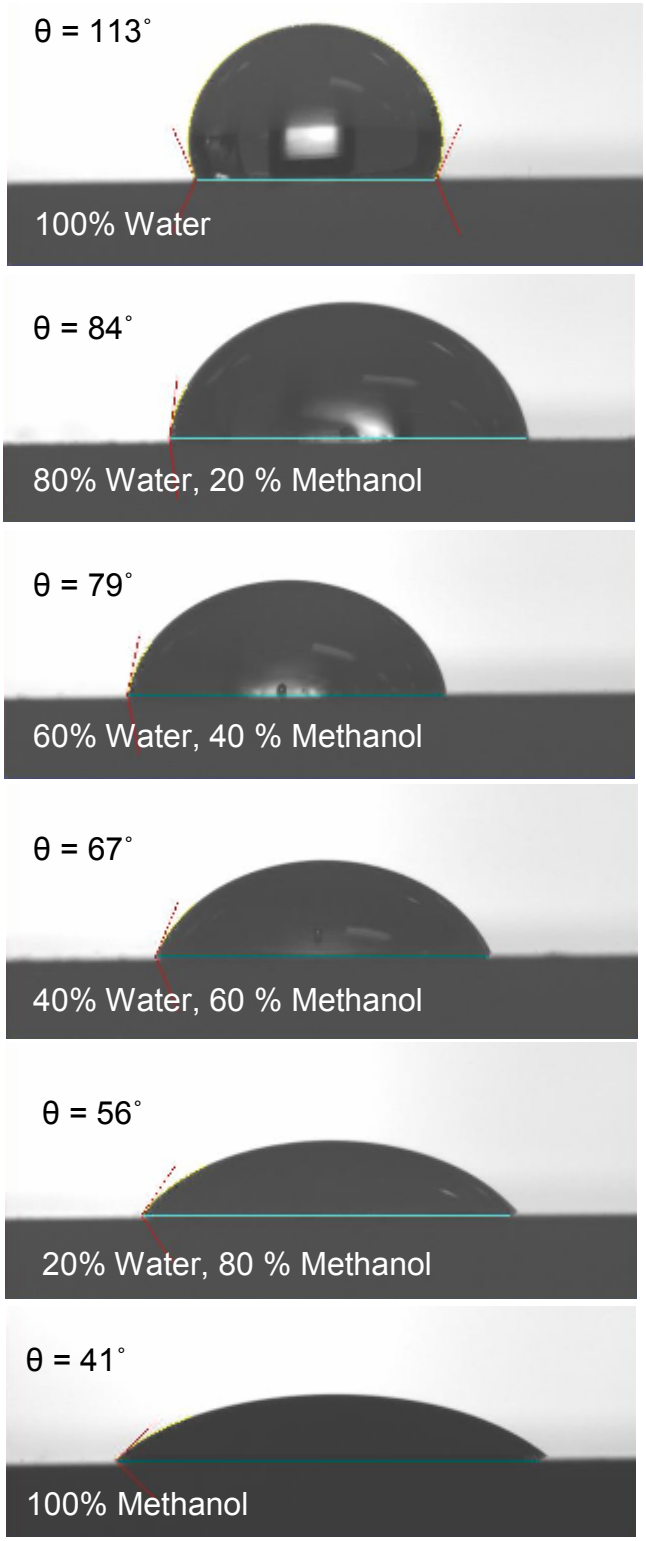

Figure 3.7 Measured Contact Angles between Methanol-Water Mixtures and PTFE

3.2.3 Owens-Wendt Plot and Results

Once the contact angles on the reference solid were measured, the dispersive component of the liquid's surface tension was calculated using Equation 3.6. Next, Equation 3.2 was used to determine the polar component. These values were used to calculate the x and y terms of the Owens-Wendt Equation (3.5), which are plotted in Figure 3.8. The resulting curve was highly linear (r^2 = 0.983) and the corresponding slope and y-intercept were used to calculate the surface energy components of the ceramic wick. Critical surface tension of the solid and surface tension values of the liquids are listed in Table 3.1. In order for any particular liquid to fully wet a solid (i.e. form a 0° contact angle), both surface tension components (σ^D and σ^P) must be lower than the CST of the solid.

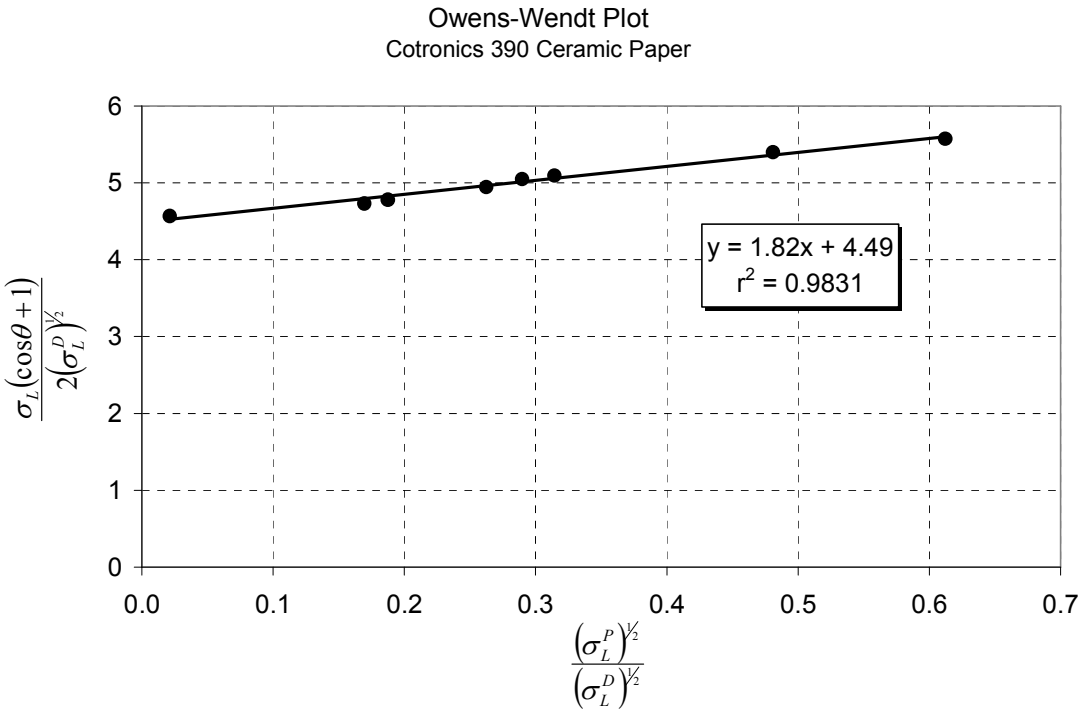

Figure 3.8 Owens-Wendt Plot of Ceramic Wick

Table 3.1 Surface Energy Values for Ceramic Solid and Liquids

		σ_S^D (mN/m)	σ_S^P (mN/m)
Critical Surface Tension of Ceramic Wick		20.1	3.3
	θ_W	σ_L^D (mN/m)	σ_L^P (mN/m)
Water	n/a	26.4	46.4
Methanol	21.4°	21.4	1.0
Ethanol	20.9°	22.3	0.0
FC-72	66.6°	8.0	4.0

Each surface tension component for water was well above the CST of the ceramic wick; thus, water does not wick at all onto this porous solid. For the alcohols, their polar components were below that of the CST, but their dispersive components were slightly above. Consequently, they wick well into the ceramic, but they do not form a 0° angle. Finally, FC-72 exhibits a very low dispersive component, well below the CST, but the polar component was actually greater than the CST. As previously noted, the polar component has greater influence on the overall performance; consequently, FC-72 generated a high contact angle and produced poor wickability.

The question was raised as to whether it is the polar component of the FC-72 that explains its poor wickability or its high density working against the capillary forces that explains the behavior. In order to answer this question, a fluid with similar surface energy characteristics was evaluated. Diisopropyl Ether has an overall surface tension of 17.27 mN/m, dispersive component of 13.25 mN/m, and a polar component of 4.02 mN/m (based on a 38° contact angle on PTFE) [14]. Properties are compared in Table 3.2. However, this ether's density was only 725 kg/m3, similar to that of the alcohols and less than half of FC-72. Wickability of the Diisopropyl Ether was evaluated using the height approach and the results are illustrated in

Figure 3.9. Ether wicked slightly better than FC-72, but it had nowhere near the performance of the alcohols. Both lower density and viscosity may have helped the ether out perform FC-72, but its polar component of surface tension held it from performing as well as its overall surface tension may suggest. Therefore, the polar component of surface energy has a great influence on a fluid's wickability.

Table 3.2 Properties of Working Fluids

Fluid	σ_L (mN/m)	σ^D (mN/m)	σ^P (mN/m)	Density (kg/m3)	Viscosity (cP)
Water	72.8	26.4	46.4	998	0.890
Methanol	22.3	21.4	1.0	787	0.549
Ethanol	22.2	22.3	0.0	785	1.074
FC-72	12.0	8.0	4.0	1680	0.640
Diisopropyl Ether	17.3	13.3	4.0	725	0.379

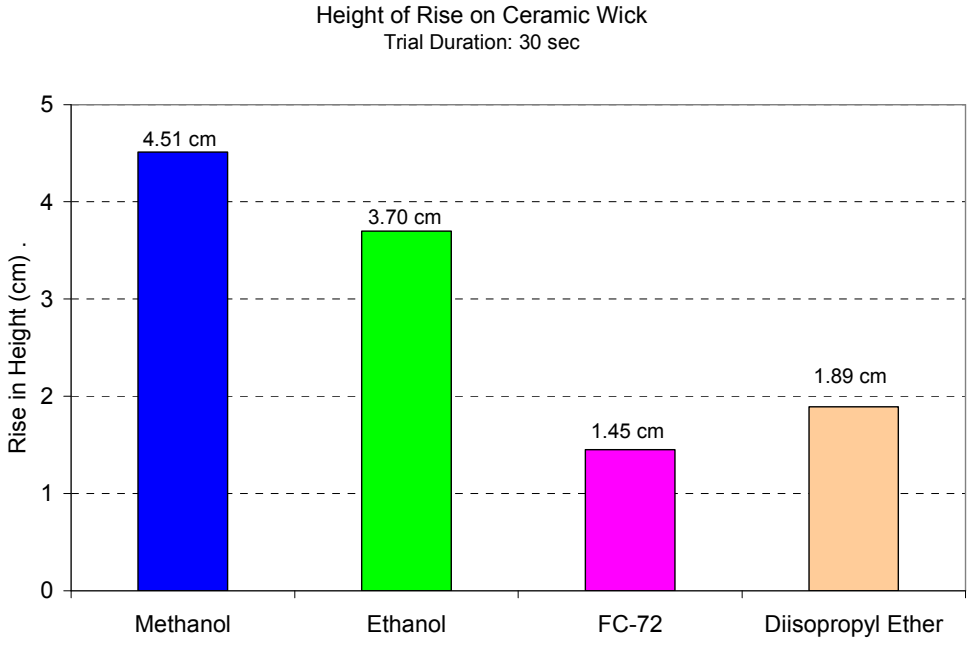

Figure 3.9 Fluid Height of Rise in Ceramic Wick

3.3 Surface Energy Summary

Initially the surface energy of the ceramic wick was modeled using the Zisman Theory, which was determined to be inappropriate for this material. The lesson learned was that for surface energy analysis, one must carefully select the appropriate theory for the particular material of interest. Consequently, the alumina based ceramic fibers were appropriately modeled using the Owens-Wendt Theory. The surface energy components of the liquids were determined empirically with the use of a goniometer by measuring the contact angle on a reference solid. An Owens-Wendt Plot revealed the surface energy of the ceramic wick. Although FC-72 has a relatively low overall surface tension, its poor wickability was due to its high polar component.

Now that the CST of this wicking material has been determined, it may be used when any proposed liquid is suggested in the future. The surface tension of any proposed liquid must simply be broken down into the polar and dispersive components and compared to the CST of the solid. This comparison will predict the wickability of the proposed liquid onto these alumina fibers.

CHAPTER 4

TRANSIENT COOLING CAPACITY

For systems requiring a transient cooling scheme such as expendable weapons, the transient cooling capacity of wick-based coldplates was investigated. As previously mentioned, preliminary cooling capacity evaluations had been performed at Raytheon Space and Airborne Systems on a wick-based coldplate [1]. The purpose of this study was to compare the performance of a wick-based coldplate to that of a phase-change-material (PCM) coldplate currently used to cool high heat flux circuit card assemblies (CCA) found in military electronics. These PCM coldplates serve as heat sinks for CCAs used in expendable weapons as shown in Figures 4.1-2. PCM coldplates typically consist of a metal matrix, usually porous foam, and solid phase change material, usually a paraffin wax. Two coldplates, one metal matrix and one wick-based, were built to the same dimension and footprint, see Figure 4.3. These coldplates were placed in the horizontal position and subjected to a 100 Watt heat load; the temperature of the baseplate was recorded over time, see Figure 4.4.

Figure 4.1 Example of an Expendable Weapon System

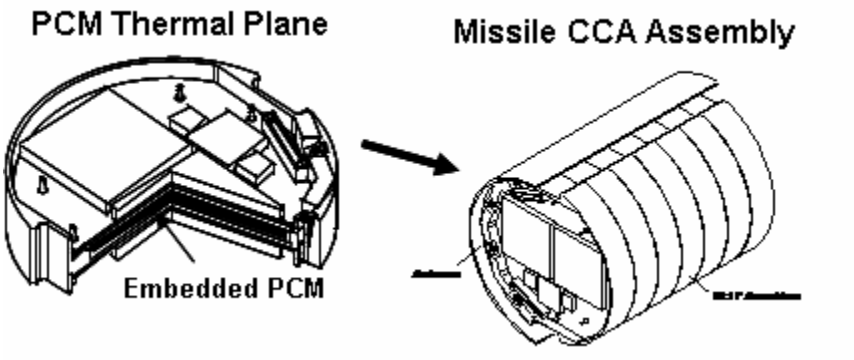

Figure 4.2 Example of CCA Cooled by a PCM Coldplate

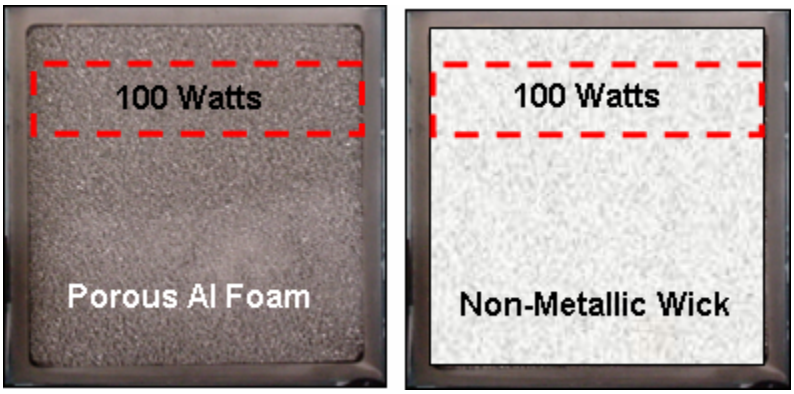

(a) (b)

Figure 4.3 (a) PCM Coldplate (b) Wick-based Coldplate

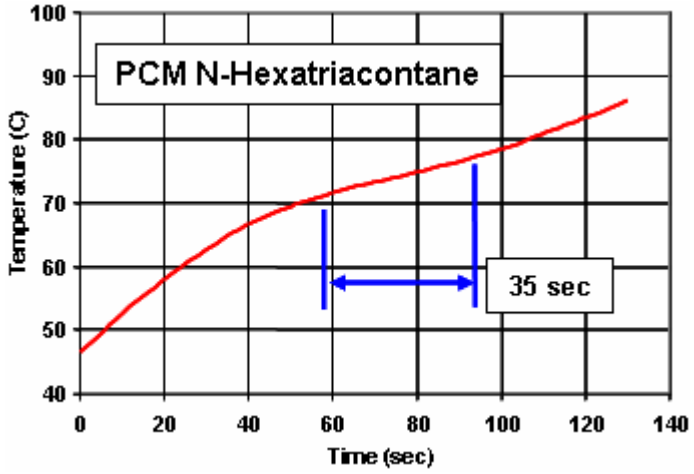

(a)

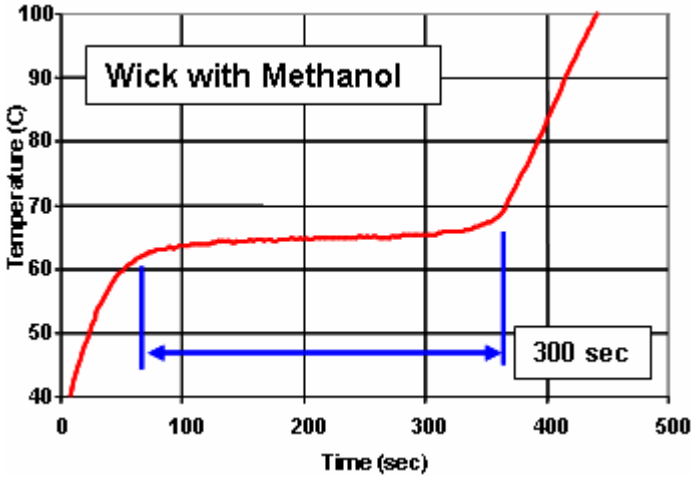

(b)

Figure 4.4 Baseplate Temperature Profile of (a) PCM Coldplate and (b) Wick-based Coldplate

The baseplate temperature of the PCM coldplate continuously increased with time, suggesting sensible heating was dominant. Only a small portion of the curve, between inflection points, displayed latent heating. Furthermore, only 29.5% of the available phase change material was consumed during the test. This configuration requires the heat to be transported from the source to the phase change material through the porous aluminum foam. The wick-based coldplate was composed of a cotton wick and methanol as the working fluid.

Initially, the baseplate temperature increased due to sensible heating. Once the saturation temperature of the liquid was reached the baseplate temperature remained fairly constant for an extended period of time (300 seconds). Cooling capacity was defined as the product of the duration of latent heating and the input power, consequently the cooling capacity was 30.0 kW-secs. Finally, as the liquid supply ran out the baseplate temperature resumed its clime; 85.7% of the available liquid was consumed. The latent heating portion of the curve for the wick-based coldplate was an order of magnitude greater than that of the PCM coldplate. Liquid within the wick-based coldplate was transported to the heat source via capillary pumping, apparently a much more efficient process.

As stated earlier, one of the goals of this research was to improve upon the preliminary work performed at Raytheon. First, the cotton wick was replaced by an alumina based porous ceramic. Second, the use of binary mixtures of alcohols and water were explored to determine their impact on cooling capacity.

4.1 Transient Test Setup

The goal for the test setup for the transient cooling capacity tests was to replicate what was done at Raytheon in order to have a direct comparison. Figures 4.5-7 display the test hardware for the open system. Essentially, the wicking material was sandwiched between a Lexan cover and an aluminum baseplate, and completely filled the cavity. It was considered an open system because it was not sealed; in fact, it had two port holes, which allowed generated vapor to escape. A flexible strip heater was used as the heat source and a thermocouple (T-type, 36 gage) was placed in the same location as the original study, see Figure 4.7. Temperatures were recorded using a Fluke Hydra Data Logger. The resolution of the data logger was 0.001°C and the error reported on the spool of thermocouple wire was ±1.0°C. Thus, the design stage error associated with this instrument was ±1.0°C.

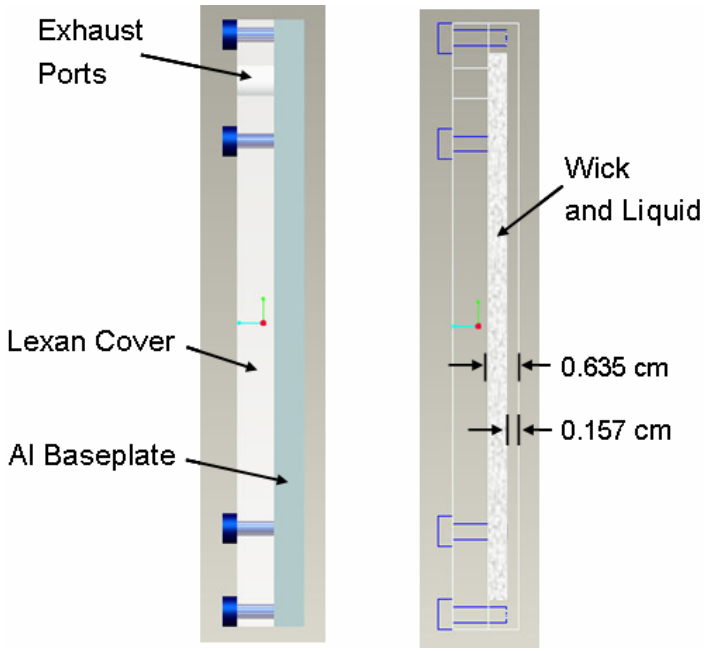

Figure 4.5 Side View of Transient Cooling Capacity Test (Open System)

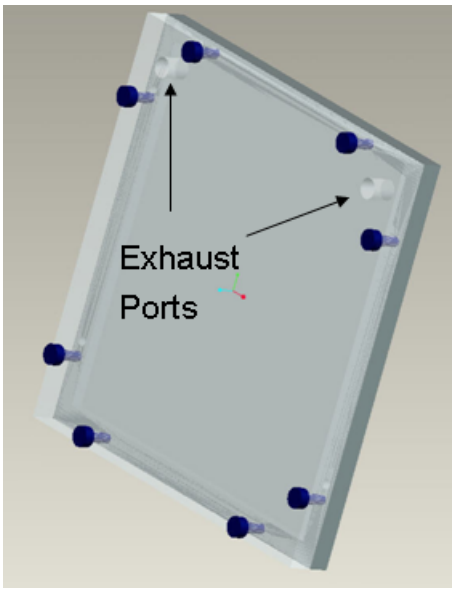

Figure 4.6 Isometric View of Transient Cooling Capacity Test (Open System)

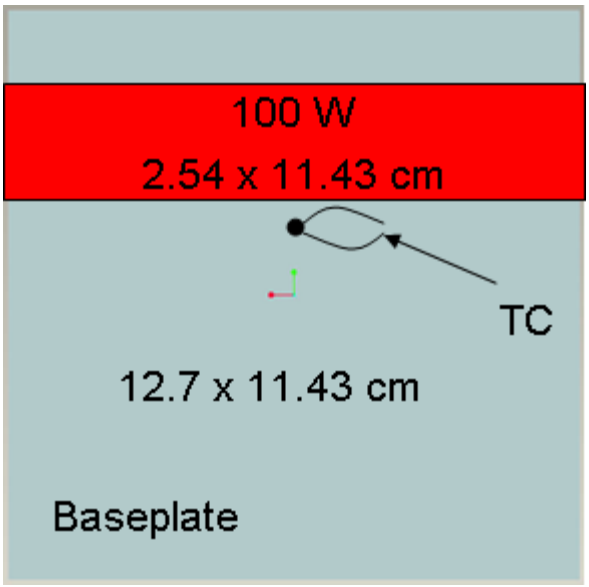

Figure 4.7 Back View of Transient Cooling Capacity Test (Open System)

4.1.1 Transient Test Procedure

For each of the transient cooling capacity tests, the wicking material was completely filled with the working fluid. Next, the coldplate was placed in either the horizontal or vertical position. When placed in the vertical position, the heat source was on top as illustrated in Figure 4.7. Next, the power supply was manually adjusted to supply enough current to the strip heater so that it would dissipate 100 Watts. Baseplate temperatures were recorded every five seconds. Generated vapor was allowed to exit the system via two exhaust ports. The system was powered off once fresh liquid was no longer available to the heated region, which was indicated by a sharp increase in baseplate temperature. Wicking material was replaced after individual evaluations, and each configuration was tested in duplicate. To prevent inhalation of exhaust vapors, tests were performed under a hood vent.

4.2 Transient Test Results for Cotton Wick

In an effort to duplicate the results obtained during the Raytheon study, the wick-based coldplate was initially tested in the horizontal position, using a cotton wick, and methanol as the working fluid. The resulting temperature profile is illustrated in Figure 4.8. It was necessary to establish a systematic method for determining the portion of the curve that represented latent heating. Initially, the temperature rose quickly while the system was heated sensibly. The beginning of the latent portion was indicated once the curve angle dipped below three degrees from horizontal. Similarly, the end of the latent heating portion of the curve was established once the curve angle grew to greater than three degrees from the horizontal. In this particular case, the duration of the latent heating was 320 seconds, resulting in a cooling capacity of 32 kWatt-sec. This was in good agreement to the cooling capacity obtained in the Raytheon study.

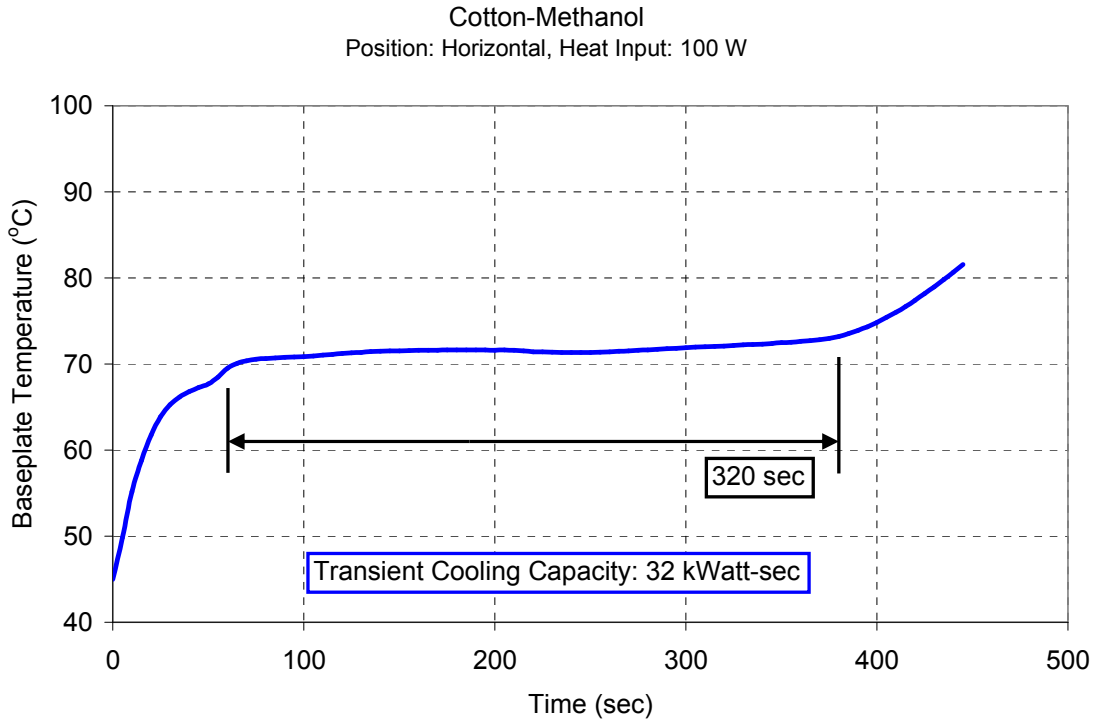

Figure 4.8 Transient Temperature Profile of Cotton Wick with Methanol (Horizontal Position)

Once it was verified that the test set and procedure produced similar results to the original study, new test parameters were introduced. First, the cotton wick was saturated with ethanol and the coldplate remained in the horizontal position. The resulting cooling capacity for this configuration was 24 kWatt-sec, as shown in Figure 4.9. Also, note that baseplate temperatures were higher than those with methanol due to ethanol's higher saturation temperature. This performance was 25% less than the configuration containing methanol and was attributed to ethanol's inferior wickability (18% less than methanol) and latent heat of vaporization (22% less than methanol).

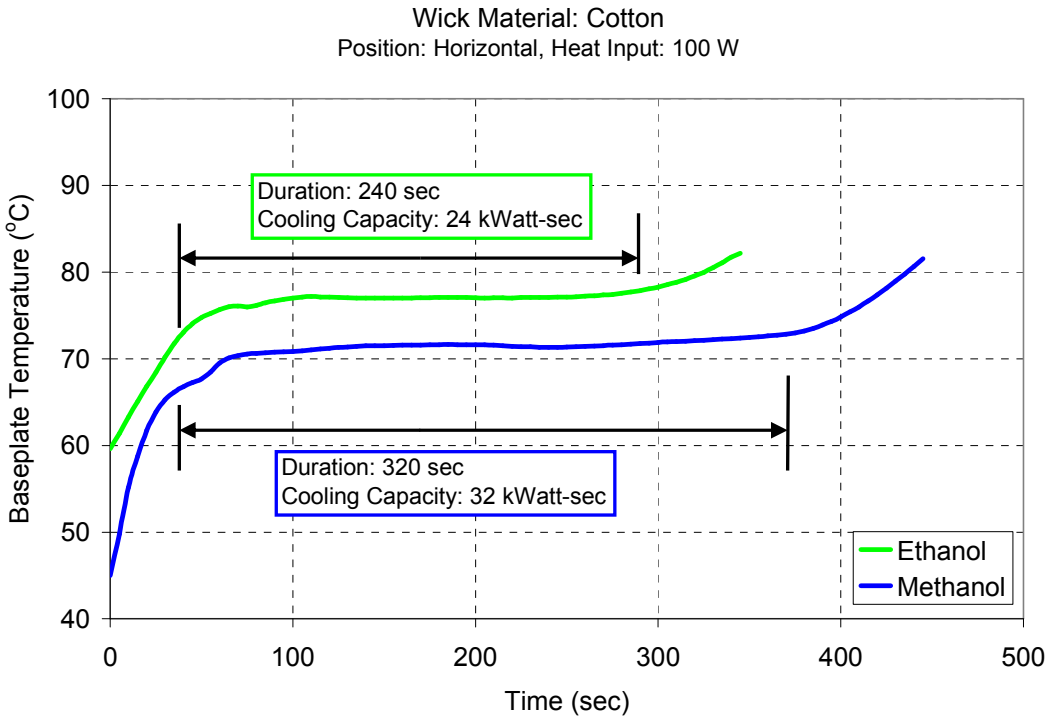

Figure 4.9 Transient Temperature Profile – Methanol vs. Ethanol

Next, the coldplate was placed in the vertical position and evaluated with a cotton wick and methanol. The transient temperature profile was illustrated in Figure 4.10. Cooling capacity for this configuration was diminished by almost 38% compared to the horizontal

configuration. In the vertical position, capillary pumping within the wick had to fight against the force of gravity. This allowed to for less of the working fluid to be available at the heat source.

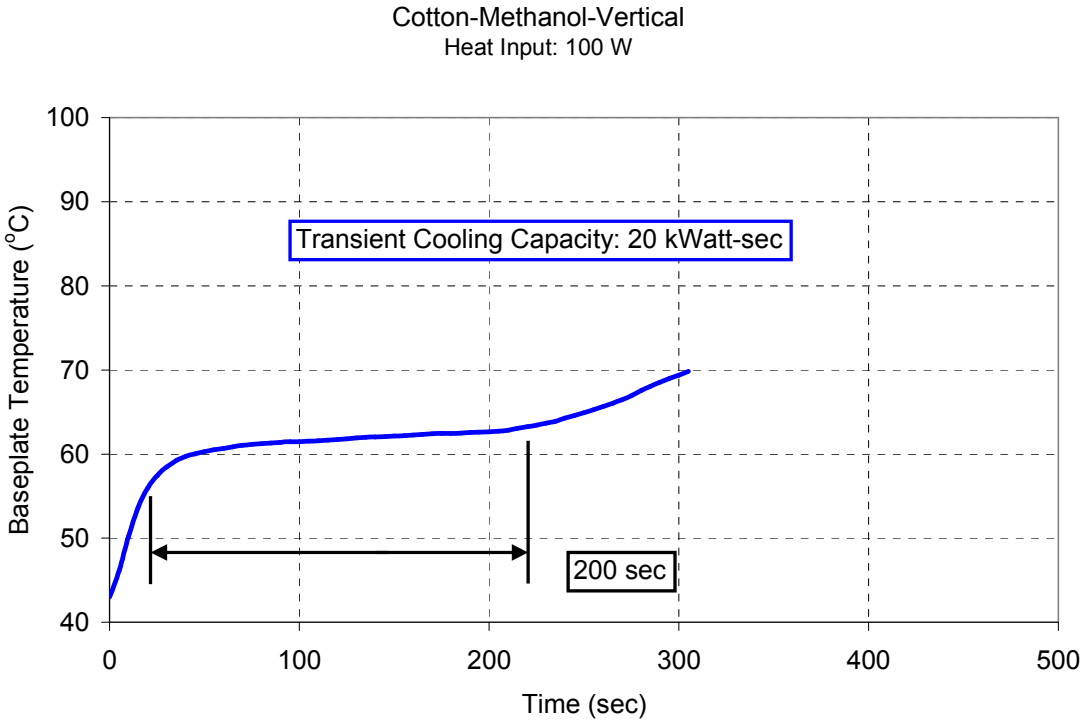

Figure 4.10 Transient Temperature Profile – Cotton, Methanol, Vertical

Next, the cotton wick was saturated with a binary mixture of 40% Methanol and 60% water (fraction was determined by mass). With the coldplate in the vertical position the resulting temperature profile was generated and is displayed in Figure 4.11. Cooling capacity for this case was enormous, 250% greater than pure methanol. Wickability of the binary mixture was not as good as that of pure methanol, however the added heat capacity of the water more than made up for the difference. This demonstrates the huge potential of alcohol-water mixtures as working fluids for wick-based coldplates. The alcohol contributes in terms of wickability, and the

water adds heat capacity. Another effect of the water was that the saturation temperature and consequently baseplate temperatures were greater than for the pure methanol case.

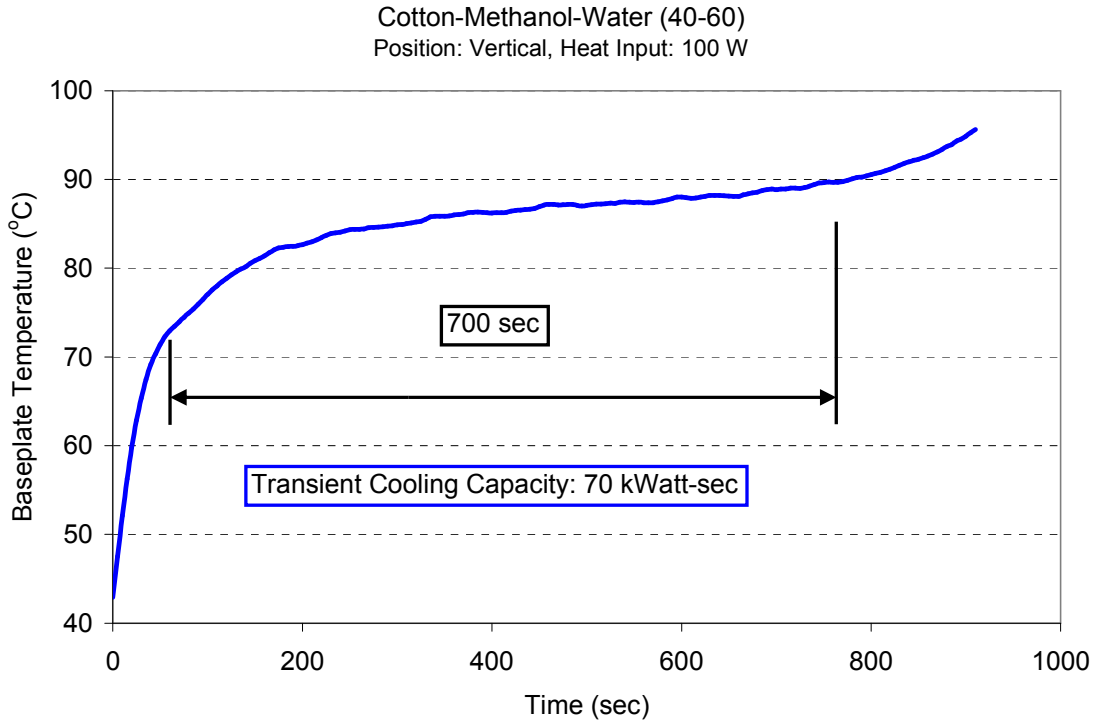

Figure 4.11 Transient Temperature Profile – Cotton, Methanol-Water (40-60), Vertical

4.3 Transient Test Results for Ceramic Wick

Since cotton is not a viable material for military applications, it was replaced with an alumina based porous ceramic, Cotronics Ultra-Temp Ceramic Paper 390. This ceramic wick is a very robust material that can withstand over 1300°C. Its low density gives it a large weight advantage over porous aluminum foams. However, this product is typically used as an insulator on furnace walls, thus its thermal conductivity is very poor, 0.055 W/m-K. Fortunately, wick-based coldplates do not rely on thermal conductivity through the porous matrix, preferring to

take advantage of the capillary action of the porous solid to transport the liquid to the point of need.

Both pure methanol and ethanol were evaluated with this ceramic wicking material in the vertical position, and a comparison of the transient temperature profiles is displayed in Figure 4.12. Once again, methanol out performs ethanol, this time by a 28% margin. This was a larger margin than in the horizontal case, which was attributed to the greater importance of wickability for the vertical configuration. Figure 4.13 provides a cooling capacity comparison for the data collected thus far. For both the horizontal and vertical configurations methanol outperformed ethanol. Comparing horizontal versus vertical cases using a cotton wick and methanol, it was evident that there was a significant loss in performance by having the coldplate in the vertical position. This loss in performance was recovered and then some by replacing the cotton with a ceramic wick.

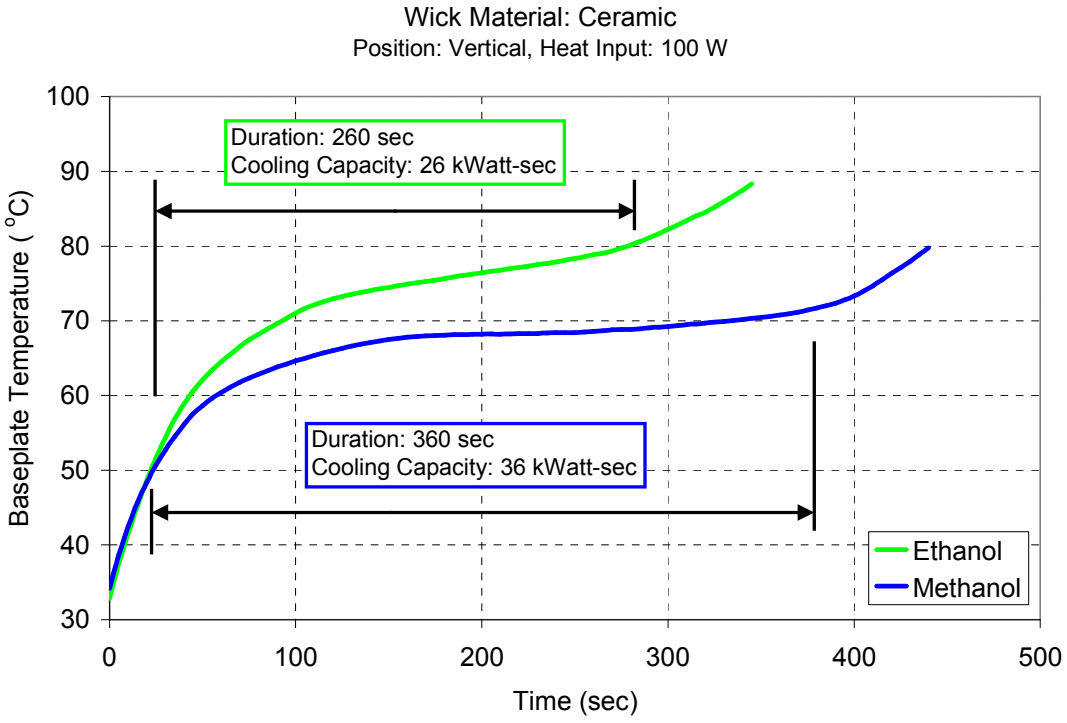

Figure 4.12 Transient Temperature Profile – Ceramic, Methanol vs. Ethanol, Vertical

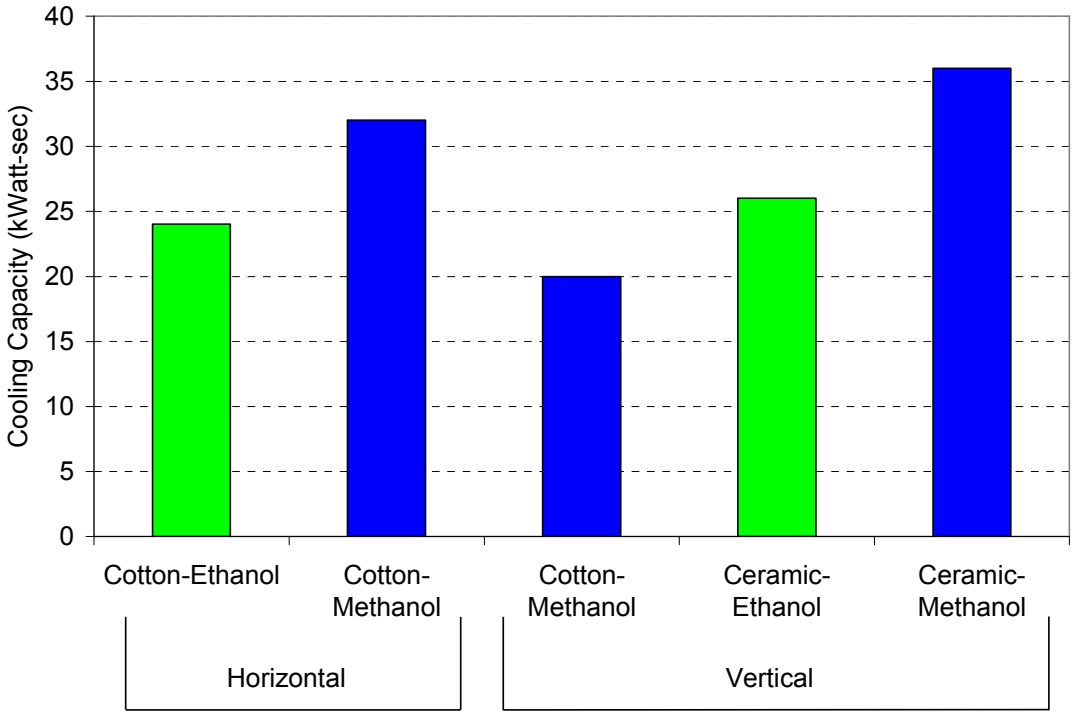

Figure 4.13 Cooling Capacity Comparison between Cotton and Ceramic Wicks

Next, binary mixtures of both methanol-water and ethanol-water were evaluated with the ceramic wick in the vertical position. Figure 4.14 displays the transient temperature profiles for methanol-water mixtures from 30 to 100% concentration. Recall that methanol concentrations below 30% did not wick into the ceramic, thus these concentrations were not considered. In the pure methanol case, baseplate temperature was held relatively constant until all the available fluid was evaporated, causing the temperature to raise sharply. As water was introduced into the mixture, the baseplate temperature varied linearly with time. This was due to the latent heating of the liquid having higher volatility, methanol, and the sensible heating of the liquid having lower volatility, water. Furthermore, the overall cooling capacity increased with higher concentrations of water, but at the price of hotter baseplate temperatures. Similar plots were generated for ethanol-water mixtures, and a summary of all cooling capacities was plotted

and shown in Figure 4.15. Individual temperature profiles for all configurations are displayed in Appendix B. At the lower concentration levels, the performance between methanol-water and ethanol-water was comparable. At low alcohol concentrations, ethanol-water had the advantage of superior wickability. However, at alcohol concentrations of greater than 60%, the wickability of methanol-water surpasses that of ethanol-water. This, in combination with methanol's superior heat of vaporization, makes it the clear choice at higher concentration levels. Generally speaking, the cooling capacity dramatically increased with increased water content. These cooling capacities were at least an order of magnitude greater than that of the currently used metal-matrix coldplates saturated with a solid phase-change-material [1].

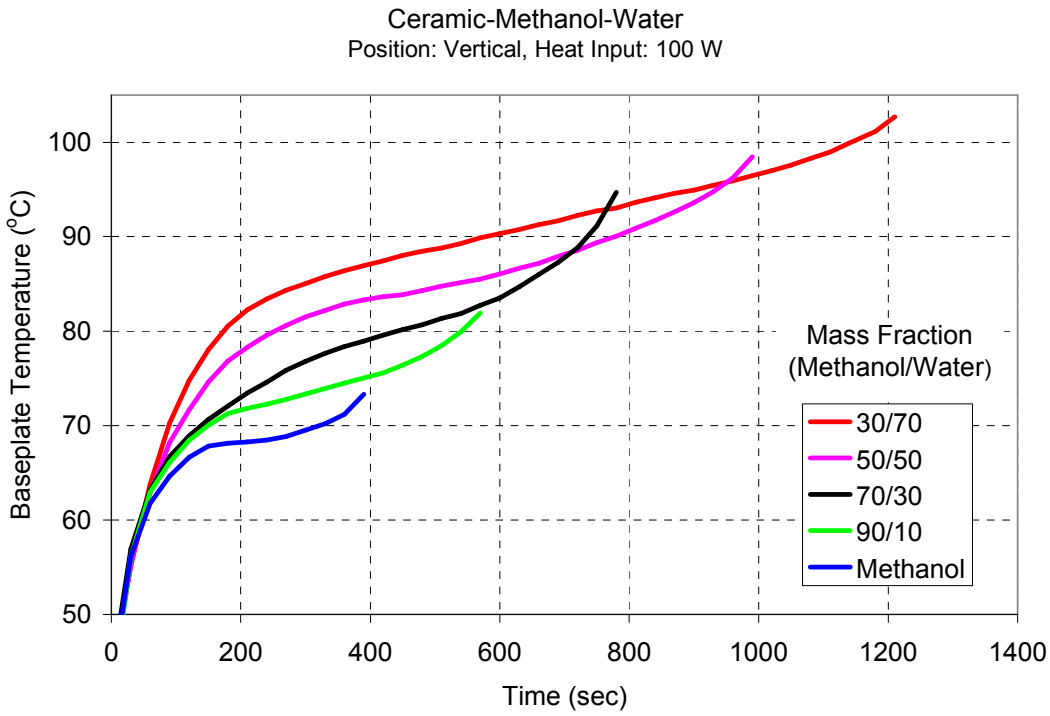

Figure 4.14 Transient Temperature Profile – Ceramic, Methanol-Water Mixtures

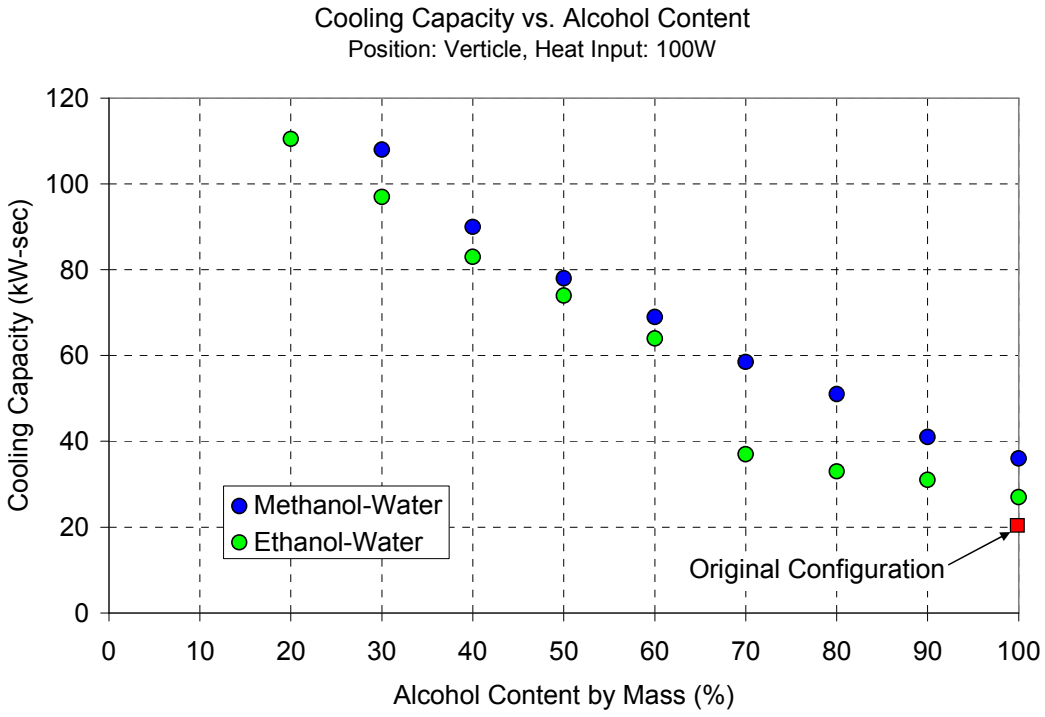

Figure 4.15 Transient Cooling Capacity Comparisons for Alcohol-Water Mixtures

4.4 Transient Cooling Capacity Summary

Transient cooling capacity tests were performed on an open wick-based coldplate and a variety of configurations were evaluated. Parameters varied were wick material (cotton vs. ceramic fibers), coldplate position (horizontal vs. vertical), and working fluid (methanol-water mixtures vs. ethanol-water mixtures. For all test configurations, no nucleate boiling was observed. Since the wicking material encompassed the entire cavity between the baseplate and the clear cover, there was no space available for bubble growth. This indicates that the dominant phase change mechanism was evaporation. By replacing the cotton with a ceramic wick, the cooling capacity improved by 80%. Furthermore, the use of binary mixtures enhanced the transient cooling capacity by an order of magnitude. This enhanced cooling capacity has plenty of margin for current and future military electronics.

CHAPTER 5

STEADY STATE TEST SETUP

Thermal evaluations in the previous chapter demonstrated tremendous potential in the use of binary mixtures in terms of transient cooling capacity. This is useful for systems only requiring a transient cooling scheme, however most military and aerospace electronics operate continuously. This requires a wick-based coldplate that either is continuously supplied with fresh liquid or can recycle the working fluid in order to operate on a continual basis. Figures 5.1-2 illustrate a typical military electronics box. These electronics boxes are placed in many platforms such as tanks, helicopters, fighter planes, and ships, which are designed to operate in harsh environmental conditions. In these environments, the external air often contains corrosive agents such as moister, salt, oil, dirt, sand, etc. For this reason, most military electronics are not directly air cooled. Instead the exterior of the electronics box is air cooled, while the electronics are sealed inside.

The chassis of the electronics box is slotted to allow the placement of various electronics modules. Typically, each module consists of two circuit cards attached to a thermal core between them. This thermal core is simply a relatively thick plate often made of aluminum, copper, or an expensive alloy and is used to conduct the heat from the boards to the chassis. Material selection for the thermal core depends greatly on the level of heat dissipated by the electronics. Heat dissipated by individual integrated circuits (ICs) must conduct through the circuit card, along the thermal core, and through the chassis before it is removed by the external cooling air. Thus, such circuit cards are considered conduction cooled boards.

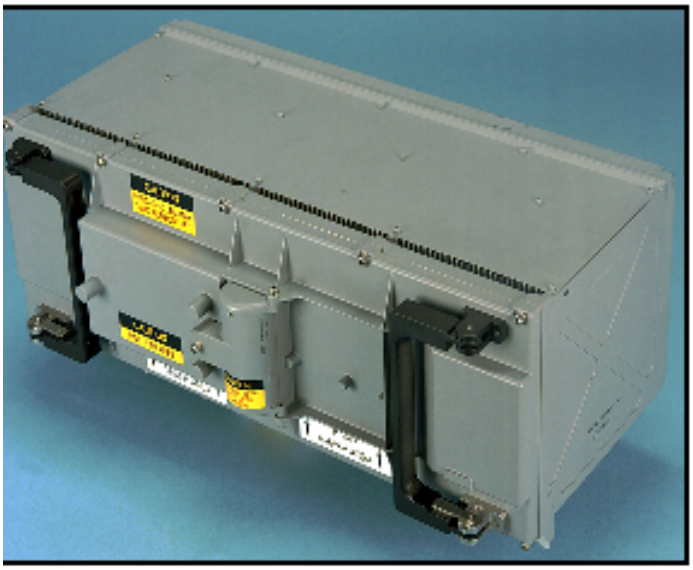

Figure 5.1 Typical Military Electronics Box

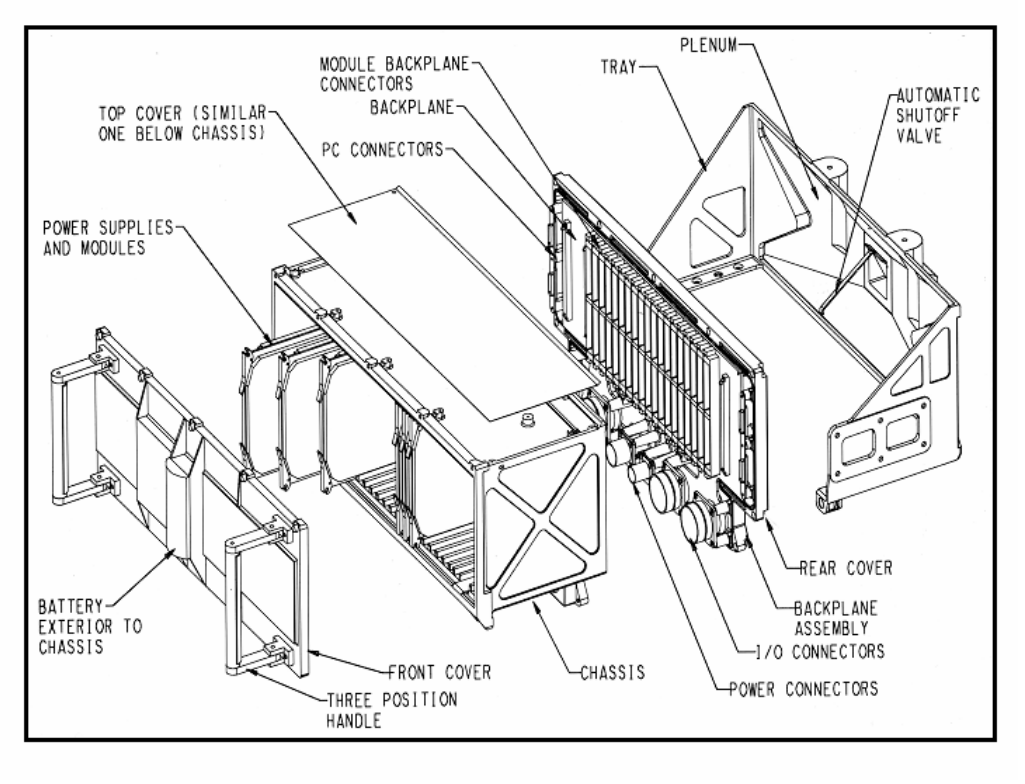

Figure 5.2 Exploded View of Military Electronics Box

With the heat dissipation of electronics increasing at a rapid pace, the use of these solid, high conductivity thermal cores will become obsolete in the near future for cutting edge, high heat-flux electronics. The thermal resistance of these solid cores is fixed; consequently, the temperature rise across them is linearly proportional to the heat dissipation. At some point, these modules will have to contain a two-phase cooling scheme in order to keep up with the power demands. The final objective of this work was to design a sealed, wick-based coldplate and empirically determine its steady state thermal resistance with the goal of producing values superior to that of a solid core.

5.1 Coldplate Sealing

As has been documented thoroughly, for two-phase systems, great care must be taken to ensure that the system is sealed properly [20, 21]. Without proper sealing, the vapor generated by the heating of the working fluid may escape or the working fluid may obtain non-condensable gases. Such foreign gases tend to degrade boiling heat transfer. Moreover, these non-condensable gases degrade the thermal performance because they tend to accumulate at the condenser section. Once this occurs, the accumulated non-condensable gases serve as a barrier for fresh vapor trying to reach the condenser section.

5.1.1 O-ring Seal

A sealed wick-based coldplate consisting of a baseplate and cover was designed and fabricated, see Figure 5.3. These two plates were to be held together by a series of screws along the perimeter, see Figures 5.4-5. Screw holes were drilled and tapped to match a 6-32 thread, flat undercut screw, see Figure 5.6. This type of screw was selected so that the screw head would lay flush with the outer plane of the cover. A gland was machined into the baseplate for the placement of an O-ring to create a face seal. Gland dimensions (depth, width, and radius) were taken from the Parker O-Ring Handbook [22] and had to be held within a tolerance of ±0.003 inch. Note that special care had to be given to the design of the radii of the groove at the four corners of the coldplate. Initially, the inner and outer radii were both set to

0.125 inch, which resulted in an inconsistent groove width along the curvature at each corner, see Figure 5.7.

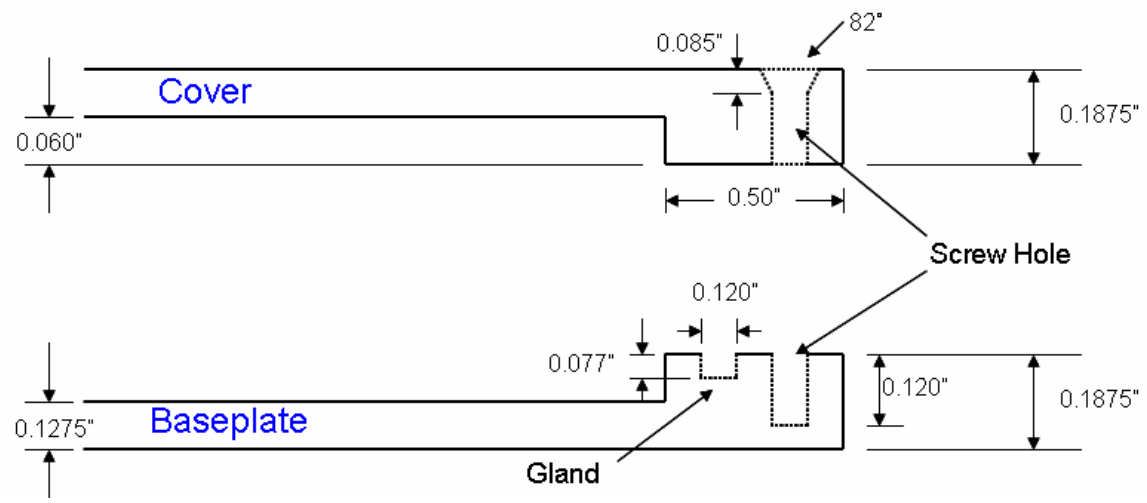

Figure 5.3 Side View of Sealed Wick-based Coldplate Design

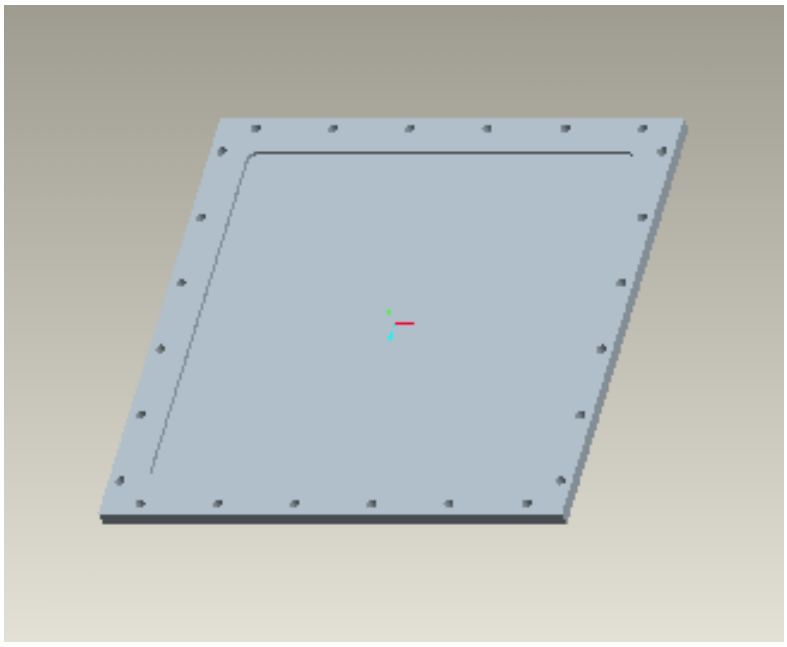

Figure 5.4 Isometric View of Top Cover

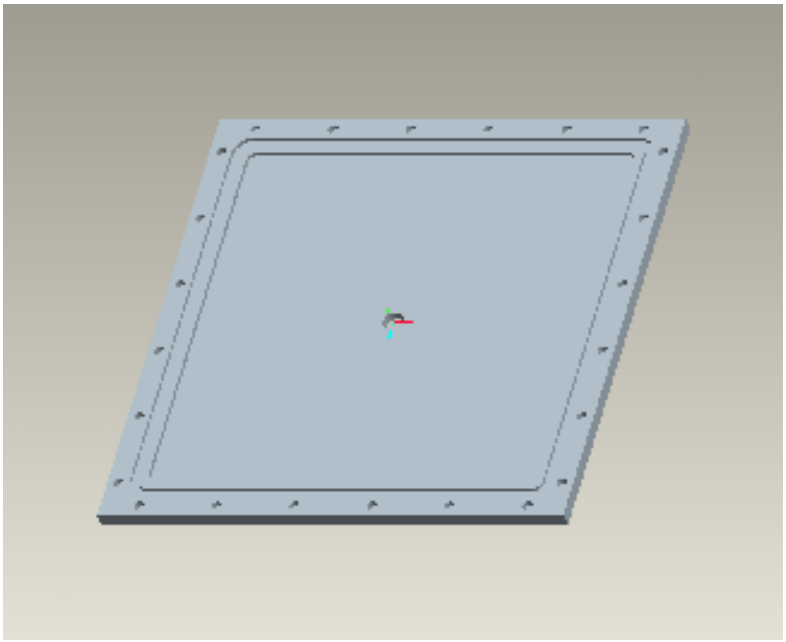

Figure 5.5 Isometric View of Baseplate

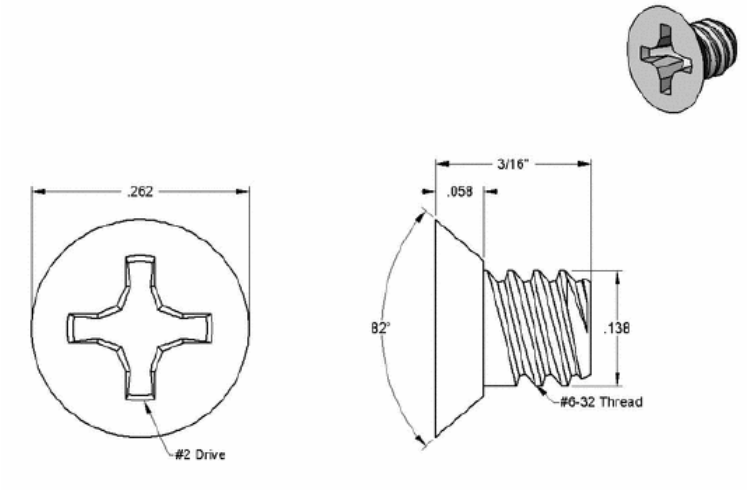

Figure 5.6 Flat Undercut Screw

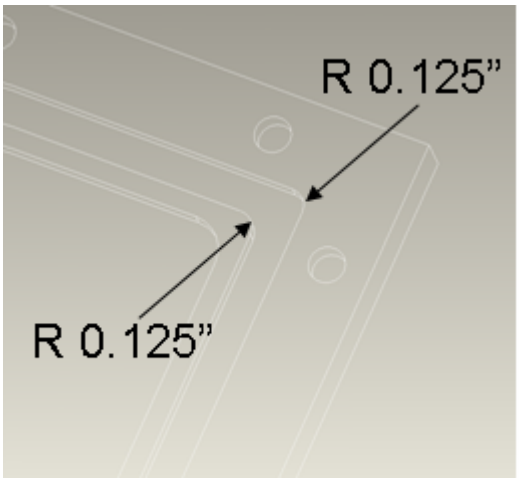

(a)

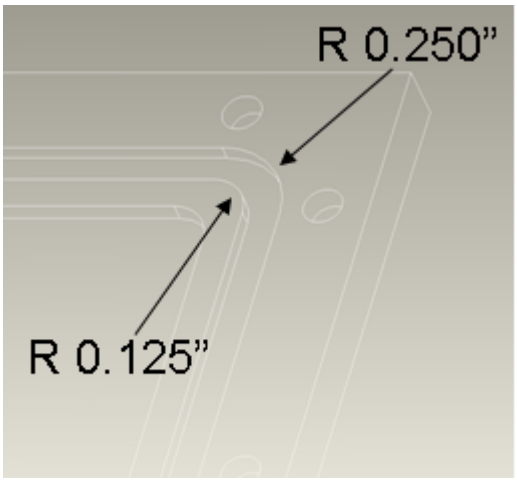

(b)

Figure 5.7 Groove Radii (a) Inconsistent and (b) Consistent Width

This inconsistent groove width resulted in poor sealing. Next, the outer radius of the groove was varied until the groove width was constant along the entire curve. Finally, a No. 2-165 Parker O-ring made of EPDM was used to create the static seal. Again, the material selection was driven by its compatibility with methanol.

The overall goal of this coldplate design was to have a sealed system that could be readily taken apart. This would allow access to the cavity of the coldplate in order to vary the

wick configurations. This is contrary to typical two-phase systems such as heat pipes, which are permanently sealed by weld or solder. This creates a superior seal, but doesn't provide the flexibility of varying the contents of the system.

5.1.2 Fitting Seal

It was necessary to attach a valve in the coldplate in order to insert the working fluid. Furthermore, both temperature and pressure sensors were required to monitor the thermodynamic state inside the cavity. Four holes were placed on the top cover, See Figure 5.8, to accommodate one valve, one pressure transducer (PT) and two thermocouples (TC). Originally, the valve and pressure transducer access holes were tapped in order to fit those two items directly onto the top cover. However, that portion of the top cover was too thin, which did not allow for enough threading. Consequently, threaded couplings were tungsten inert gas (TIG) welded onto the access holes, see Figure 5.9. Once the threaded couplings were in place, threaded adapters were used to fit the valve and pressure transducer onto the top cover.

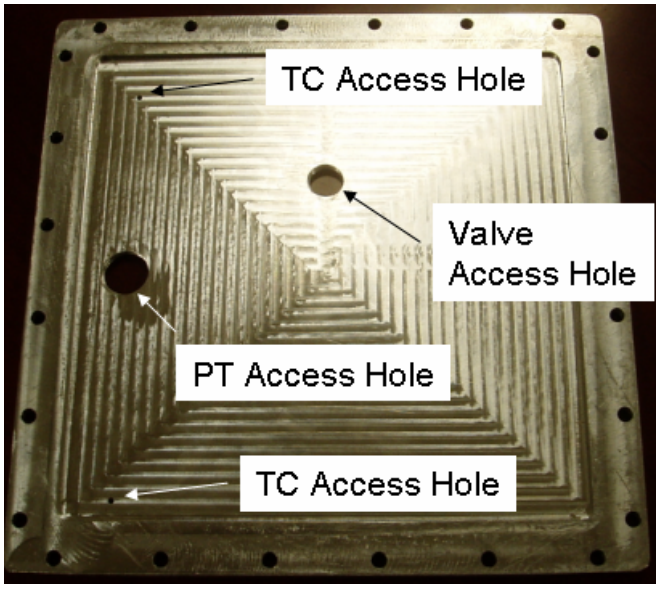

Figure 5.8 Access Holes on Top Cover

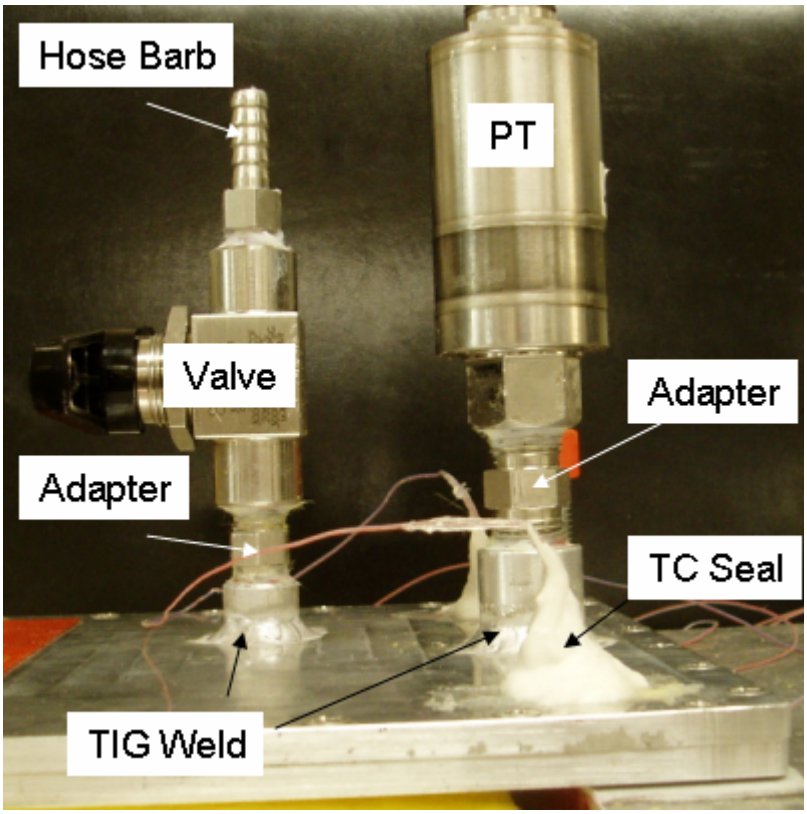

Figure 5.9 Valve and Pressure Transducer Fittings

5.1.2.1 Sealant Compatibility Test

Once the hardware was in place, a sealant was required to seal the many thread fittings. Said sealant had to seal under high vacuum and be compatible with methanol. Many sealant vendors were contacted in order to obtain a material that met these requirements. Unfortunately, none of the vendors that were contacted would guarantee that their sealants would not react with methanol. Consequently, 3M's Compatibility Test Procedure [23] was used to test various sealants with methanol. Figure 5.10 displays the compatibility test setup, which includes a hot plate, boiling flask, Soxhlet Extractor, and condenser. Sealant test samples were weighed initially and placed in the extractor chamber. Test fluid, methanol, was placed in the boiling flask and heated. Generated vapor travels up the large side tube and into the chilled

water condenser where it is condensed and drips into the Soxhlet Extractor, which contains the sealant sample. Once the fluid level in the extractor reaches the top of the small return tube, it drains back into the boiling flask. Once draining begins, a siphon is established and the extractor is drained completely. Any extracted material form the test sample is collected in the boiling flask. Note that roughened copper pieces were placed in the boiling flask to avoid flash boiling. Tests were performed in duplicate.

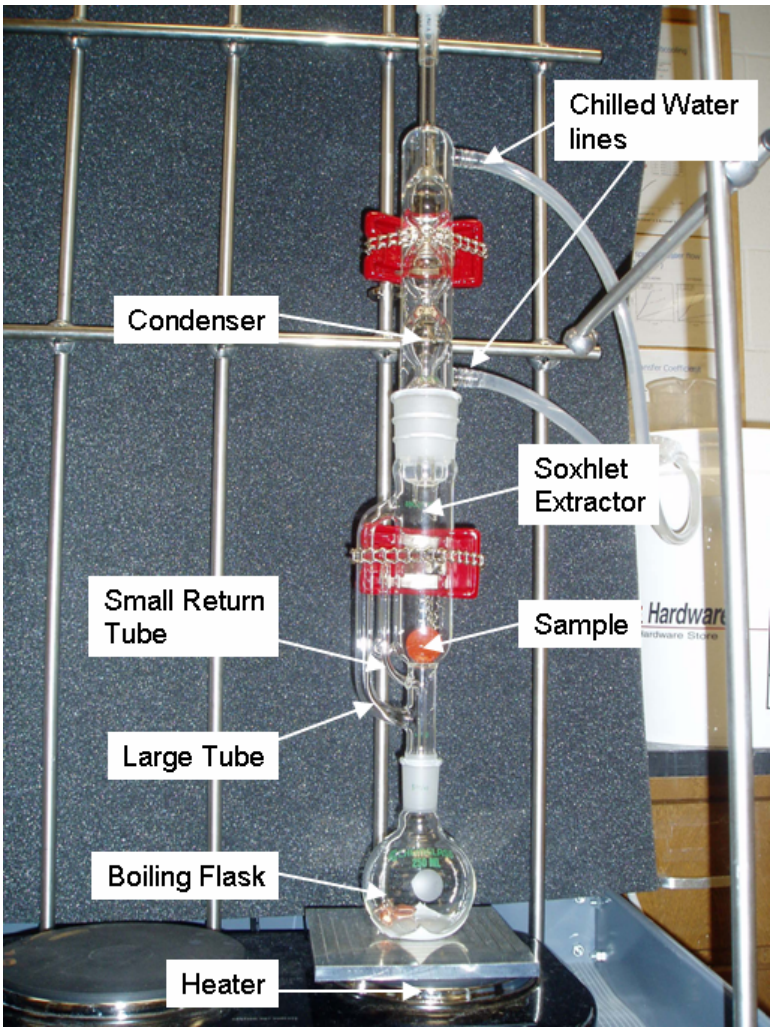

Figure 5.10 Compatibility Test Setup

This process repeats continuously with the intent of keeping fresh fluid in contact with the sample at all times. Test duration of three days was recommended, but due to lab regulations, the hot plate was turned off at nights when the test was left unattended. Initially, several sealants had been discarded because of their immediate reaction to methanol. However, three sealants, Seal-All, 3M Epoxy 1838-L, and Room Temperature Vulcanizing (RTV) Silicon, did not noticeably react with methanol, thus they were subjected to this compatibility test. Before and after pictures are displayed in Figures 5.11-13 and weights are listed in Table 5.1.

Seal-All's manufacturer claims that it is resistant to gasoline, paint thinner, and most solvents. Before this material was exposed to methanol, it was soft and transparent. After exposure it was hard and opaque, clearly indicating that it reacted with methanol. Surprisingly enough its weight did not change much. For the 3M Epoxy, there was little change visually, but the weight difference was significant, indicating some reaction with methanol. Finally, the RTV silicon did look any different after exposure to methanol and the weight change was also minimal. Thus, the RTV silicon was used to seal all the threaded fittings.

Table 5.1 Before and After Weights of Thread Sealants

Trial	Sealant	Weight Before (g)	Weight After (g)	Percent Change
1	Seal-All	1.576	1.629	3.4%
2	Seal-All	1.588	1.644	3.5%
1	3M Epoxy	4.150	4.592	10.6%
2	3M Epoxy	3.987	4.528	13.6%
1	RTV Silicon	2.843	2.732	3.9%
2	RTV Silicon	3.011	2.915	3.2%

(a) (b)

Figure 5.11 (a) Before and (b) After Images of Seal-All (Not to Scale)

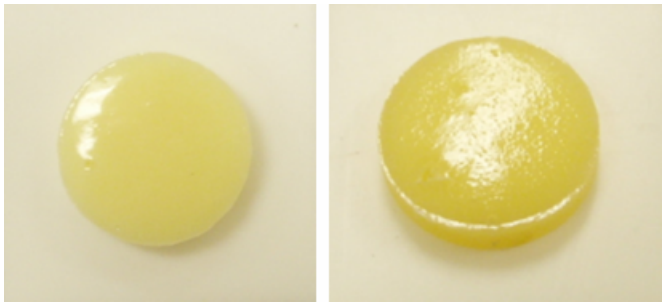

(a) (b)

Figure 5.12 (a) Before and (b) After Images of 3M Epoxy (Not to Scale)

(a) (b)

Figure 5.13 (a) Before and (b) After Images of RTV Silicon (Not to Scale)

5.1.2.2 Thermocouple Seal

Two (T-type, 36 Gage) thermocouples were used to monitor the temperature inside the cavity, see Figures 5.8-9. First, the thermocouples were set in place using regular, clear silicon (DAP), which is easily removed. Next, red RTV silicon was used to seal the access hole. After that, the regular silicon was removed. Then, a white epoxy (Varian Torr Seal®) was poured over the red RTV silicon. This was to give the seal some robustness. Finally, the white epoxy was covered with the clear silicon to provide further protection and strain relief to the thermocouple wire. The only sealant exposed to the cavity (i.e. methanol) was the RTV silicon.

5.2 Degassing System

As discussed previously, working fluids must be void of non-condensable gasses. However, once a liquid is exposed to the ambient, a certain amount of gas will be dissolved into the liquid. Pure water may contain up to three percent of its volume in non-condensable gases [24]. The most common degassing method involves the distilling process. A heat source is typically used to vaporize the liquid, and then the vapor is condensed and collected, while the non-condensable gages are discarded. This was not the approach taken in this study, which had the ultimate goal of producing degassed binary mixtures with known mass fractions. With the available equipment, the traditional approach would have been impractical. Consequently, a degassing system using a vacuum pump was implemented.

5.2.1 Single Fluid Degassing System

A single fluid degassing system was assembled and is illustrated in Figure 5.14. This system consisted mainly of high-vacuum, glass chambers, which were connected by ground glass fittings. Each fitting was lubricated with highly inert Krytox® high vacuum grease. This particular grease was selected because of its compatibility with methanol. Initially, the gassy liquid was poured into Chamber #1, which was then closed using a glass stopper. Next, the entire system below Chamber #1 was evacuated until the pressure dropped below 0.001 pounds per square inch (psi).

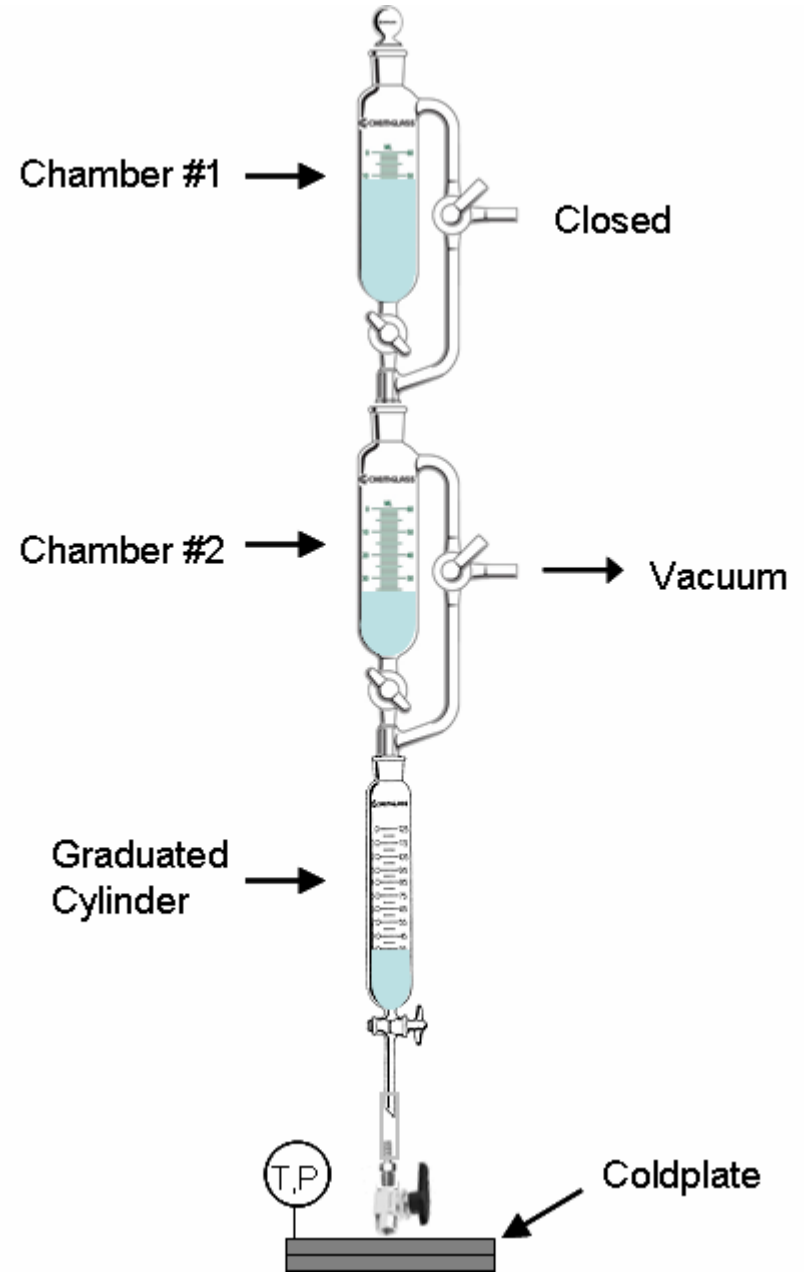

Figure 5.14 Single Fluid Degassing System

Then, the valve below Chamber #2 was closed and a portion the gassy liquid was transferred to Chamber #2. Since Chamber #2 had previously been evacuated, the degassing process began immediately. Next, Chamber #2 was evacuated further (for only ten additional minutes), removing the non-condensable gases and vaporizing some of the working fluid. The decreasing pressure and vaporization of some of the working fluid caused Chamber #2 to get quite cold. Note that pre-evacuating Chamber #2 and then adding the gassy liquid was much more efficient (i.e. minimized vacuum pumping time) than pulling a vacuum directly on gassy liquid starting at ambient pressure. Next, a measured amount degassed liquid was transferred to the smaller, graduated cylinder, which was then emptied into the coldplate. The cylinder had 1 milliliter (mL) graduations. It was important to accurately measure the amount of liquid, which was to be placed into the coldplate in order to know what the fill ratio was. Once the liquid was inserted into the coldplate, its thermodynamic state was compared to reference values to ensure that the liquid was in fact degassed. Figure 5.15 displays the saturation curves for water and methanol [2].

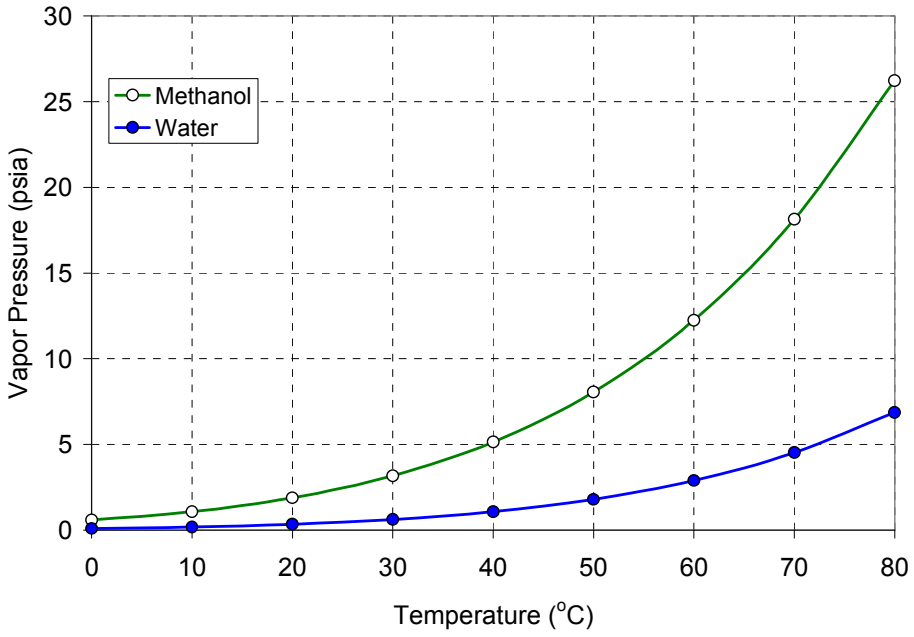

Figure 5.15 Saturation Curves for Water and Methanol

5.2.2 Binary Mixture Degassing System

In order to accommodate for two different liquids, which would be degassed independently and then mixed, two additional chambers were added and interconnected using a three-way valve, see Figure 5.16. This added many more fittings, which had to be properly lubricated in order to maintain adequate sealing. Binary mixtures of water and methanol were degassed by the following procedure.

Gassy water and methanol were poured into Chambers #1 and #3, respectively, and then the rest of the system was evacuated until the target vacuum level was achieved. This typically took between 30 and 45 minutes depending on how well the valve fittings were lubricated. Next, the water was transferred to Chamber #2 and degassed. Then, depending on the desired mass fraction, a specified amount was let into the graduated cylinder through one side of the three-way valve. Note that the original O-rings included with this three-way valve were made out of Viton®, but were replaced with EPDM O-rings. Next, the methanol was transferred to Chamber #4 and degassed. Then, a corresponding amount was poured into the graduated cylinder. Note that the water was always placed in the mixing cylinder first. This is because, for a given temperature, water has a lower saturation pressure than methanol, see Figure 5.15. If the methanol were to be placed in the mixing cylinder first, then the pressure in this cylinder would be greater than the chamber containing the water. This pressure difference would not immediately allow the water to enter mixing cylinder. Finally, the mixture was let into the previously evacuated wick based coldplate. Once the binary mixture was sealed into the cavity by closing the coldplate valve, its temperature and pressure were measured and compared to reference values in order to verify the mass fraction and quality of degassing. The only thermodynamic data found for binary mixtures of water and methanol was at temperatures of 50°C and above. Figure 5.17 displays a plot of the vapor pressure of water-methanol binary mixtures at 50°C for the full concentration range [2]. Therefore, the coldplate was heated until

the liquid and vapor temperatures reached 50°C and the pressure was measured and verified against the reference value.

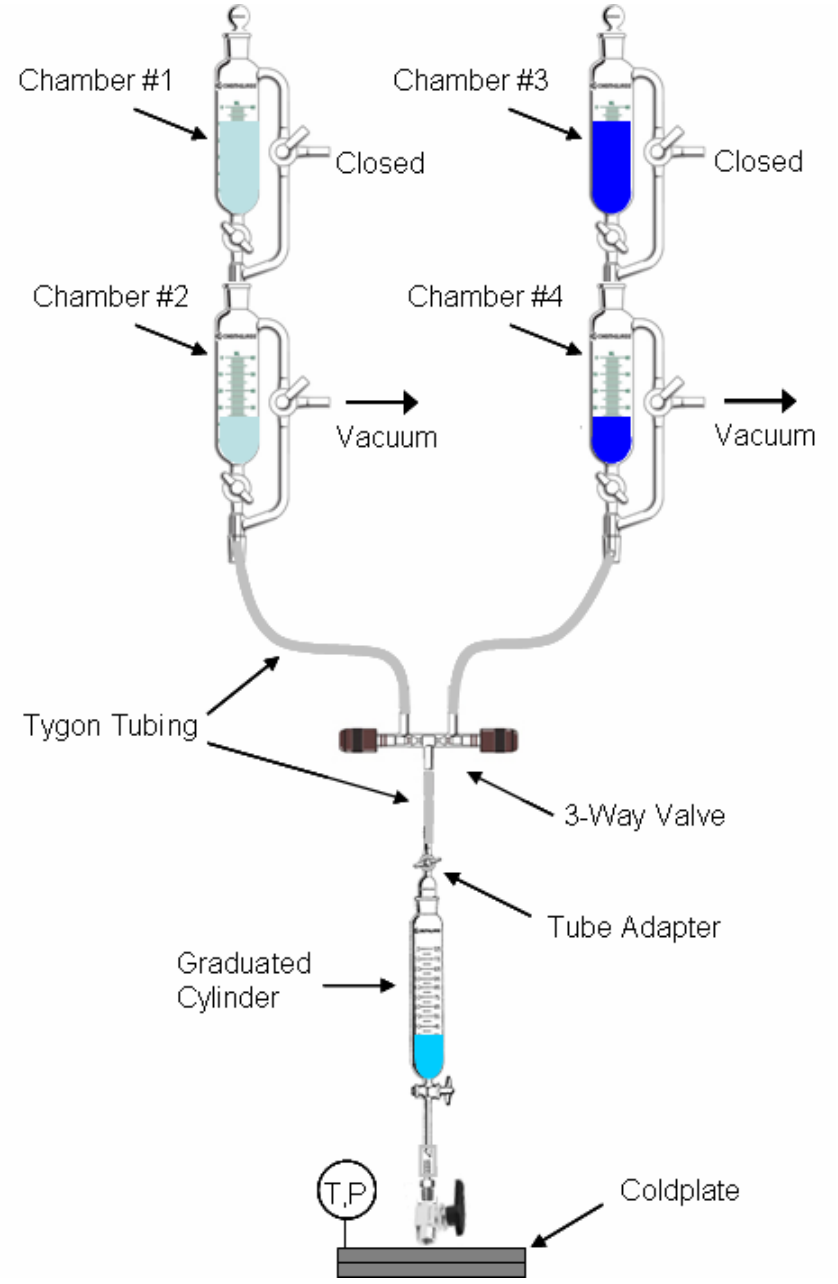

Figure 5.16 Binary Mixture Degassing System

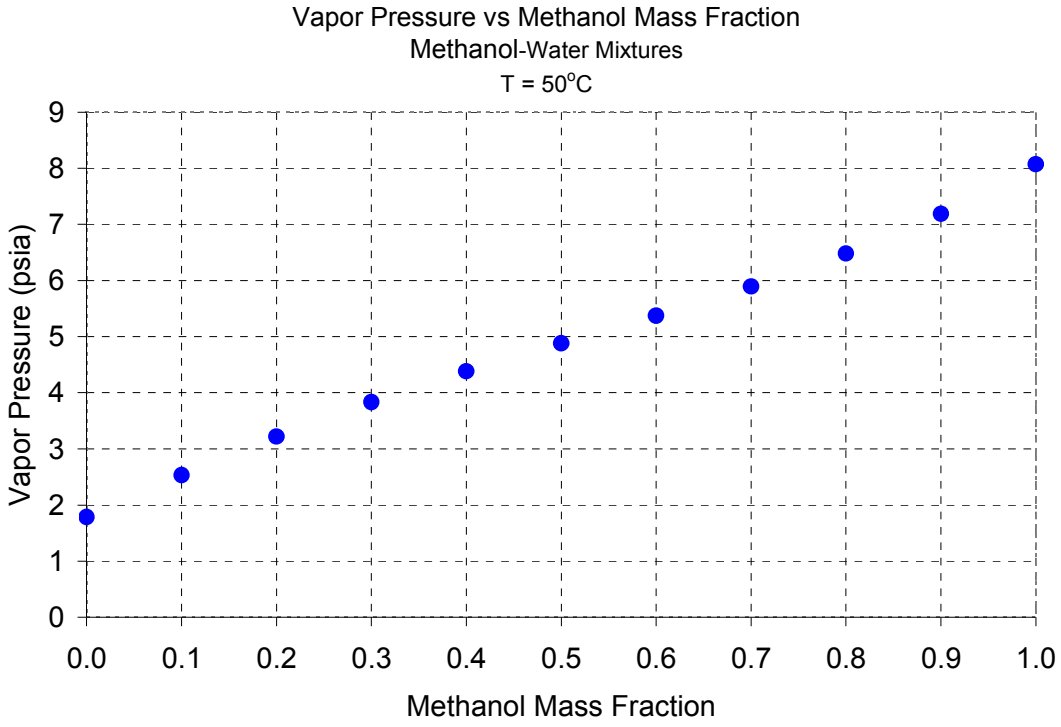

Figure 5.17 Vapor Pressures of Water-Methanol Mixtures at 50°C

5.3 Test Setup and Procedure

The overall goal of the steady state test setup was to measure the thermal resistance across the length of the wick-based coldplate. One end of the coldplate would be heated by strip heaters and the other end would be cooled by a chilled water coldplate. Input power would be varied to establish thermal performance as a function of heat flux. Evaluations were performed with the wick-based coldplate in both the horizontal and vertical positions.

Figures 5.18 and 5.19 depict the top and side views, respectively of the wick-based coldplate in the horizontal position. Two thermocouples (T-type, 36 gage) were used to measure temperatures in the coldplate cavity. Six similar thermocouples were placed

externally, three on the hot side and three on the cold side. The thermocouples on the cold side were sandwiched between the bottom of the wick-based coldplate and a thermal pad, which was used to minimize the contact resistance between the wick-based coldplate and the chilled water coldplate. An Omegadyne absolute pressure transducer (PT) PX35D0-050AV was used to track the internal pressure. Two Minco 100 Watts flexible strip heaters were used as variable input heat sources. One was placed on the cover and one was placed on the baseplate, see Figure 5.19.

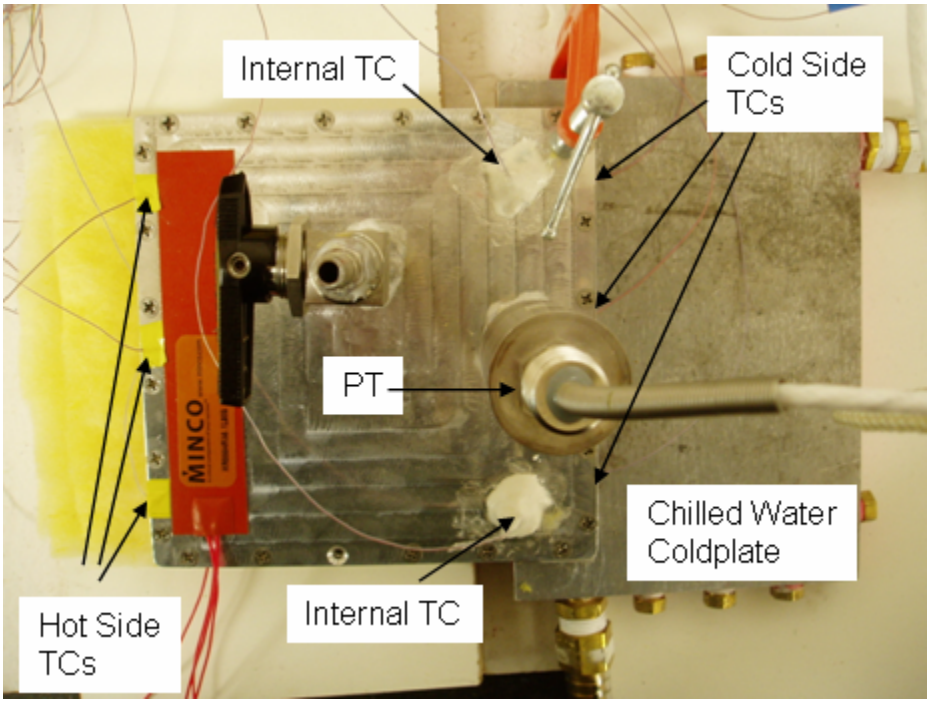

Figure 5.18 Top View of Steady State Test Setup

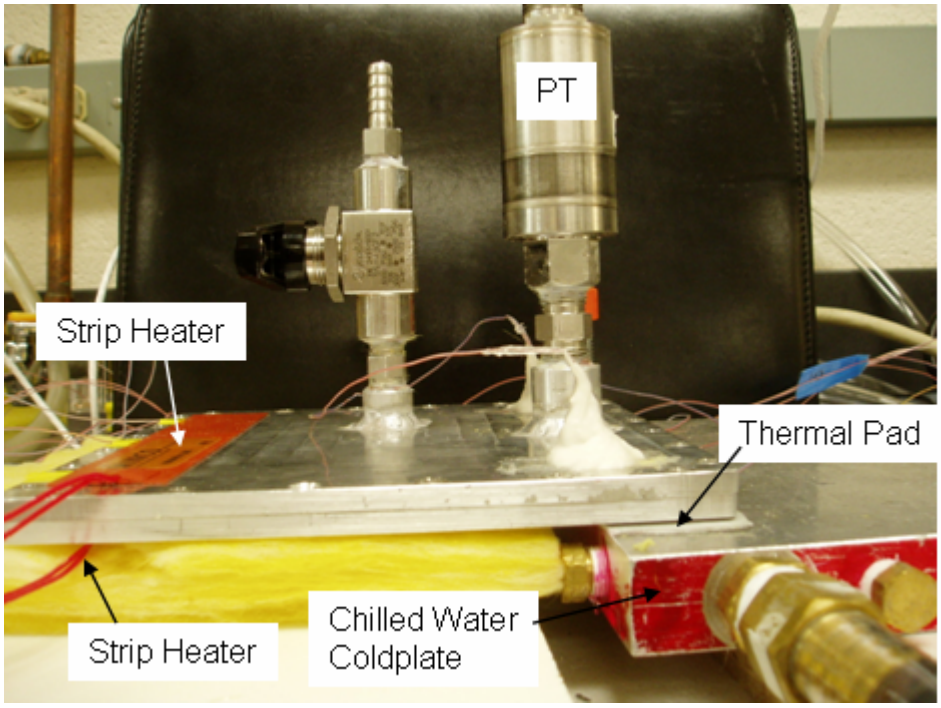

Figure 5.19 Side View of Steady State Test Setup

5.3.1 Uncertainty Analysis of Steady State Test

The uncertainty in determining the thermodynamic state of the fluid within the coldplate was estimated. Internal pressures were measured using the pressure transducer previously described. This device had a range of 0-50 psia and reported errors of ±0.25% full-scale output (FSO) due to the combination of linearity, hysteresis, and repeatability, plus a zero balance error of ±2.0% FSO. Errors due to thermal effects (operational temperature range: -73 to 163°C) were in the noise (±0.004% FSO/°F). Internal temperatures were measured using two thermocouples, each having a potential error of ±1°C. In an effort to get all error sources in the same units, the temperature error was translated into an equivalent pressure error by using the

saturation curves for water and methanol. For water at room temperature, a ±1°C error becomes ±0.024 psia or ±6.4%, while for methanol the same error in temperature becomes ±0.112 psia or ±5.3%. The average value of ±5.85% was used as the error attributed to a single thermocouple. Again, the RSS method was used to combine all error sources and the resulting design stage uncertainty for determining the thermodynamic state was ±8.5% in terms of absolute pressure. In other words, for a given temperature, if the measured pressure of the fluid within the wick-based coldplate was within ±8.5% of the reference value, then it would be statistically equivalent.

5.3.2 Seal Verification

Since having a well degassed working fluid and maintaining a good seal was so critical to these steady state thermal evaluations, seal verification tests were performed on the coldplate prior to performing a series of tests. Figure 5.20 displays a plot of the pressure inside the wick based coldplate filled with degassed water. Recall that during the degassing process, the system is first evacuated and then the degassed liquid is inserted. Consequently, the pressure curve drops from ambient and approaches zero, while the cavity is being evacuated. Once the liquid is introduced to the cavity the pressure increases to the saturation pressure corresponding to the given temperature, which was typically near room temperature. If the coldplate had a gross leak, the internal pressure would quickly return to ambient. However, for a small leak in the system the pressure increase was much more subtle. Therefore, long term pressure monitoring was required.

For the verification test depicted in Figure 5.20, the initial pressure after the liquid was inserted into the coldplate was 0.394 psia; only a 4.3% delta from the reference value of 0.377 psia. This delta was well within the uncertainty of the apparatus. After 4, 8, 12, and 16 hours, the internal pressure had increased to 24.4, 49.4, 74.3, and 79.6%, respectively, indicating that there was a small leak in the system. The internal temperature of the cavity varied by ±1.5°C for the duration of the test, probably tracking the lab's ambient temperature. Even tough the

steady state tests typically only lasted for two to three hours; this leak rate was not acceptable. Common leak locations were at the thermocouple access holes and the many thread fitted joins of the pressure transducer and coldplate valve. The least problematic area was the large face seal created by the O-ring along the perimeter of the coldplate.

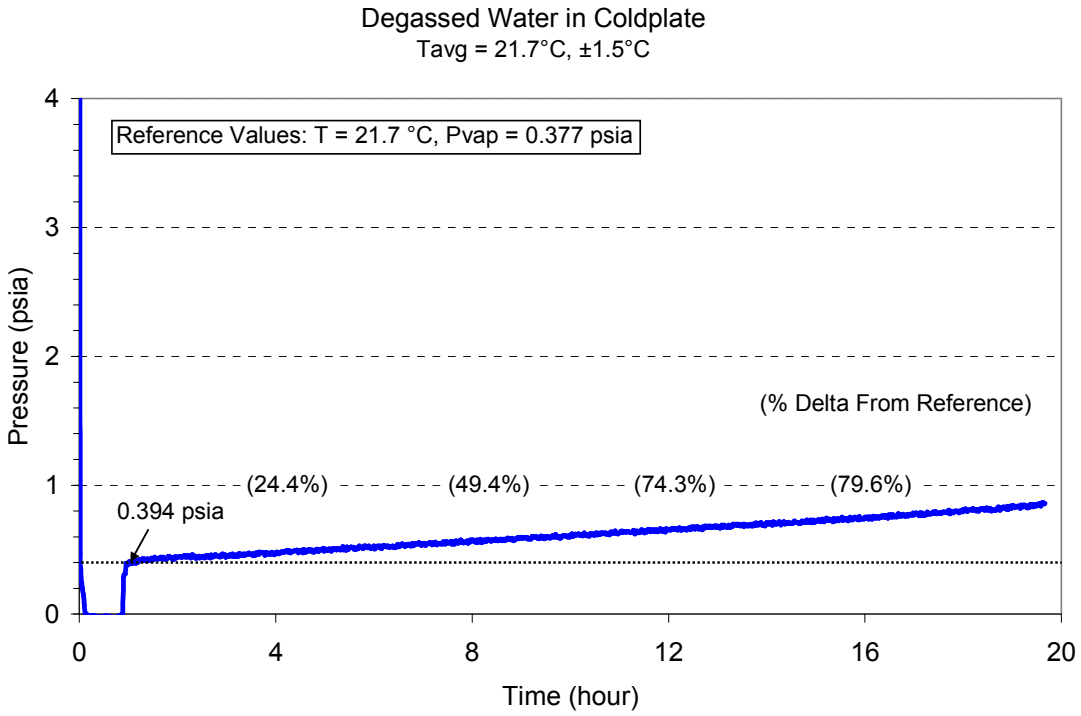

Figure 5.20 Example of a Poorly Sealed Coldplate (Water)

Once the coldplate was deemed to be leaky, the system would be pressurized and submerged in a water bath in an effort to locate the leak. If a leak was detected, the culprit area was resealed, however sometimes the leak was so small that its source location was not discernible. In these cases, the sealant material on all fittings was removed and reapplied. Figure 2.21 illustrates the internal pressure of a well sealed coldplate filled with water for the duration of a seal verification test. Initially, the pressure of the fluid was 0.407 psia, only a 1.2%

delta from the reference value at the average measured temperature. This pressure was held within a very tight band, only varying with the ambient air temperature.

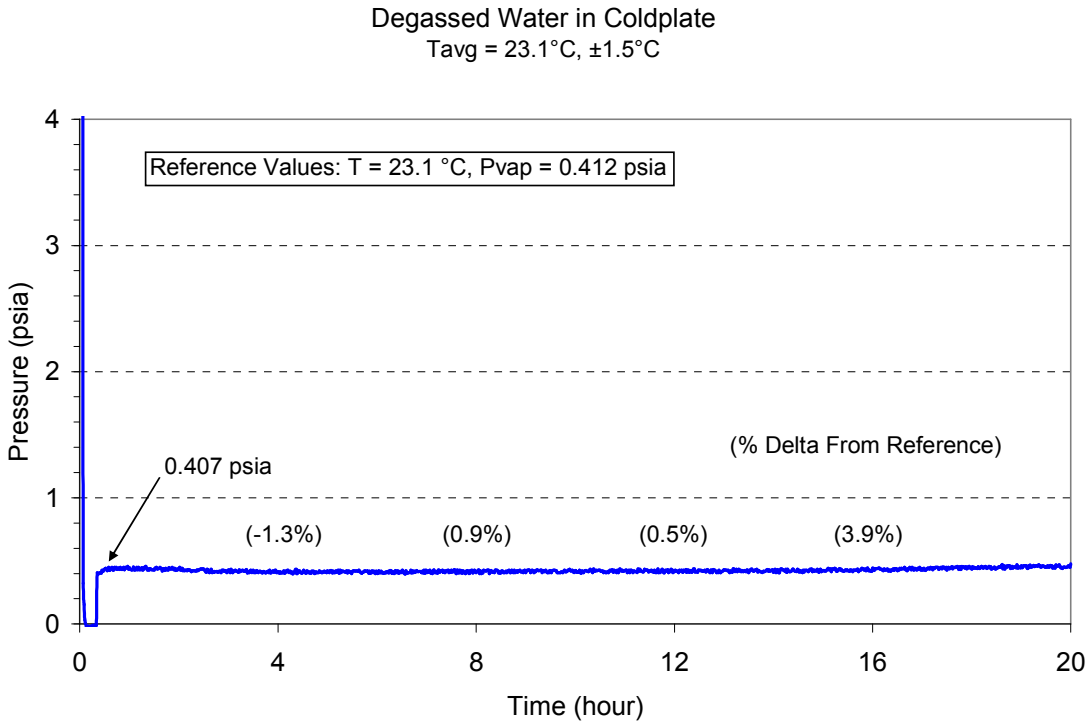

Figure 5.21 Example of a Well Sealed Coldplate (Water)

Next, the coldplate was filled with methanol and the pressure was monitored to verify adequate sealing. This was also a true test of how well all of the materials in the system would stand up to methanol's corrosive nature. Figure 5.22 illustrates the measured internal pressure, which matched well with the published saturation pressure at the given temperature. Interestingly enough, the pressure curve followed the diurnal cycle, decreasing slightly as the lab cooled off at night and increasing the following day.

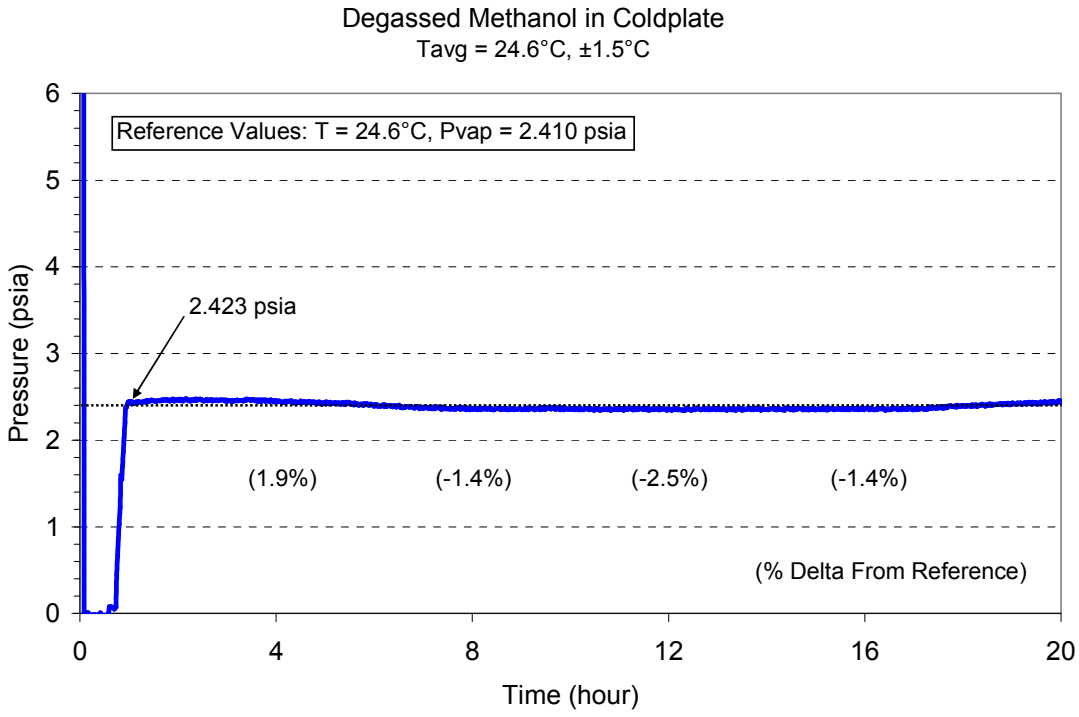

Figure 5.22 Example of a Well Sealed Coldplate (Methanol)

5.3.3 External Thermocouple Placement

In order to accurately determine the thermal resistance across the wick-based coldplate, the temperature extremes had to be measured. In other words, the thermocouples had to be placed in the hottest location on the hot side and on the coldest location on the cold side. Placement of the thermocouples on the cold side was straightforward; they were sandwiched between the bottom of the coldplate and the thermal pad, see Figure 5.19. On the hot side, it was convenient to simply place the thermocouples on the left edge of the coldplate right next to the strip heater, see Figure 5.18. However, it was not known if these locations accurately represented the hottest points on the system. In light, a finite element analysis (FEA) was performed to determine if these convenient thermocouple locations adequately represented the hottest points.

Using symmetry, a numerical model of half of the coldplate was constructed, see Figure 5.23. The dashed line in the figure represents the cavity outline. Initially, the coldplate was simulated and measured with the cavity evacuated. Figure 5.24 shows the inner side of the top cover. Areas highlighted in blue and navy blue represent the regions in contact with the baseplate. The area highlighted in blue was given a heat transfer coefficient as a boundary condition to represent the heat loss to the chilled water coldplate.

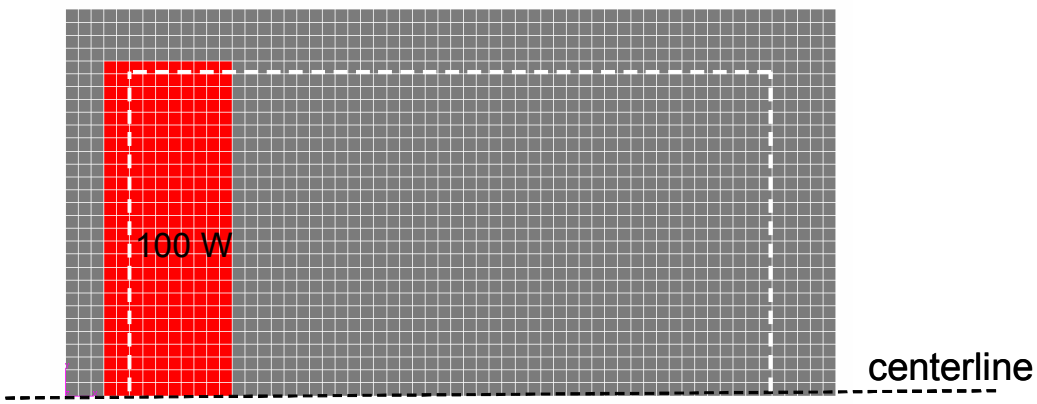

Figure 5.23 Top View of Numerical Model

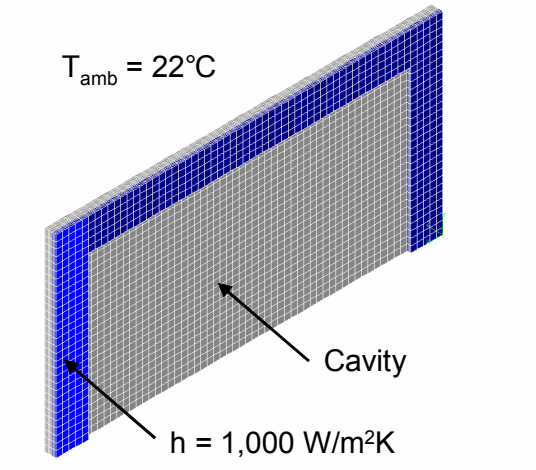

Figure 5.24 Isometric View of Inner Side of Coldplate Cover

The finite element model was solved, and measurements were taken with the coldplate cavity evacuated. Both numerical and empirical results are displayed in Figure 5.25. Temperatures in black were generated by the numerical model, and temperatures in blue were measured. The heat transfer coefficient in the model was adjusted until the temperatures at the two thermocouple locations were in acceptable agreement with the measured values. The predicted temperatures at the current thermocouple locations could then be compared to the hottest temperature in their perspective areas. The maximum delta occurred along the centerline of the coldplate (near thermocouple 2) and there was only a 0.2°C delta between the thermocouple location and the hottest point on the coldplate.

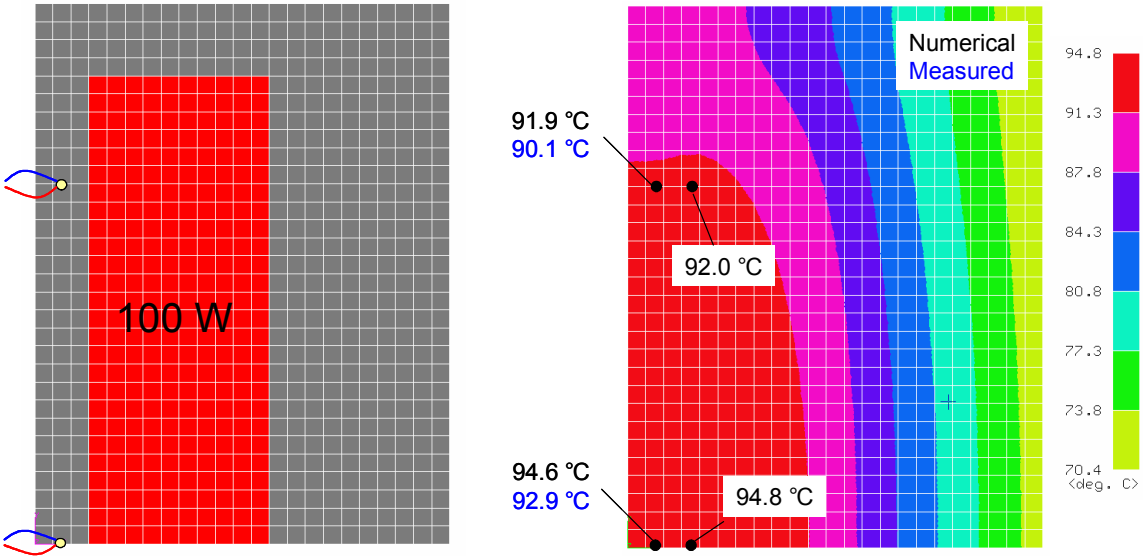

(a) (b)

Figure 5.25 Finite Element Grid of Heater Area (a) Temperature Profile of Cover with Empty Cavity (b)

Next, the model was modified by increasing the input power to 150 Watts and by adding a heat transfer coefficient to the cavity, representing heat consumed due to phase change. The area affected by this additional heat transfer coefficient is highlighted in green in Figure 5.26.

Since the heat exchange between the top cover and the evaporating fluid within the cavity was not known, the simulation was performed using a heat transfer coefficient of 100.0, 1,000.0, and 10, 000.0 W/m^{2}K. Resulting temperature profiles are displayed in Figure 5.27, and temperature values are listed in Table 5.2. Again, temperature deltas between the thermocouple location and the hottest spot on the cover were minimal. As a result, the hot side thermocouples were placed in the location shown in Figure 5.18 for all steady state evaluations.

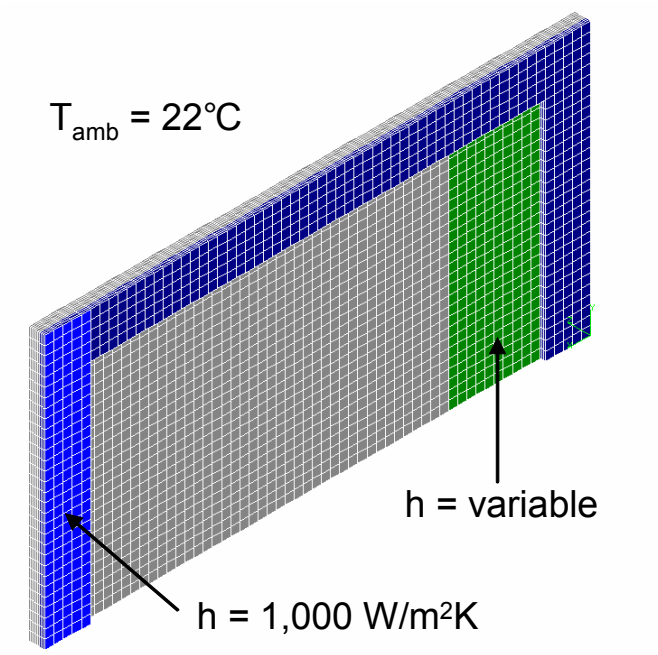

Figure 5.26 Modified Numerical Model

Table 5.2 Predicted Temperatures for Modified Numerical Model

	Heat Transfer Coefficient in Cavity (W/m^2K)		
	100	1,000	10,000
Thermocouple Temperature (°C)	116.4	45.4	26.2
Maximun Temperature (°C)	116.5	45.5	26.4
Delta	0.1	0.1	0.2

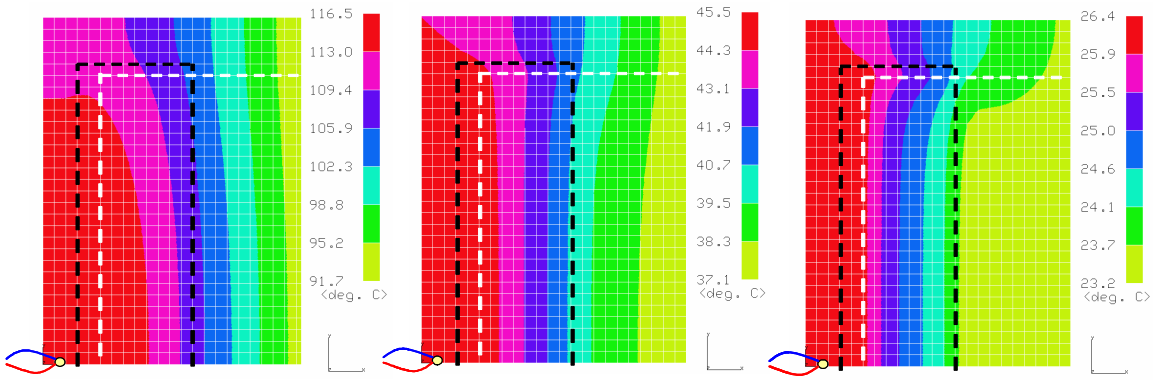

Figure 5.27 Cover Temperature Profiles for Cavity Heat Transfer Coefficients of (a) 100 (b) 1,000 and (c) 10,000 W/m^2K

5.3.4 Steady State Test Procedure

Once a degassing procedure was established, the coldplate was checked for leaks, and the temperature sensors were located, the wick-based coldplate was evaluated to determine its steady state thermal resistance for a variety of configurations. For each trial, the desired wick structure was located within the coldplate; next, it was evacuated, and then filled with the desired working fluid. The thermodynamic state of the working fluid was then verified to ensure that the fluid was properly degassed and that there were no leaks in the system. For single fluids, the measured saturation pressure typically fell within 2% of the reference value. The setup was considered invalid if the delta between the measured and published values was

greater than 5%. For binary mixtures of methanol and water, the measured pressure typically fell within 5% of the appropriate value. Mixtures were considered improperly degassed if the delta between the measured and reference value was greater than 10%. Mixtures had greater error due to the uncertainty of measuring the appropriate volumes to obtain the desired ratio.

Once the wicking material and working fluid were in place, the right edge of the wick-based coldplate was placed the water chilled coldplate with a thermal pad in between, see Figure 5.19. They were held together with the use of two C-clamps. Next, the wick-based coldplate would be covered with insulation to minimize heat loss to the ambient, see Figure 5.29. Next, the power supply was manually adjusted so that the strip heaters dissipated a total of 50 Watts. The total heat input area was 64.5 cm^2, thus the corresponding heat flux for this power input was 0.775 W/cm^2. Temperatures were allowed to reach steady state, which was defined as the rate of change being no greater than 2°C per hour as per Military Standard 810 [25]. Once the temperatures were stabilized, the power input was increased by an increment of 50 Watts. This was repeated until the pressures within the system reached two atmospheres or the output power of the flexible heaters was maxed out at 182 Watts. Consequently, input powers were 50, 100, 150, and 182 Watts and corresponding heat fluxes were 0.775, 1.550, 2.325, and 2.820 W/cm^2, respectively. A typical temperature profile is displayed in Figure 5.30. Once the tests were completed, the thermodynamic state of the working fluid was reevaluated to ensure that no leak developed during the test. Previously described criteria for measured pressures were applied. Finally, the delta between the average of the three hot temperatures and three cold temperatures was computed and used to calculate the thermal resistance of the system.

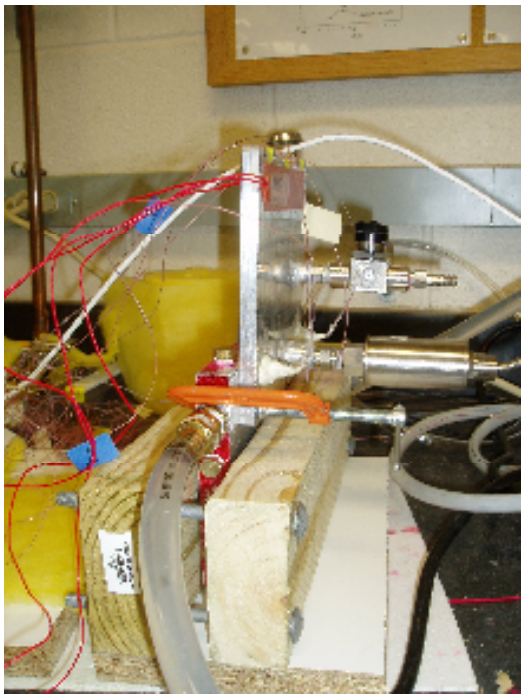

Figure 5.28 Wick-based Coldplate in Vertical Position

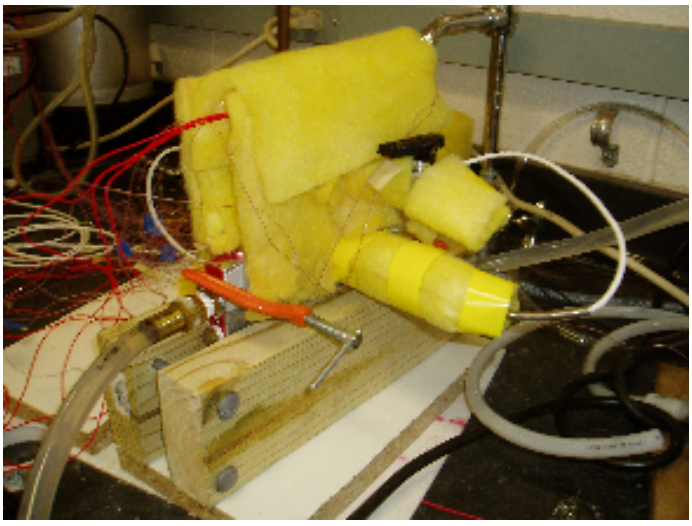

Figure 5.29 Wick-based Coldplate Covered with Insulation

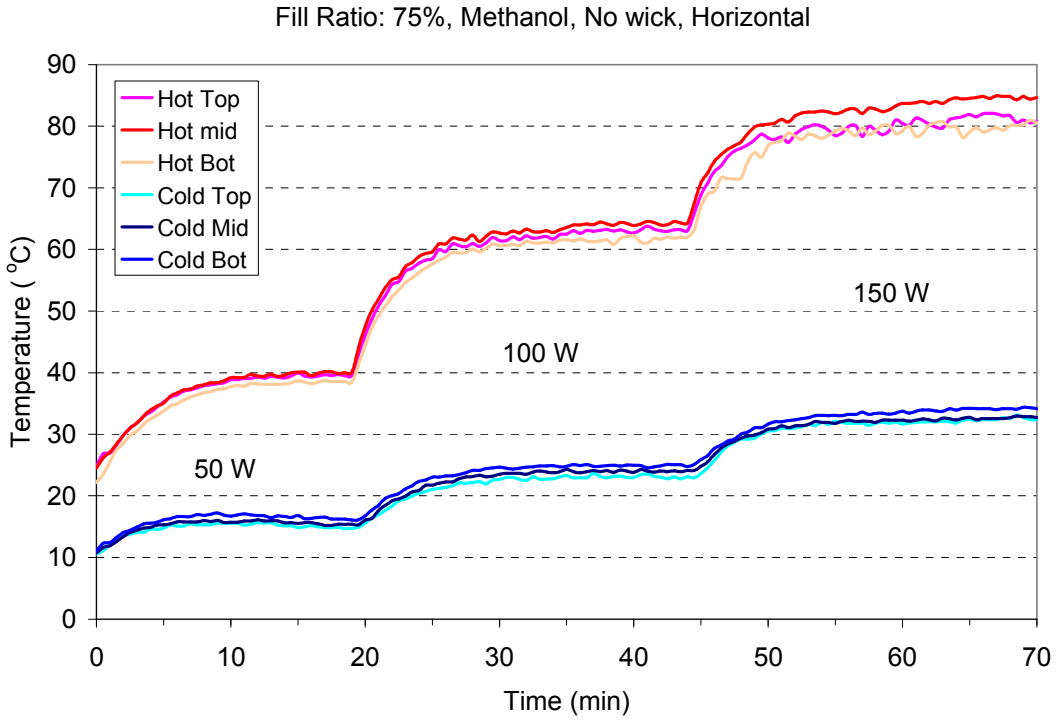

Figure 5.30 Typical Temperature Profile of Steady State Test

CHAPTER 6

STEADY STATE THERMAL RESISTANCE

Once a sealed wick-based coldplate had been assembled and a test procedure for measuring the thermal resistance was established, steady state empirical evaluations were performed. First, an aluminum thermal core was tested in order to establish a baseline thermal resistance value, which would be used as a reference to compare the performance of the proposed wick-based coldplate. Next, the fill ratio effect was studied to determine the most effective value. Next, various wick configurations were evaluated to determine the most efficient design for mass transport of both the liquid and the vapor. Finally, binary mixtures of alcohol and water were introduced to determine if the impressive enhancements achieved in the transient study applied to the steady state case.

6.1 Baseline Thermal Resistances

As previously discussed, conduction cooled electronics are typically cooled via a thermal core, which is a simple solid plate usually made of a high conductivity metal. In order for a wick-based coldplate to be implemented, its thermal performance must be superior to that of a thermal core. Consequently, a solid plate of aluminum with the same dimensions as the proposed wick-based coldplate (6 x 6 x 3/8 inch) was measured to provide a point of comparison. A simple, one dimensional conduction analysis gave a theoretical thermal resistance of 0.339°C/W. Empirical data is shown in Figure 6.1 and yielded a measured thermal resistance of 0.381°C/W. Thermal resistances of wick-based coldplates will have to exceed this value in order to have any argument for their use in systems requiring continuous operation.

In addition, the thermal resistance of an evacuated coldplate was measured. This provided a baseline thermal performance of the wick-based coldplate with only conduction at its disposal. Additional heat transfer due to phase change within the cavity could then be surmised once a working fluid was added. Temperature deltas across an evacuated wick-based coldplate were plotted (Figure 6.1) and the resulting thermal resistance was 0.724°C/W.

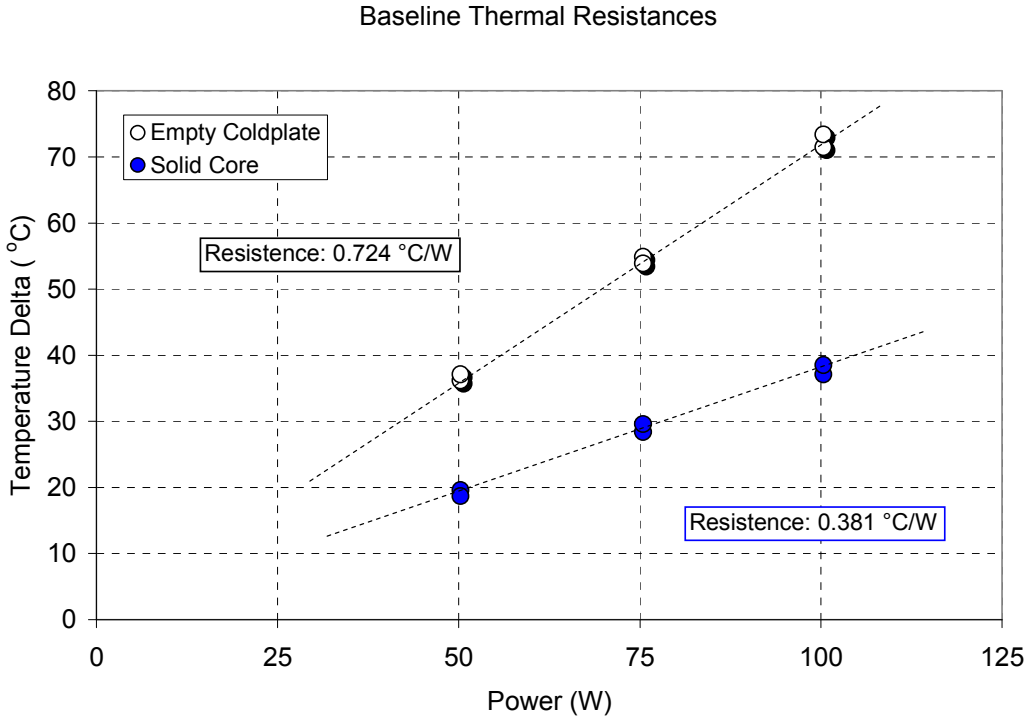

Figure 6.1 Baseline Thermal Resistances

6.2 Horizontal Test Results

6.2.1 Thermal Performance with No Wick

Initially, the coldplate was evaluated without any wicking material, in the horizontal position (Figure 5.19), a 75% fill ratio, and pure methanol as the working fluid. Fill ratio was determined by the ratio of volume occupied by the fluid to the total volume available in the

coldplate's cavity. If wicking material was placed in the cavity, the volume occupied by the porous solid was subtracted from the open volume total. Thermal resistance values were plotted (Figure 6.2) for this configuration. Two of the trials had a sealed coldplate throughout the test; in other words the thermodynamic state of the fluid was measured to be within 5% of the reference value throughout the test. For the trial considered "leaky", it was believed that the coldplate developed a small leak during the test because the thermodynamic state of the fluid at the end of the trial was significantly different from the accepted value. The pressure was 11% off of the expected value for the given temperature, which was a greater error than the known uncertainties. Results indicate that having a gassy working fluid negatively impacts thermal performance. Thermal resistance values for the leaky trial were on average 20% greater than for the sealed trials. Note that thermal resistance plots contain colored dashed lines representing the baseline resistance values. The green line represents the thermal resistance obtained with a completely empty coldplate cavity, and the brown line represents the value obtained with a solid aluminum plate.

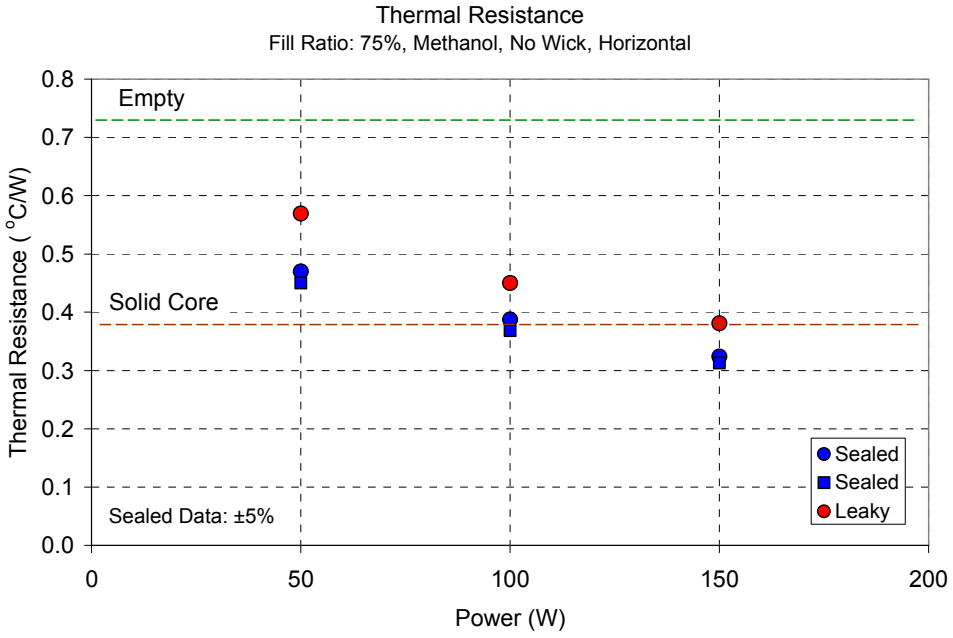

Figure 6.2 Thermal Performance of a Sealed vs. Leaky Coldplate

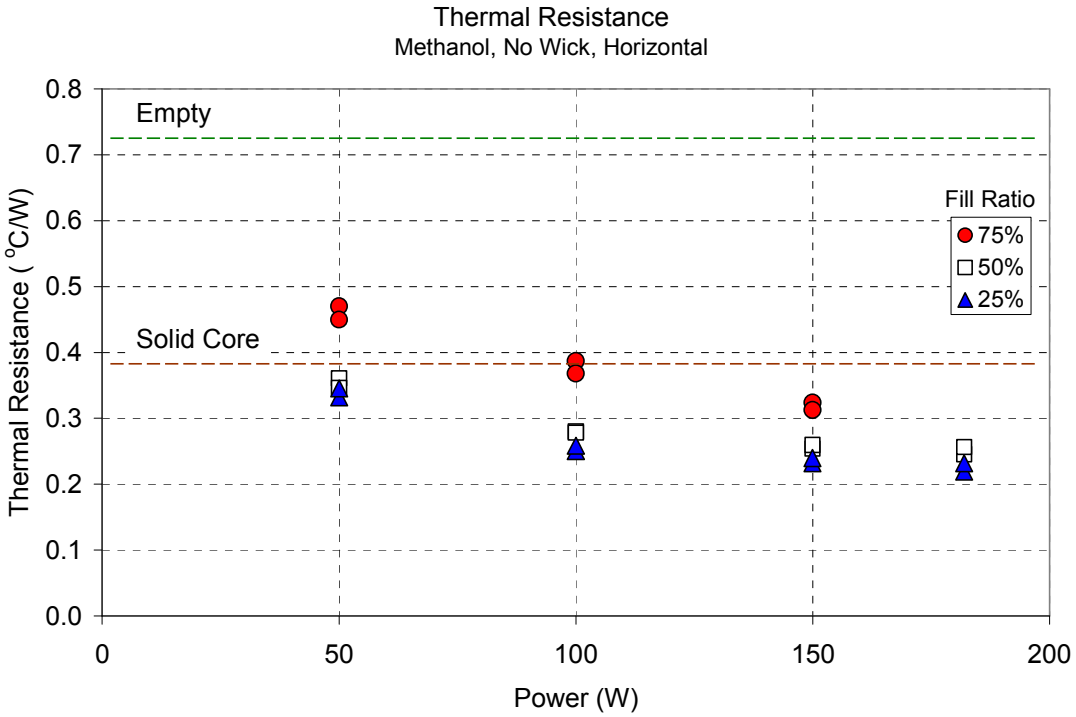

Figure 6.3 Thermal Performance as a Function of Fill Ratio (Methanol)

Next, the fill ratio was varied with methanol as the working fluid and no wick in the cavity. Fill ratios of 25, 50, and 75% were investigated and resulting thermal resistances are displayed in Figure 6.3. Heat input values were 50, 100, 150, and 182 Watts corresponding to heat fluxes of 5, 10, 15, and 18.2 W/in^2 (0.78, 1.55, 2.33, and 2.82 W/cm^2). For all three fill ratios, the thermal resistance decreased as a function of heat input, indicating that the two-phase heat transfer was enhanced with higher heat fluxes. Statistically, the 25 and 50% fill ratios performed the same, and at the highest heat flux, the thermal resistance was 38% less than that of the solid core. Note that the performance was leveling off at the higher heat fluxes. Unfortunately, the performance limit, or dry out point, was not determined because of limitations of the power supply. Interestingly enough, the performance for the 75% fill ratio was not as

good at the lower heat fluxes, but the slope was steeper. For this configuration, the test was stopped after the power input of 150 Watts because the internal pressure had exceeded the operational range of the pressure transducer, which at the time was 30 psia. The performance may have approached that of the other two fill ratios at the highest heat flux and may have exceeded it at even higher heat inputs.

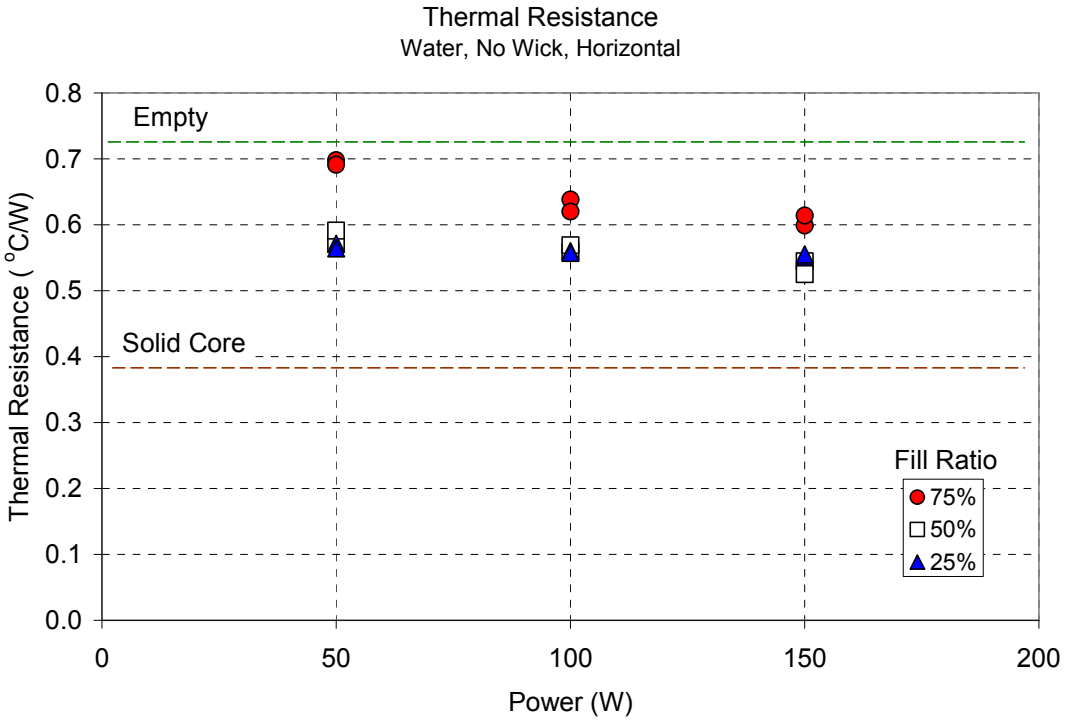

Figure 6.4 Thermal Performance as a Function of Fill Ratio (Water)

Next, the fill ratio study with no wick in the cavity was repeated using degassed water and resulting thermal resistances are illustrated in Figure 6.4. Again, the performance of the 25 and 50% fill ratios was comparable, while that of 75% lagged. Overall, the performance of water was deplorable with resistance values significantly greater than that of the solid core. The heat flux was not high enough to cause the water to change phase, consequently for the water

case, heat transfer was limited to single phase conduction. A comparison was made between water and methanol, see Figure 6.5. Methanol's favorable performance was due to its higher volatility, which allows it to change phase at these heat flux levels. Next, a 50% water and 50% methanol mixture was evaluated in triplicate and the resulting thermal resistance values, shown in Figure 6.5, varied by only 5%, which was well within the expected uncertainty. Furthermore, the average measured thermal resistance at the highest heat flux was 54% lower than that of the solid core.

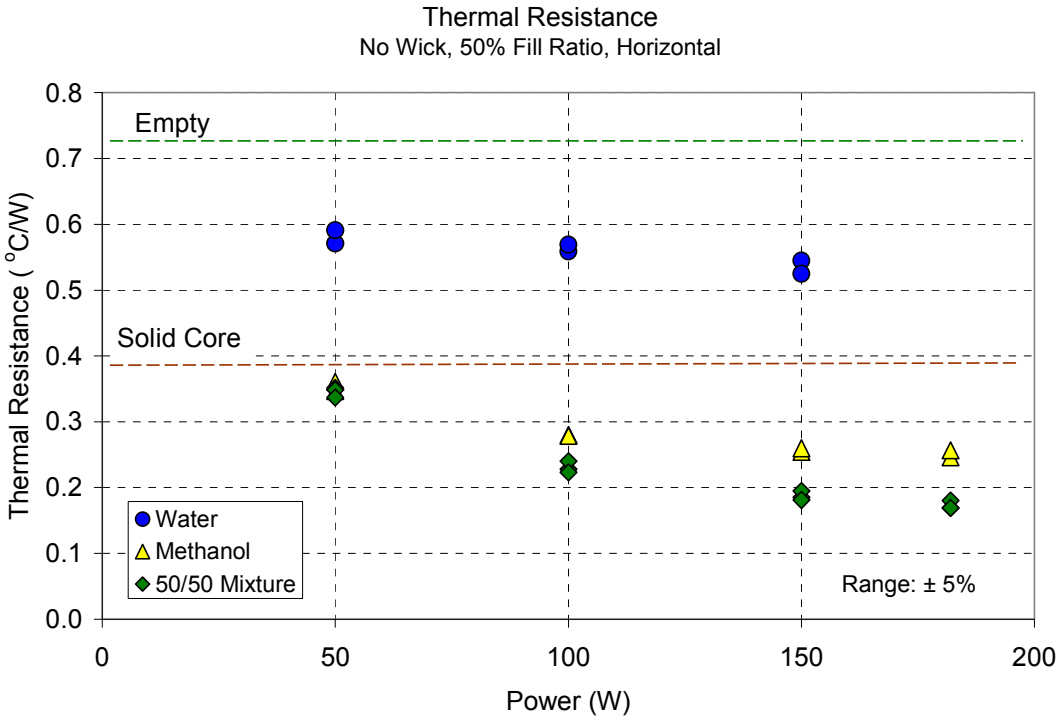

Figure 6.5 Thermal Performance Water vs. Methanol vs. 50/50 Mixture

6.2.2 Thermal Performance of Various Wick Configurations

Four wick configurations, depicted in Figures 6.6-9, were evaluated to determine which was most efficient in transporting liquid and vapor from one end of the coldplate to the other.

The main objective was to allow vapor generated at the heated end (the left side as depicted by the figures) to travel to the condenser end. Boiling or evaporation of the liquid would increase the pressure at the hot end of the coldplate, driving vapor to the cooler end. Once the vapor was condensed on the cold side, the wick was to transfer the liquid back to the hot side via capillary pumping action.

Figure 6.6 Full Wick Configuration

Figure 6.7 Wick Configuration having Two Gaps

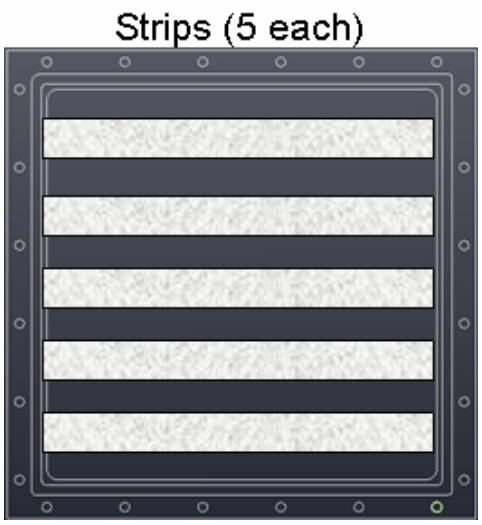

Figure 6.8 Wick Configuration having 1/2 Inch Strips (5 each)

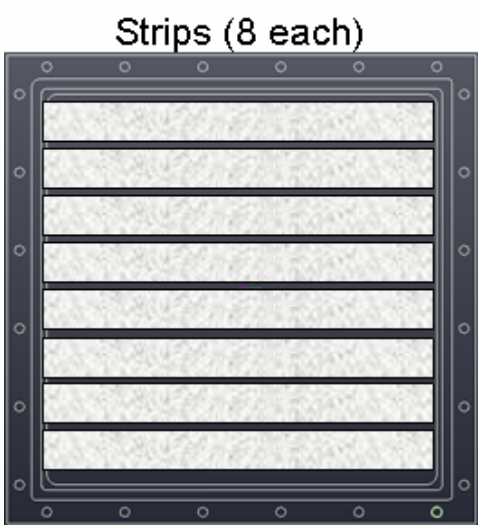

Figure 6.9 Wick Configuration having 1/2 Inch Strips (8 each)

The first configuration, Figure 6.6, had the wicking material completely filling the cavity. Next, half inch gaps were incorporated at the top and bottom of the cavity, see Figure 6.7, with the idea of having an open space for which the vapor could move freely. Next, the configuration was modified to include five (half inch) strips with large gaps in between, Figure 6.8. Finally, eight (half inch) strips were evaluated with small gaps in between, Figure 6.9.

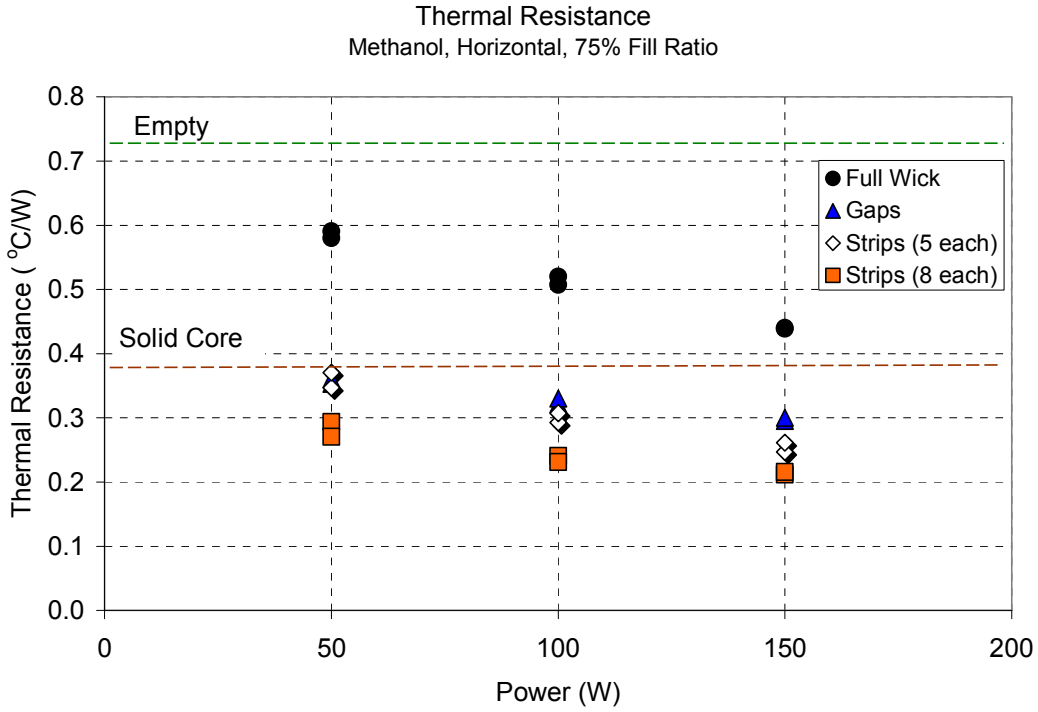

Figure 6.10 Thermal Performance of Various Wick Configurations

Thermal resistance values were plotted, see Figure 6.10, for all wick configurations and their relative performance was compared. By far, the worst performer was the full wick configuration. For this setup, the vapor had no clear path to the condenser side. Adding the two gaps on top and bottom improved the thermal performance significantly. The five strip configuration exhibited marginal improvement, and the eight strips had the best performance.

This indicates that large gaps were not required. A wick configuration having 15 (1/4 inch strips) was attempted, see Figures 6.11-12, but the strips were so thin that they moved during the evacuation process.

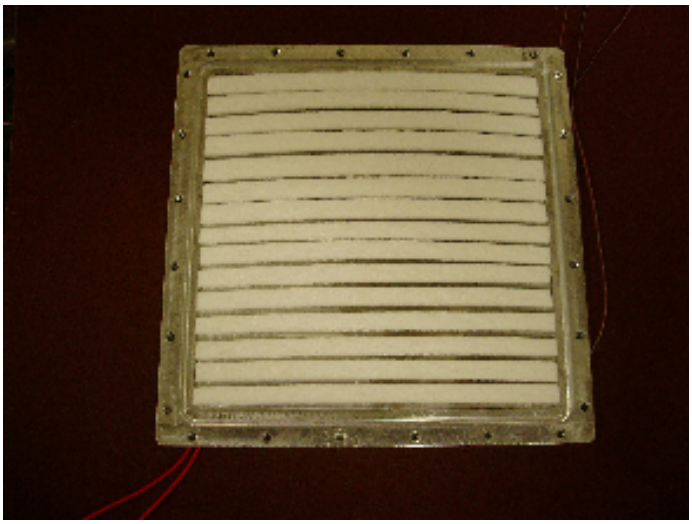

Figure 6.11 Wick Configuration having 1/4 Inch Strips (15 each)

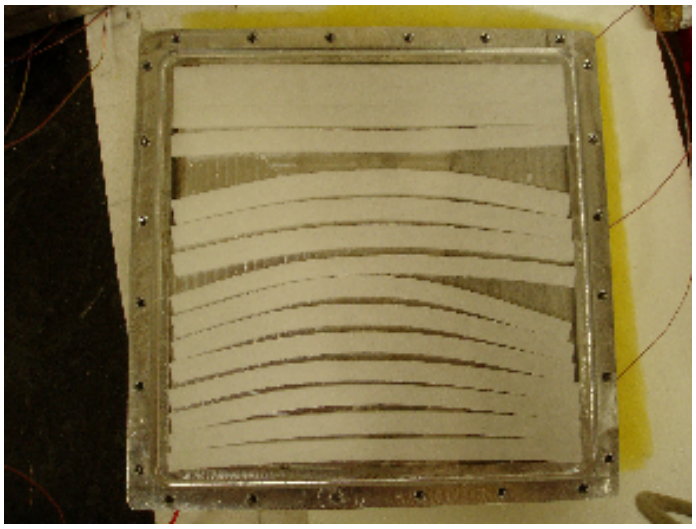

Figure 6.12 Strip Position Shift due to Vacuum Process

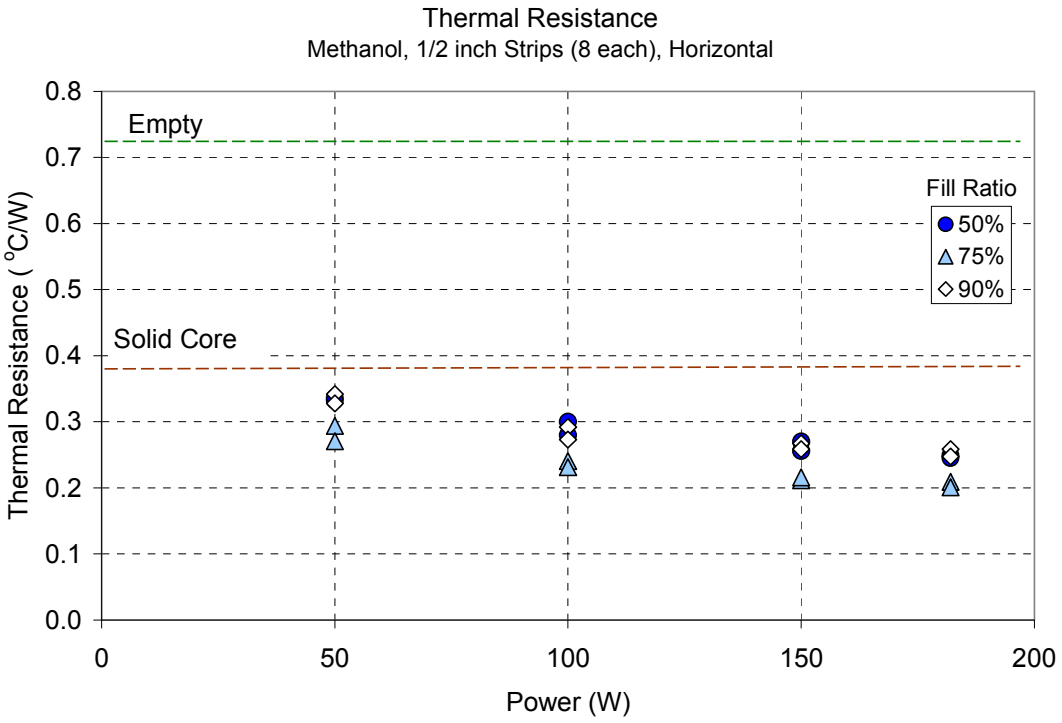

Figure 6.13 Thermal Performance of Best Wick Configuration as a Function of Fill Ratio

Since the eight (1/2 inch) strip configuration had the best steady state thermal resistance, it was selected for the remainder of the study. Next, the fill ratio was varied to study its effect with wicking material introduced. Fill ratio comparisons are displayed in Figure 6.1. There was a significant improvement in performance by increasing the fill ratio from 50 to 75%. At 50% much of the liquid was trapped by the wicking material, potentially causing dry out. At 75% more liquid may have been available for phase change. Interestingly enough, at a fill ratio of 90% the performance reverted back to that of 50%. This indicates that having too much liquid in the cavity may adversely affect the phase change dynamics. In light, a fill ratio of 75% was used for the remainder of the evaluations.

6.2.3 Thermal Performance of Binary Mixtures

Once the optimum wick configuration and fill ratio was established, the use of binary mixtures was investigated. For this study, the fill ratio was maintained at 75% and the eight (half inch) strip configuration used. The thermal performance of a methanol-water binary mixture with a 30% methanol concentration was plotted (Figure 6.14). Results indicate a large disparity between the performances at the heat flux extremes. The thermal resistance at a 50 Watt input was approaching that of an empty coldplate, indicating that at this heat load the phase change mechanism was only slightly activated. As the heat input was increased the thermal resistance decreased dramatically, reaching almost a third less than that of the solid core at the highest heat flux.

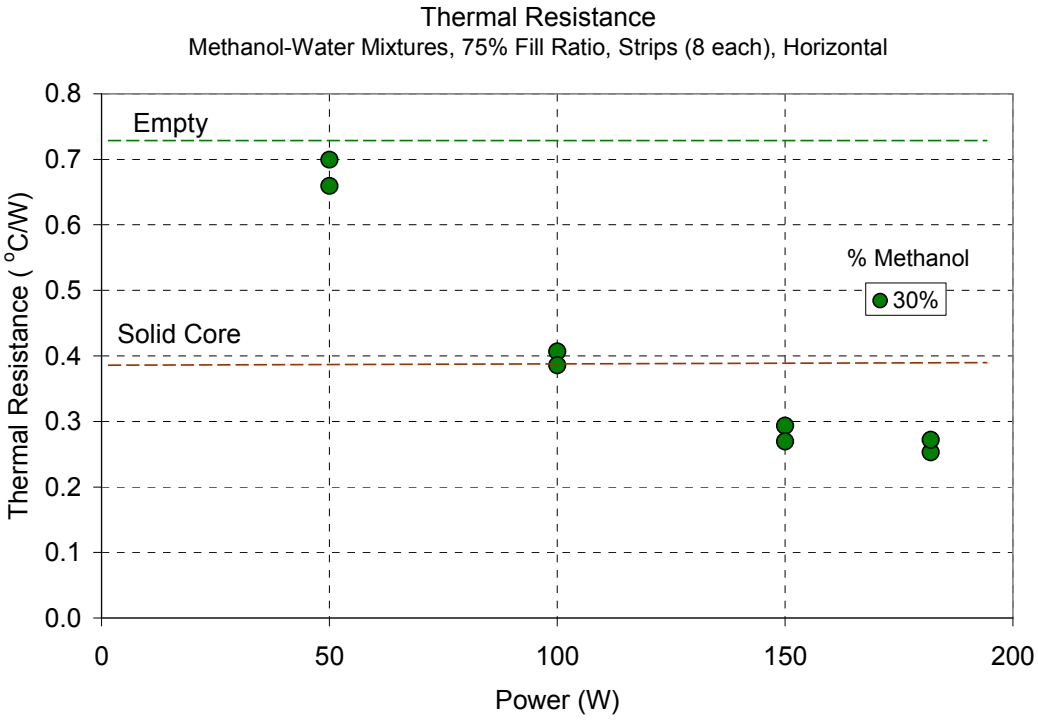

Figure 6.14 Thermal Performance with Mixture of 30% Methanol and 70% Water

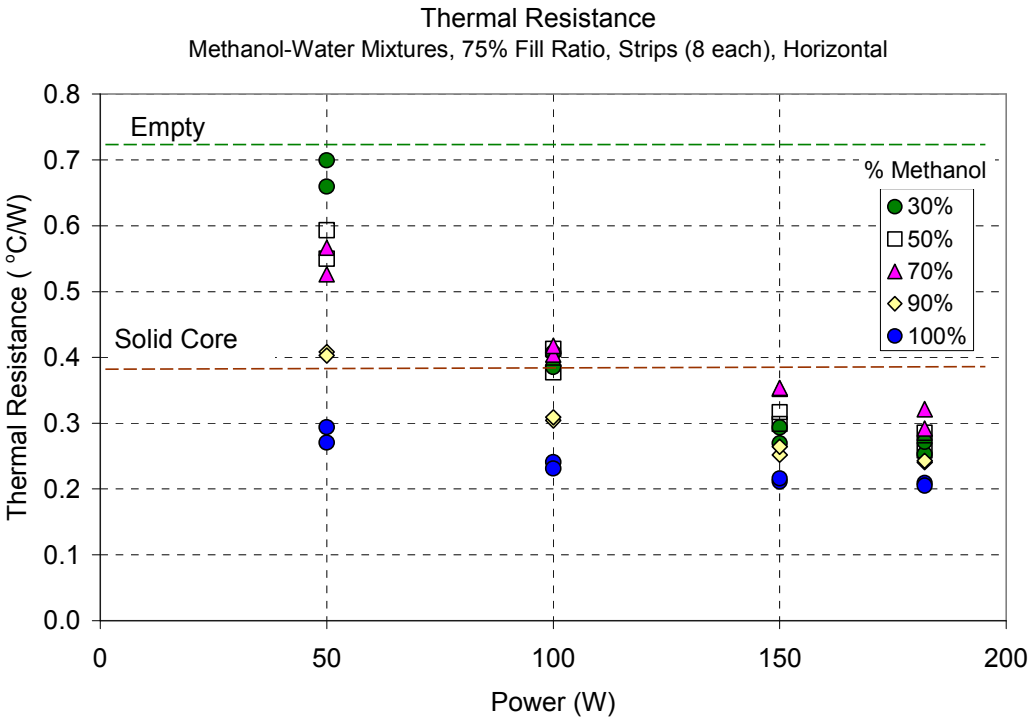

Figure 6.15 Thermal Performance of Methanol-Water Mixtures (Horizontal)

The full concentration range was evaluated and resulting thermal resistances are displayed in Figure 6.15. This data indicates that the disparity in performance between the heat flux extremes diminishes with an increasing methanol concentration. This was most likely due to methanol's high volatility, which requires less heat input in order to activate phase change. Furthermore, the data indicates that the overall thermal resistance across the coldplate was improved with increased concentrations of the alcohol. A potential explanation is that since methanol iss more volatile, it evaporated first leaving a mixture with a high concentration of water within the wick. This preferential evaporation of the volatile component in a binary mixture has been observed in previous research [26-29]. The high concentration of water within the wick may have served as a barrier, which blocked the freshly condensed methanol from

returning to the heated side. The pure methanol case had the lowest resistance, which was approaching half (46% less) of that of the solid core.

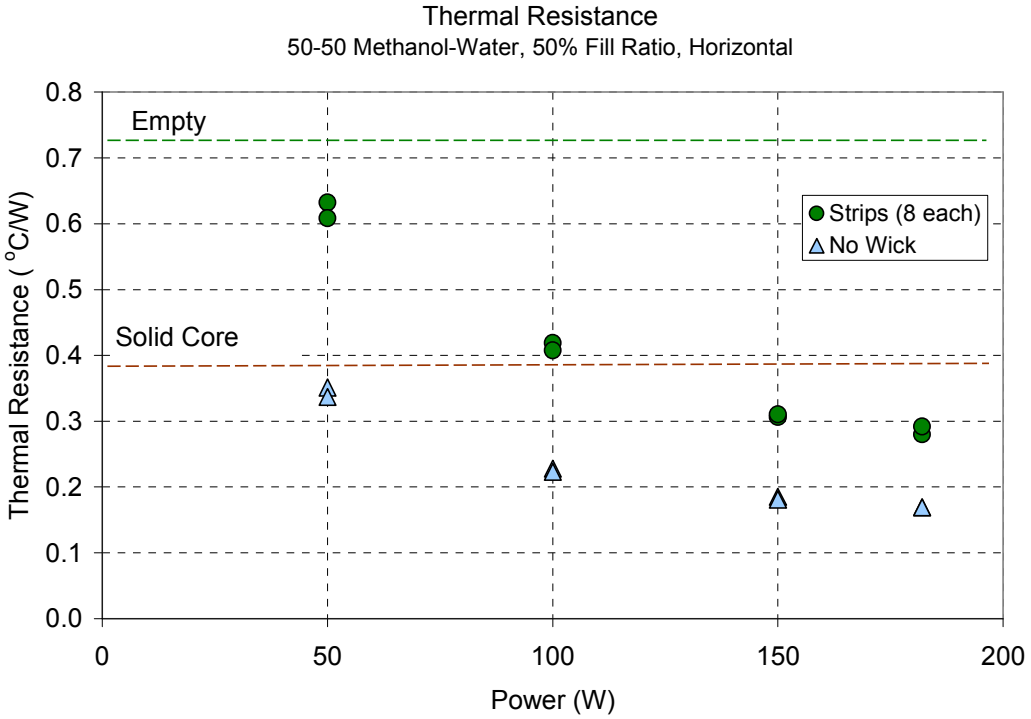

Figure 6.16 Thermal Performance of Wick vs. No Wick (Horizontal)

Direct comparisons were made between the performance with and without wicking material for 50% water and 50% methanol binary mixture, see Figure 6.16. Results clearly indicate that the wicking material diminishes the performance with the coldplate in the horizontal position. In this position, with no wicking material, the fluids are fairly free to move back and forth between the condenser and evaporator sections. Once the wick was introduced, the wickability of the liquids became a factor. The methanol in the mixture in all likelihood changed phase first, leaving the poor wicking water within the porous medium, which perturbed the two-phase cycle.

6.3 Vertical Test Results

Initially, the wick-based coldplate in the vertical position (Figure 5.28) was evaluated without the wicking material. This data was compared to that of the horizontal position and results are illustrated in Figure 6.17. The performance of the coldplate in the vertical position with no wick, methanol, and a 50% fill ratio was comparable to that of an empty coldplate. This was not a fair comparison because in the vertical position the liquid had no way of getting up to the heated area without wicking material to transport it.

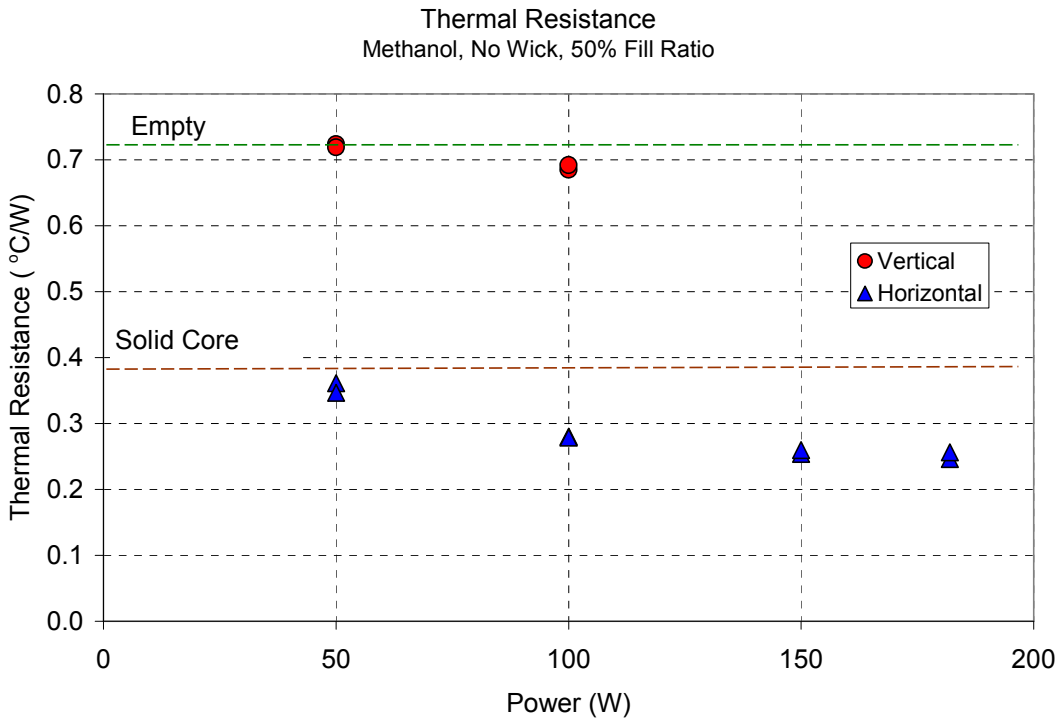

Figure 6.17 Thermal Performance of Vertical vs. Horizontal (No Wick)

Next, half inch (8 each) ceramic strips were added to the coldplate and results were compared, see Figure 6.18. This was a more reasonable comparison since now the liquid in the vertical position has some means of approaching the heated surface. The curvature in the

data for the vertical position suggests that the thermal limit may have been reached within the tested heat input range. However, this was difficult to confirm due to the uncertainty of the measurements. Using pure methanol, the thermal resistance in the vertical position was only 18% less than that of the solid core.

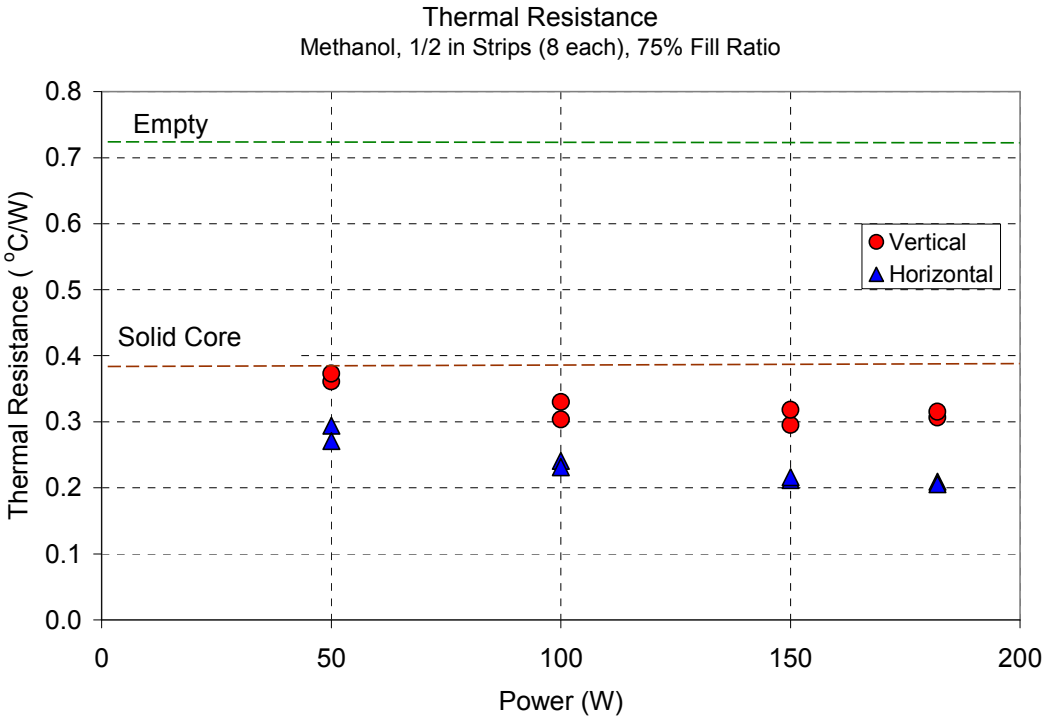

Figure 6.18 Thermal Performance of Vertical vs. Horizontal (Wick)

Next, binary mixtures were introduced to the coldplate in the vertical position and resulting thermal resistances were plotted (Figure 6.19) for the full methanol concentration range. The results were very similar to that in the horizontal position, except that the performance was degraded due to the force of gravity acting against the capillary pumping action. Similarly though, there was a large disparity in the thermal resistance for the low power input with the

values somewhat converging at the highest input power. Again, pure methanol out performed the methanol-water binary mixtures.

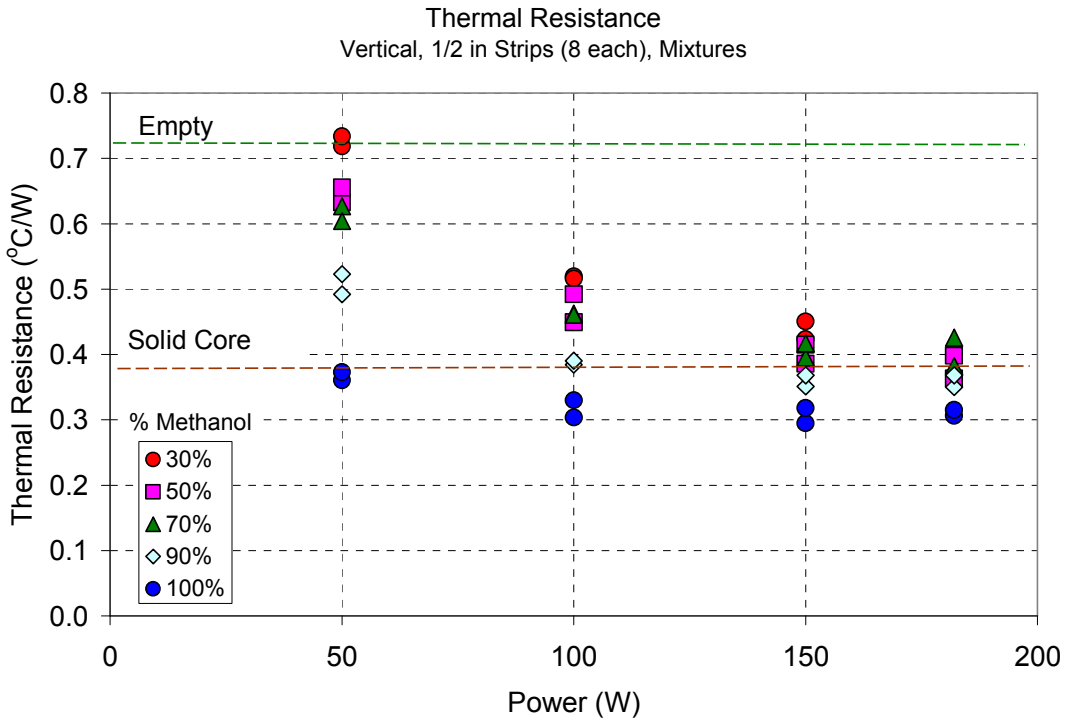

Figure 6.19 Thermal Performance of Methanol-Water Mixtures (Vertical)

6.4 Phase Change Mechanism

It was not certain what the dominant phase change mechanism was for the sealed wick-based coldplate with methanol. In light, a Lexan baseplate was fabricated and used to observe the fluid as it was being heated. The coldplate was filled to 75% capacity with pure methanol, and the aluminum cover received heat input (90 Watts or 2.8 W/cm^2) from the strip heater. Initially, no wicking material was used. A distinct vapor region was created on the heated side and a clear vapor-liquid interface was established, see Figure 6.20. Relatively

small boiling regions were observed and are displayed in Figure 6.21; bubbles were observed at the edges near the corners of the heat side and at two small circular areas within the vapor region. However, these regions comprised only a small fraction of the total heated surface area. This suggests that the dominant phase change mechanism was evaporation.

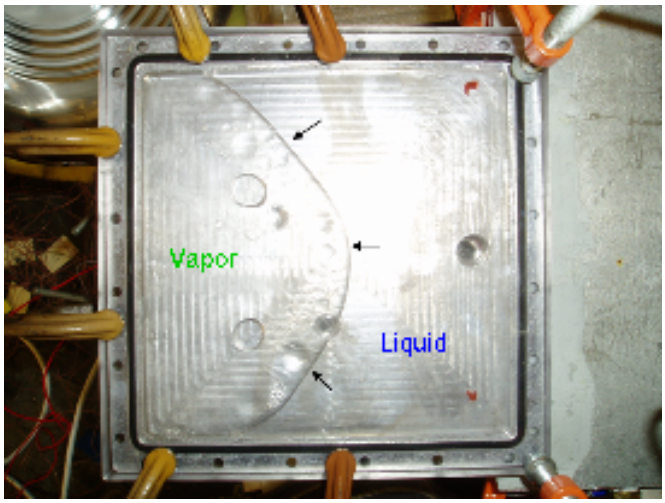

Figure 6.20 Coldplate with Transparent Baseplate

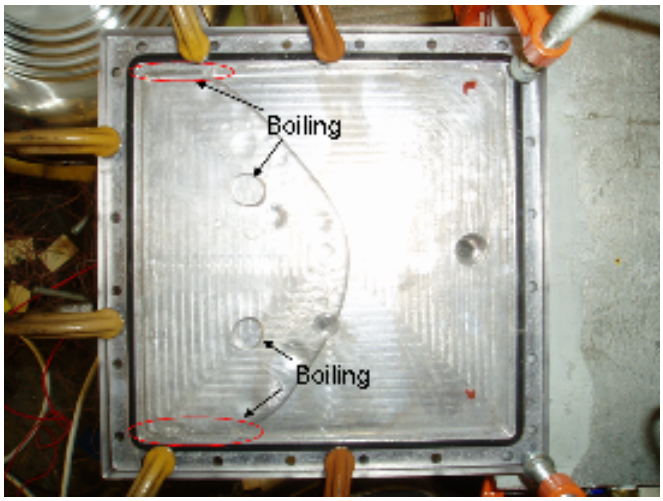

Figure 6.21 Observed Boiling Regions (No Wick)

Next, the coldplate was fitted with half inch (8 each) ceramic strips, see Figure 6.22. Again, bubble activity was observed only at the edges near the corners of the coldplate. Furthermore, activity was observed at only a couple of the gaps between strips, as indicated by the image. These limited boiling areas indicate that much of the phase change was due to evaporation.

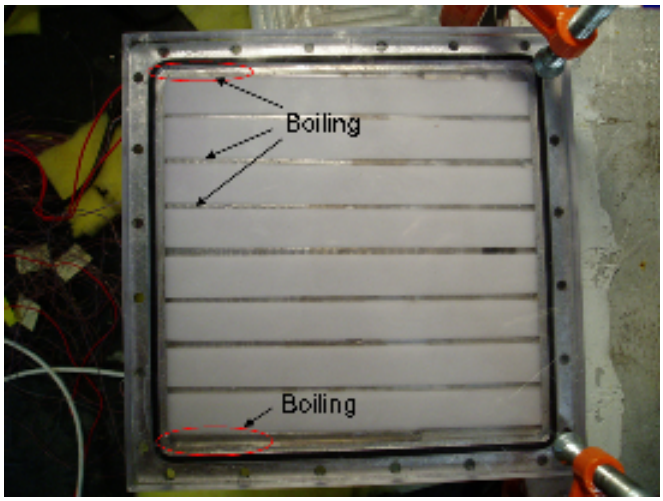

Figure 6.22 Observed Boiling Regions (Wick)

6.5 Steady State Summary

Steady state thermal resistance tests were performed on a sealed wick-based coldplate and a variety of configurations were evaluated. Parameters varied were wick configuration, fill ratio, coldplate position (horizontal vs. vertical), and working fluid (methanol-water mixtures). The best wick configuration was determined to be half inch strips with small gaps in between. This allowed a clear path for the generated vapor to reach the condenser side of the coldplate. With the wicking strips in place, the optimum fill ratio was 75%. With no wick in the cavity, the best thermal resistance in the horizontal position was achieved with a methanol-water mixture

(50-50 ratio). This resistance was 54% lower than that of the solid core. In other words, if the solid core, which is currently used to cool military electronics, were to be replaced with a coldplate with no wick and methanol, the power of the electronics could be doubled while maintaining the same temperature delta. With ceramic strips, the lowest resistance achieved in the horizontal position was with pure methanol as the working fluid, which was 46% less than that of the solid core. The poor performance of the pure water case was due to the heat flux levels, which did not cause the water to change phase. In the vertical position, there was a large disparity between the no wick and wick configurations. Without the wicking material, the performance was close to that of an empty cavity, while with the ceramics strips, the best resistance was 18% less than that of the solid core.

CHAPTER 7

CONCLUSION

7.1 Summary of Accomplishments and Results

In an effort to meet the objectives, mass transport within the porous medium was evaluated using both the height and weight approaches. Furthermore, the material properties and parameters of the wicking material and proposed test liquids were characterized. Methanol's superior wickability over ethanol was due to its lower viscosity. As observed in previous studies, the surface tension of the alcohol-water binary mixtures was reduced with increasing concentrations of alcohol. As expected, this decreasing trend in surface tension resulted in decreasing contact angles between these mixtures and the ceramic wick. However, FC-72 had poor wickability and formed a large contact angle with the ceramic in spite of its attractive surface tension. This unexpected result was only explained through a surface energy analysis using the Owens-Wendt Theory. Although FC-72 had an impressively low overall surface tension, its poor wickability onto the ceramic wick was due to the fact that its polar component of surface tension was higher than that of the polar component of the critical surface tension of the porous solid.

The next objective was to improve upon Raytheon's wick-based coldplate configuration. Transient cooling capacity tests were performed on an open wick-based coldplate and a variety of configurations were evaluated. By replacing the cotton with a ceramic wick, the transient cooling capacity was improved by 80%. Moreover, the use of binary mixtures further enhanced the transient cooling capacity by an order of magnitude.

The final objective was to develop a sealed, wick-based coldplate and determine its steady state thermal performance relative to current cooling schemes used in military

electronics. In doing so, a vacuum based degassing system was developed for single liquids and binary mixtures. This system is compatible with highly reactive fluids such as methanol. The hope was that the impressive performance of the binary mixtures observed in the transient (open) system would transfer to that of the sealed (closed) coldplate. Although this was not the case, significant enhancement was achieved. In the horizontal position, the wick-based coldplate produced thermal resistance values half of that of the solid thermal core. Therefore, in the horizontal position, the heat load capacity of the wick-based coldplate was double that of the current technology. In the vertical position, performance was improved by 18%.

7.2 Future Research

The focus of this study was to improve the performance of the working fluid. However, the overall, wick-based coldplate performance could be further enhanced by improving the surface energy of the wicking material. Commercially available alumina based ceramic fibers were investigated in this study. These fibers are held together via a bonding material. A study to investigate the effect of this bonding material on surface energy should be performed. Perhaps the bonding material may be specifically altered in an effort to increase the surface energy of the resulting wick. Next, the fiber material itself may be changed to a substance that inherently has a higher surface energy. Finally, the porous structure (i.e. porosity, pore size, pore shape, etc.) may be varied to determine an optimum design.

APPENDIX A

STUDENT-T DISTRIBUTION TABLE

Student-t Distribution Table

ν	75%	80%	85%	90%	95%	97.5%	99%	99.5%	99.75%	99.9%	99.95%
1	1.000	1.376	1.963	3.078	6.314	12.71	31.82	63.66	127.3	318.3	636.6
2	0.816	1.061	1.386	1.886	2.920	4.303	6.965	9.925	14.09	22.33	31.60
3	0.765	0.978	1.250	1.638	2.353	3.182	4.541	5.841	7.453	10.21	12.92
4	0.741	0.941	1.190	1.533	2.132	2.776	3.747	4.604	5.598	7.173	8.610
5	0.727	0.920	1.156	1.476	2.015	2.571	3.365	4.032	4.773	5.893	6.869
6	0.718	0.906	1.134	1.440	1.943	2.447	3.143	3.707	4.317	5.208	5.959
7	0.711	0.896	1.119	1.415	1.895	2.365	2.998	3.499	4.029	4.785	5.408
8	0.706	0.889	1.108	1.397	1.860	2.306	2.896	3.355	3.833	4.501	5.041
9	0.703	0.883	1.100	1.383	1.833	2.262	2.821	3.250	3.690	4.297	4.781
10	0.700	0.879	1.093	1.372	1.812	2.228	2.764	3.169	3.581	4.144	4.587
11	0.697	0.876	1.088	1.363	1.796	2.201	2.718	3.106	3.497	4.025	4.437
12	0.695	0.873	1.083	1.356	1.782	2.179	2.681	3.055	3.428	3.930	4.318
13	0.694	0.870	1.079	1.350	1.771	2.160	2.650	3.012	3.372	3.852	4.221
14	0.692	0.868	1.076	1.345	1.761	2.145	2.624	2.977	3.326	3.787	4.140
15	0.691	0.866	1.074	1.341	1.753	2.131	2.602	2.947	3.286	3.733	4.073
16	0.690	0.865	1.071	1.337	1.746	2.120	2.583	2.921	3.252	3.686	4.015
17	0.689	0.863	1.069	1.333	1.740	2.110	2.567	2.898	3.222	3.646	3.965
18	0.688	0.862	1.067	1.330	1.734	2.101	2.552	2.878	3.197	3.610	3.922
19	0.688	0.861	1.066	1.328	1.729	2.093	2.539	2.861	3.174	3.579	3.883
20	0.687	0.860	1.064	1.325	1.725	2.086	2.528	2.845	3.153	3.552	3.850
21	0.686	0.859	1.063	1.323	1.721	2.080	2.518	2.831	3.135	3.527	3.819
22	0.686	0.858	1.061	1.321	1.717	2.074	2.508	2.819	3.119	3.505	3.792
23	0.685	0.858	1.060	1.319	1.714	2.069	2.500	2.807	3.104	3.485	3.767
24	0.685	0.857	1.059	1.318	1.711	2.064	2.492	2.797	3.091	3.467	3.745
25	0.684	0.856	1.058	1.316	1.708	2.060	2.485	2.787	3.078	3.450	3.725
26	0.684	0.856	1.058	1.315	1.706	2.056	2.479	2.779	3.067	3.435	3.707
27	0.684	0.855	1.057	1.314	1.703	2.052	2.473	2.771	3.057	3.421	3.690
28	0.683	0.855	1.056	1.313	1.701	2.048	2.467	2.763	3.047	3.408	3.674

APPENDIX B

TRANSIENT TEMPERATURE PROFILES

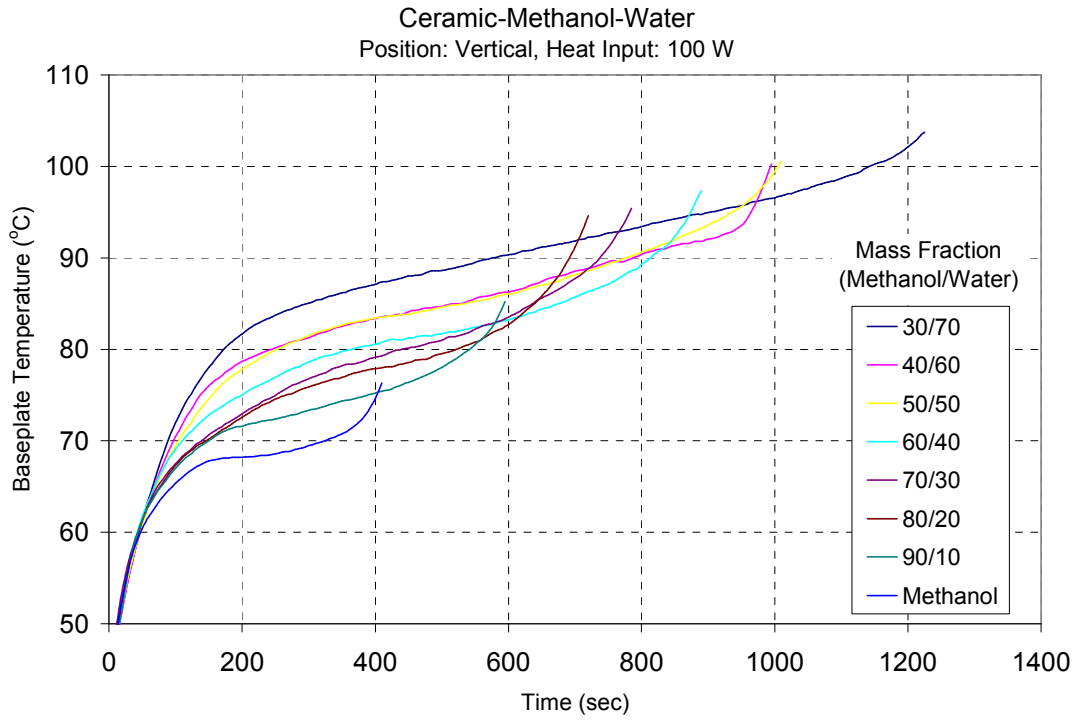
Ceramic-Methanol-Water
Position: Vertical, Heat Input: 100 W
Baseplate Temperature (°C)
110
100
90
80
70
60
50
0
200
400
600
800
1000
1200
1400
Time (sec)
Mass Fraction
(Methanol/Water)
30/70
40/60
50/50
60/40
70/30
80/20
90/10
Methanol

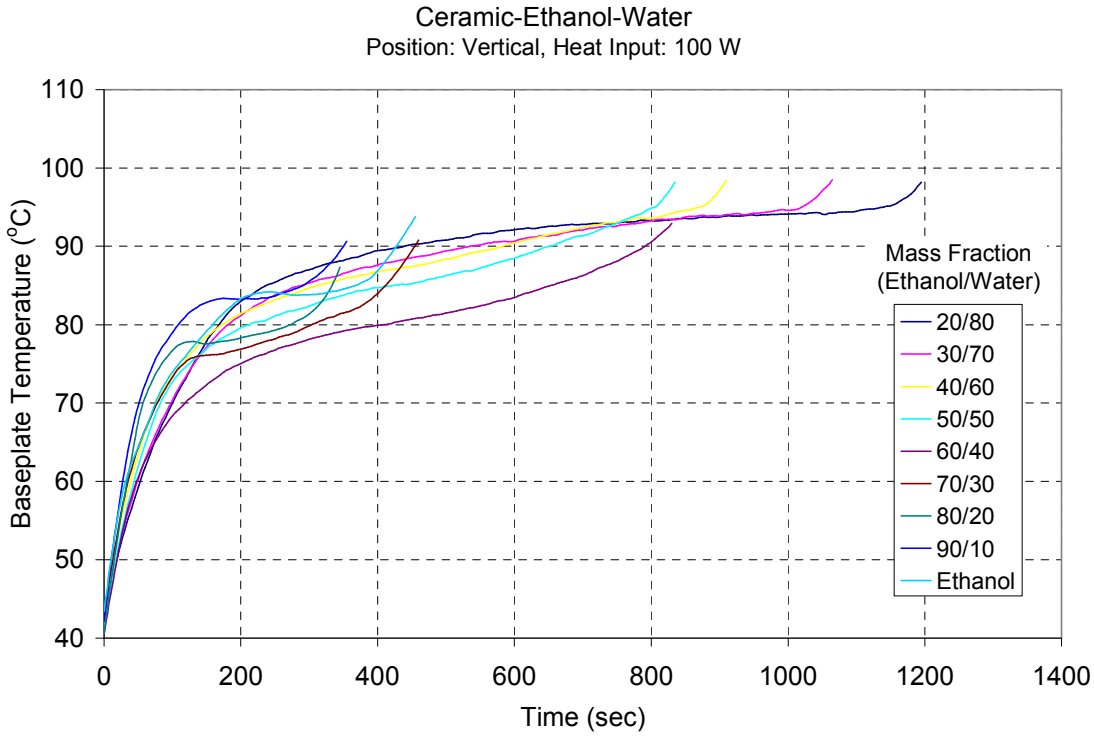
Ceramic-Ethanol-Water
Position: Vertical, Heat Input: 100 W
Baseplate Temperature (°C)
110
100
90
80
70
60
50
40
0
200
400
600
800
1000
1200
1400
Time (sec)
Mass Fraction
(Ethanol/Water)
20/80
30/70
40/60
50/50
60/40
70/30
80/20
90/10
Ethanol

REFERENCES

[1] Weber, R.M., Chen, K.W., “Thermal Management System Having Porous Fluid Transfer Element,” *United States Patent No.* US 7,161,802 B2, 1-7, 2007.

[2] Lide, D.R., Kehiaian, H.V., *CRC Handbook of Thermophysical and Thermochemical Data*, 212-220, 1994.

[3] Inoue, T., Teruya, Y., Monde, M., “Enhancement of pool boiling heat transfer in water and ethanol/water mixtures with surface-active agent,” *International Journal of Heat and Mass Transfer* 47, 5555-5563, 2004.

[4] van Oss, C.J., Giese, R.F., Li, Z., Murphy, K., Norris, J., Chaudhury, M.K., Good, J.R., *Journal of Adhesion Science Technology*, 6, 413, 1992.

[5] Varadaraj, R., Bock, J., Brons, N., Zushma, S., “Influence of Surfactant Structure on Wettability Modification of Hydrophobic Granular Surfaces,” *Journal of Colloid and Interface Science*, 167, 1, 207-210, 1994.

[6] Patnaik, A., Rengasamy, R.S., Kothari, V.K., Ghosh, A., “Wetting and Wicking in Fibrous Materials,” *Textile Progress*, 38, No 1, 40-46, 2006.

[7] Figliola, R.S., Beasley, D. E., *Theory and Design for Mechanical Measurements*, 4th Edition, 120-154, 2006.

[8] Washburn, E.W., “The Dynamics of Capillary Flow,” *Physics Review*, 273-283, 1921.

[9] Zisman, W.A., “Relation of Equilibrium Contact Angle to Liquid and Solid Constitution,” *ACS Advances in Chemistry,* Series #43, 1-51, 1961.

[10] Owens, D.K., Wendt, R.C., *Journal of Applied Polymer Science*, 13, 1741, 1969.

[11] Fowkes, F.M., *Journal of Industrial and Engineering Chemistry*, 56, 12, 40, 1964.

[12] van Oss, C.J., Good, R.J., Chaudhury, M.K., “The role of van der Waals forces and hydrogen bonds in hydrophobic interactions between biopolymers and low energy surfaces” *Journal of Colloid and Interface Science,* 111, 378-390, 1986

[13] Good, R.J., Girifalco, L.A., *Journal of Physics and Chemistry*, 64, 561, 1960.

[14] Chibowski, E., Kerkeb, M.L., González-Caballero, F., “On the Problem of Acid-Base Interaction Determination for Weakly Polar Solids: Cholesterol Surfaces”, *Journal of Colloid and Interface Science,* 155, 444-451, 1993.

[15] Holmberg, K., *Handbook of Applied Surface and Colloid Chemistry*, 219, 2002.

[16] Stabinger, H., "Density Measurement using modern oscillating transducers", South Yorkshire Trading Standards Unit, 34-41, 1994.

[17] Labajos-Broncano, L., González-Martín, M.L., Bruque, J.M., González-García, C.M., “Comparison of the Use of Washburn’s Equation in the Distance-Time and Weight-Time Inbibition Techniques”, *Journal of Colloid and Interface Science*, 233, 356-360, 2001.

[18] Labajos-Broncano, L., González-Martín, M.L., Bruque, J.M., González-García, C.M., Janczuk, B., “On the Use of Washburn’s Equation in the Analysis of Weight-Time Measurements Obtained from Imbibition Experiments”, *Journal of Colloid and Interface Science*, 219, 275-281, 1999.

[19] Rulison, C., “So You Want to Measure Surface Energy?” Augustine Scientific, Application Note 401, 8, 1998.

[20] Dunn, P.D., Reay, D.A., *Heat Pipes*, 2nd Edition, 163-174, 1978.

[21] Peterson, G.P., *An Introduction to Heat Pipes*, 34-41, 1994.

[22] *Parker O-ring Handbook*, ORD 5700, Parker Hannifin Corporation, 4-14, 2000.

[23] Tuma, P.E., “Weight Gain, Volume Swell, and Extraction Compatibility Test,” 3M Company, 1-6, 1998.

[24] Xu, Y., “Direct Contact Condensation With and Without Non-condensable Gas in Water,” Dissertation, Purdue University, 56-57, 2004.

[25] Egbert, H., et al., “Test Method Standard for Environmental Engineering Considerations and Laboratory Tests,” MIL-STD-810, Department of Defense, 16, 1989.

[26] Essome, G.R., Orozco, J., “An Analysis of Film Boiling of a Binary Mixture in a Porous Medium,” *International Journal of Heat and Mass Transfer*, 34, 3, 757-766, 1991.

[27] Fujita, Y., Tsutsui, M., “Heat Transfer in Nucleate Pool Boiling of Binary Mixtures,” *International Journal of Heat and Mass Transfer*, 37, 1, 291-302, 1994.

[28] Pratt, D.M., Kihm, K.D., “Binary Fluid Mixture and Thermocapillary Effects on the Wetting Characteristics of a Heated Curved Meniscus,” *Journal of Heat Transfer*, 125, 867-874, 2003.

BIOGRAPHICAL INFORMATION

Mauricio Adrián Salinas received his B.S. in Mechanical Engineering from the University of Texas – Pan American in his home town of Edinburg, Texas (1996). He then received an M.S. in Mechanical Engineering with a depth in heat transfer from Stanford University (1998). Each summer while an undergraduate and masters candidate, Mauricio served as an intern at the NASA Lewis Research Center in Cleveland, Ohio. The bulk of his experience at NASA dealt with empirical evaluations of micro-gravity combustion. Upon graduation from Stanford, he accepted a position in the Thermal Design Group of Raytheon TI Systems, where he currently holds the position of Principal Mechanical Engineer. His responsibilities include thermal analysis, design and testing of military electronics and he has developed expertise in thermoelectric and cryogenic coolers. His experience includes the thermal design of night vision cameras, advanced airborne processors and radar systems, ground based military electronics, and anti-iced radomes. Mauricio has served as Secretary, Treasurer, Vice-Chair, and Chair of the ASME Electronics and Photonics Packaging Division (EPPD) and is currently serving as Treasurer of the ASME North Texas Section. Salinas is a Registered Professional Engineer in the State of Texas.